The influence of oxygen vacancy concentration in nanodispersed non-stoichiometric $CeO_{2-\delta}$ oxides on the physico-chemical properties of conducting polyaniline/CeO_2 composites

Bojana Kuzmanović [a], Milica J. Vujković [b, *], Nataša Tomić [c], Danica Bajuk-Bogdanović [b], Vladimir Lazović [c], Biljana Šljukić [b], Nenad Ivanović [a], Slavko Mentus [b, d]

[a] Institute of Nuclear Sciences "Vinča", Mike Petrovića Alasa 12-14, 11001, Belgrade, University of Belgrade, Serbia
[b] Faculty of Physical Chemistry, University of Belgrade, Studentski trg 12-16, 11158, Belgrade, Serbia
[c] Institute of Physics Belgrade, University of Belgrade, Pregrevica 118, 11080, Belgrade, Serbia
[d] Serbian Academy of Sciences and Arts, Knez Mihajlova 35, 11000, Belgrade, Serbia

ARTICLE INFO

ABSTRACT

Cerium oxide ($CeO_{2-\delta}$) ultrafine nanoparticles, with the lower ($CeO_{2-\delta}$-HT) and higher ($CeO_{2-\delta}$-SS) fraction of oxygen vacancies, were used as anchoring sites for the polymerization of aniline in acidic medium. As a result, polyaniline-emeraldine salt (PANI-ES)-based composites (PANI-ES@$CeO_{2-\delta}$-HT and PANI-ES@$CeO_{2-\delta}$-SS) were obtained. The interaction between $CeO_{2-\delta}$ and PANI was examined by FTIR and Raman spectroscopy. The PANI polymerization is initiated via electrostatic interaction of anilinium cation and Cl^- ions (adsorbed at the protonated hydroxyl groups of $CeO_{2-\delta}$), and proceeds with hydrogen and nitrogen interaction with oxide nanoparticles. Tailoring the oxygen vacancy population of oxide offers the possibility to control the type of PANI-cerium oxide interaction, and consequently structural, electrical, thermal, electronic and charge storage properties of composite. A high capacitance of synthesized materials, reaching ~294 $F\,g^{-1}$ (PANI-ES), ~299 $F\,g^{-1}$ (PANI-ES@$CeO_{2-\delta}$-HT) and ~314 $F\,g^{-1}$ (PANI-ES@$CeO_{2-\delta}$-SS), was measured in 1 M HCl, at a common scan rate of 20 mV s^{-1}. The high adhesion of PANI with cerium oxide prevents the oxide from its slow dissolution in 1MHCl thus providing the stability of this composite in an acidic solution. The rate of electrochemical oxidation of emeraldine salt into pernigraniline was also found to depend on $CeO_{2-\delta}$ characteristics.

© 2019 Elsevier Ltd. All rights reserved.

1. Introduction

The linkage of diverse metal oxides (TiO_2, CeO_2, ZnO, graphene oxide, SiO_2, Fe_xO_y, MnO_2 …) with one of the oldest conducting polymers such as polyaniline (PANI) has been shown as an effective strategy for improving mechanical, thermal, dielectric, electrical and optical properties of this polymer [1—5]. An easy synthesis, environmental stability, and fast doping/dedoping process, make PANI very suitable matrix for the facile further fabrication. On the other hand, inorganic oxides easily interact with PANI chains, resulting in the synergistic behaviour. The versatile properties of these hybrid materials, achieved either through the different degree of PANI's protonation or different oxide structures (obtained through numerous synthesis procedures), make their study inexhaustable.

While the investigations of composites with TiO_2 were quite diverse and numerous, the studies on PANI/CeO_2 nano-composites have mostly directed to the development of sensor technology including H_2O_2 sensors, humidity sensors, biosensors, gas sensing materials [6—11]. The positive influence of CeO_2 particles, incorporated into PANI chains, has been recognized in many sensor properties. Besides, the binding of cerium oxide with the polyaniline was found to improve thermal [12,13], corrosion protection [14] and electrochemical properties [15—17]. Still, the studies regarding the Ce-oxide's influence to the charge storage properties of polyaniline are quite rare. Recently, Fei et al. [17] showed that an indirect chemical bonding of PANI to CeO_2 surface via its —OH and —NCO functionalized groups improves both electrocatalytic and capacitive performance of PANI. By mixing CeO_2 with 10% of PANI,

Maheswari et al. [15] have significantly improved charge storage properties of oxide in HCl, from a very high value of 927 F g^{-1} (for pure oxide) to the extremely high one amounting to 1452 F g^{-1} for the CeO$_2$/PANI composite. Also, Gong et al. [16], have recently prepared nickel doped cerium oxide nanospheres at PANI (Ni–CeO$_2$@PANI) as an electrode material for supercapacitors, which provided a very high capacitance of 894 F g^{-1} (at 1 A g^{-1}), thanks to the defective nature of Ni–CeO$_2$. The excess of reactive oxygen vacancies was achieved by doping CeO$_2$ with nickel atoms, whereas the Ni–CeO$_2$@PANI nanocomposite was prepared by in situ chemical oxidative polymerization of aniline in presence of Ni–CeO$_2$ particles. Herein, polyaniline-cerium oxide composites have been synthesized by typical chemical polymerization of aniline (under highly acidic conditions), adsorbed on the surface of cerium-oxide nanoparticles, in order to examine its charge storage ability. The idea was to use the two types of CeO$_{2-\delta}$, containing different fraction of oxygen vacancies (without metal doping), in order to compare how the O-vacancy population influences the PANI-CeO$_2$ interaction. The oxide's particles were synthesized by two different methods: i) the solid-state method, yielding cerium-oxide with higher concentration of oxygen vacancies and ii) the hydrothermal method yielding oxide with lower concentration of oxygen vacancies. The influence of vacancy concentration of CeO$_{2-\delta}$ oxides, in their composites with highly conductive emeraldine form of PANI, on the thermal, vibrational and electrochemical properties of composites, was thoroughly examined. The mechanism of PANI-CeO$_{2-\delta}$ interaction is proposed and discussed.

2. Experimental

2.1. Synthesis procedure

2.1.1. Synthesis of polyaniline emeraldine salt

Polyaniline, in the form of emeraldine salt (PANI-ES), was synthesized by typical chemical polymerization of aniline (Sigma Aldrich) in the presence of hydrochloric acid using ammonium persulfate (Sigma Aldrich) as an oxidant [18]. Briefly, 0.18 mL of two times distilled aniline monomer was injected into 7 mL of 2 M HCl solution. 0.45 g (NH$_4$)$_2$SO$_4$ (previously dissolved in 2 mL of deionized water) was dropped to the solution and stirred magnetically at 25 °C. After filtration, the precipitate was washed (with 2 M HCl and deionized water followed by ethanol) and dried at 60 °C in the oven for 36 h.

2.1.2. Hydrothermally synthesis of CeO$_{2-\delta}$

The CeO$_{2-\delta}$ nanoparticles with a lower amount of oxygen vacancies were prepared by the hydrothermal treatment (CeO$_{2-\delta}$-HT), according to the procedure presented in Ref. [19]. In a typical synthesis, 2 g of polyvinylpyrrolidone (Sigma Aldrich) was dissolved in 40 mL of deionized water, continuously stirring on a magnetic stirrer (at room temperature T ≈ 25 °C) until a homogeneous solution was obtained. 6 mmol of Ce(NO$_3$)$_3$·6H$_2$O (Acros Organics 99.5%), previously dissolved in deionized water V = 40 mL, was slowly added to the resulting solution, with constant stirring. During the synthesis, the pH of the solution was not adjusted and value was pH ≈ 4. The prepared solution was put into a Teflon-lined stainless steel autoclave (capacity ∼ 80 mL), and hydrothermally treated at 200 °C for 6 h. After synthesis, the autoclave was cooled down to room temperature naturally. The resulting precipitate was collected and washed several times with distilled water, and afterwards dried in a vacuum oven overnight at 105.5 °C.

2.1.3. Solid state synthesis of CeO$_{2-\delta}$

Solid-state reaction at room temperature was used for the synthesis CeO$_{2-\delta}$ ultrafine particles with a higher amount of oxygen vacancies [20,21]. Cerium nitrate hexahydrate (Acros Organics 99.5%) and sodium hydroxide (Carlo Erba) were used as starting materials for this procedure. Synthesis involves manual mixing of the starting chemicals in mortar (∼10 min) until the mixture becomes light brown. After exposure to the air (4 h), the sample was washed four times with distilled water and twice with ethanol to remove NaNO$_3$. The final product was transferred into petri dish using ethanol and dried at 60 °C in a drying oven overnight. The final result of the synthesis obtained is a light yellow powder CeO$_{2-\delta}$.

$$2[(Ce(NO_3)_3 \times 6H_2O] + 6NaOH + (1/2-\delta)O_2 \rightarrow 2CeO_{2-\delta} + 6NaNO_3 + 15H_2O$$
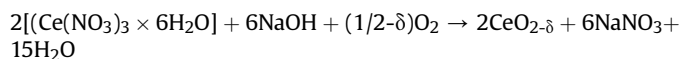
2.1.4. PANI@CeO$_{2-\delta}$ synthesis procedure

The PANI@CeO$_{2-\delta}$ composites were prepared in the same way as PANI-ES, in presence of cerium oxide. Namely, 0.18 mL of distilled aniline monomer was injected into an aqueous solution of 2 M HCl, containing 50 mg of CeO$_{2-\delta}$-SS or CeO$_{2-\delta}$-HT ultrafine nanoparticles. The acidic solutions of cerium-oxide nanoparticles were previously treated by ultrasound to prevent aggregation of nano-CeO$_2$ particles. The oxidizing agent (NH$_4$)$_2$S$_2$O$_8$ (0.45 g), previously dissolved in 2 ml deionized water, was added to the solutions drop by drop. After mixing the solution for 6 h on a magnetic stirrer, at room temperature, the samples were filtered and washed. Afterwards, the obtained dark-green PANI@CeO$_{2-\delta}$ composites, labelled as PANI-ES@CeO$_{2-\delta}$-SS and PANI-ES@CeO$_{2-\delta}$-HT, were dried in the oven at 60° for 36 h to achieve the constant weight.

For the sake of comparison, the similar experiments using 100 mg of CeO$_{2-\delta}$-SS and 9 mg, 50 mg and 100 mg of TiO$_2$ anatase (Sigma Aldrich) were also performed.

2.2. Characterization

The obtained powdered samples were pressed into pellets and their conductivity was measured between two stainless pistons using an ac bridge (Waynne Kerr Universal Bridge B 224) at 1.0 kHz, at room temperature and pressure of 375 MPa.

Thermogravimetric and differential thermal analysis (TG/DTA) were carried out simultaneously by an SDT 2960 Simultaneous DSC-TGA thermal analyzer, in air atmosphere with a flowing rate of 10 C min^{-1}.

The morphology of synthesized samples was observed by field-emission scanning electron microscope (FESEM, Tescan MIRA3). PANI-based samples were clearly visible as such, while cerium oxide sample required vacuum decoration by gold.

The Raman spectra of samples were recorded on a DXR Raman microscope (Thermo Scientific) equipped with a research optical microscope and a CCD detector. A HeNe gas laser with an excitation wavelength of 633 nm was used for all measurements. The scattered light was analyzed by the spectrograph with a grating of 600 lines mm^{-1} and a spectrograph aperture of 50 μm slit. The laser power was kept at 0.5 mW on the sample. Each spectrum was measured with an exposure time of 30 s and number of exposures of 20.

The Infrared transmission spectra (FTIR) of the samples in the form of pellets with KBr, were recorded using an Avatar System 370 spectrometer (Thermo Nicolet), with 64 scans per sample and 2 cm^{-1} resolution in the wavenumber range 4000–400 cm^{-1}.

2.3. Electrochemical measurements

Electrochemical measurements of examined samples were performed at Gamry PCI4/300 Potentiostat/Galvanostat, in the

typical three-electrode configuration. The reference electrode was a saturated calomel electrode (SCE), while the counter electrode was a wide Platinum foil (Pt). To prepare the working electrode the examined powder was mixed with the 5 wt% Nafion binder (Sigma Aldrich) in ethanol/water, in the 95:5 ratio. Several drops of ethanol were added in order to obtain the desired viscosity. After homogenization in an ultrasonic bath, the slurry was deposited over the rectangular glassy carbon support and dried at ambient temperature in order for ethanol to evaporate. The loading mass was 1.7 mg cm^{-2} for all examined electrodes. The electrolyte was 1 mol dm^{-3} HCl aqueous solution.

3. Results and discussion

3.1. Conductivity measurements

The synthesized PANI-ES delivers a high value of electronic conductivity, amounting to ~0.6 S/cm. The incorporation of semiconducting cerium-oxide, into polymer matrix, decreases the conductivity to ~0.5 S/cm and ~0.3 S/cm for PANI-ES@CeO$_{2-\delta}$-SS and PANI-ES@CeO$_{2-\delta}$-HT, respectively.

3.2. Thermal behavior

Thermal behavior of prepared samples was examined by simultaneous thermogravimetric/differential thermal analysis (TGA/DTA), in the temperature range 25–700 °C, under air atmosphere. The characteristic thermogram of conducting polymer [22], made of three separated weight loss steps, is observed (Fig. 1a). The first weight loss (about 7%) up to 100 °C, originates from desorption of adsorbed water molecules, while the second weight loss between 180 and 300 °C (about 13%) can be attributed to the elimination of protonating acid dopant (HCl) bound to the polymer chain. The third and the greatest weight loss (about 80% for pure PANI), within the temperature range 300–700 °C, corresponds to the structural degradation of the polymer backbone [22]. One can notice that both composites, unlike the pure PANI, did not lose the whole weight at 700 °C, but ~96.3% (PANI-ES@CeO$_{2-\delta}$-SS) and ~95.8% (PANI-ES@CeO$_{2-\delta}$-HT) of its initial weight. It is due to a high thermal stability of inorganic cerium oxide. Based on this, the fraction of cerium-oxide in the composite could be determined and, relative to the mass of dried sample (taking into account the amount of adsorbed water), was found to be ~4% (PANI-ES@CeO$_{2-\delta}$-SS) and 4.5% (PANI-ES@CeO$_{2-\delta}$-HT). Somewhat higher content of hydrothermally synthesized oxide in the composite was obtained. This is in the correlation with the higher concentration of Ce^{4+} ions i.e. higher fraction of oxygen atoms in the CeO$_{2-\delta}$-HT crystal lattice.

It can be seen that weight loss of samples, up to 300 °C (removal of water molecules and dopant), is insensitive to the presence of oxide (it is governed by the type of dopant). However, above ~300 °C, there are differences in the thermal decomposition of the polymer chain in examined samples, which are more visible in corresponding DTA curves (Fig. 1b). As our DTA curves show, two exothermic peaks follow the process of ES degradation within the temperature region 300–700 °C. The position of the first DTA peak (appearing at 384 °C) is the same for PANI-ES and PANI-ES@CeO$_{2-\delta}$-SS, while its values for PANI-ES@CeO$_{2-\delta}$-HT is slightly shifted towards higher temperature (393 °C). The second DTA peak, higher in the intensity, appears at ~489 °C (PANI-ES), 499 °C (PANI-ES@CeO$_{2-\delta}$-SS), 512 °C (PANI-ES@ CeO$_{2-\delta}$-HT). It can be concluded that the thermal resistance of PANI becomes higher by its binding with the cerium-oxide, especially when the chains grew on hydrothermally prepared oxide. This originates from its strong interaction with the oxide. The improved thermal stability of PANI in interaction with metal oxides has been already reported [12,13,17], but the opposite
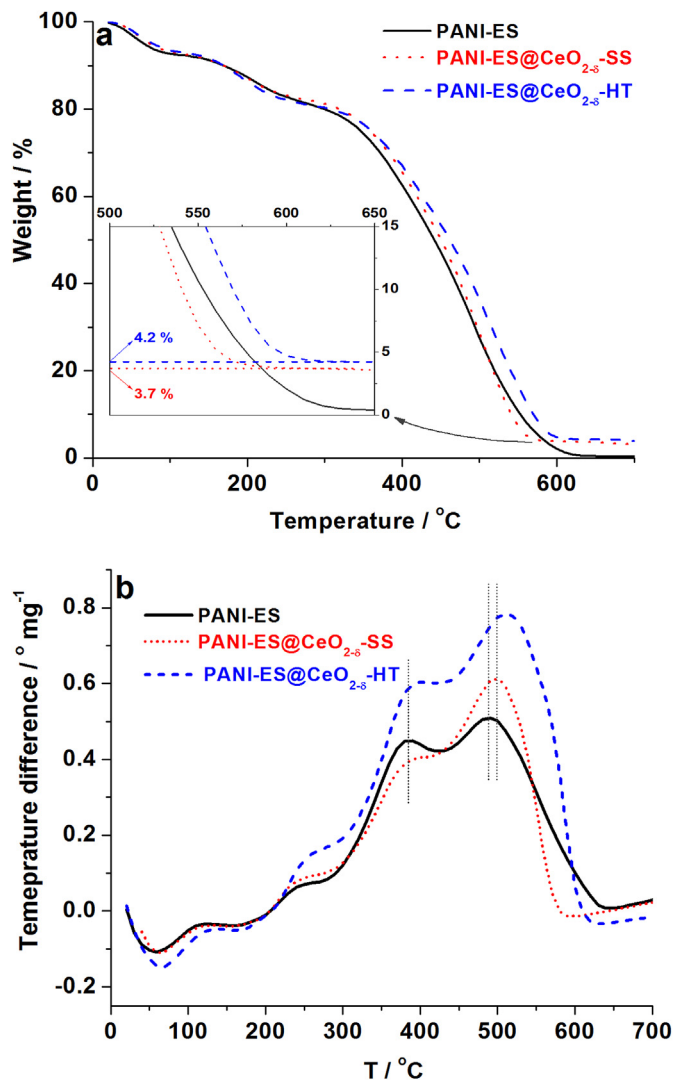

Fig. 1. TG (a) and DTA (b) curves of PANI-ES and PANI-ES@CeO$_{2-\delta}$ samples.

behavior [17] was also found. These variations can be explained in the different interactions of cerium oxide with polyaniline chains, which can be influenced by the synthesis of oxide, the type of PANI dopant and the doping level. Here, higher thermal stability of PANI was obtained for the composite containing CeO$_{2-\delta}$ with the lower fraction of oxygen vacancies. Furthermore, the declining slope of the PANI@CeO$_{2-\delta}$ DTA curves is steeper than that of PANI-ES, which suggests that the cerium oxide acts as a catalyst of the combustion process of carbon, formed by the thermal decomposition of polymer.

3.3. Morphology

Ultrafine nanoparticles of CeO$_{2-\delta}$-HT and CeO$_{2-\delta}$-SS are shown in Fig. 2a and b. Nanodispersed, nearly spherical particles, 20–40 nm in diameter, prevail on the CeO$_{2-\delta}$-SS surface (Fig. 2a) while the CeO$_{2-\delta}$-HT sample is composed of monodispersed spherical particles, 0.7–1.1 μm in diameter (Fig. 2b). Interestingly, these submicron/micron CeO$_{2-\delta}$-HT spheres are huge agglomerates of nanoparticles 20–40 nm in diameter, which are similar to CeO$_{2-\delta}$–SS particles. Representative FE-SEM micrograph of PANI-ES sample shows that the short nanofibers (~75 nm in diameter) can be perceived (Fig. 2c). The FE-SEM micrographs of PANI-ES@CeO$_{2-}$
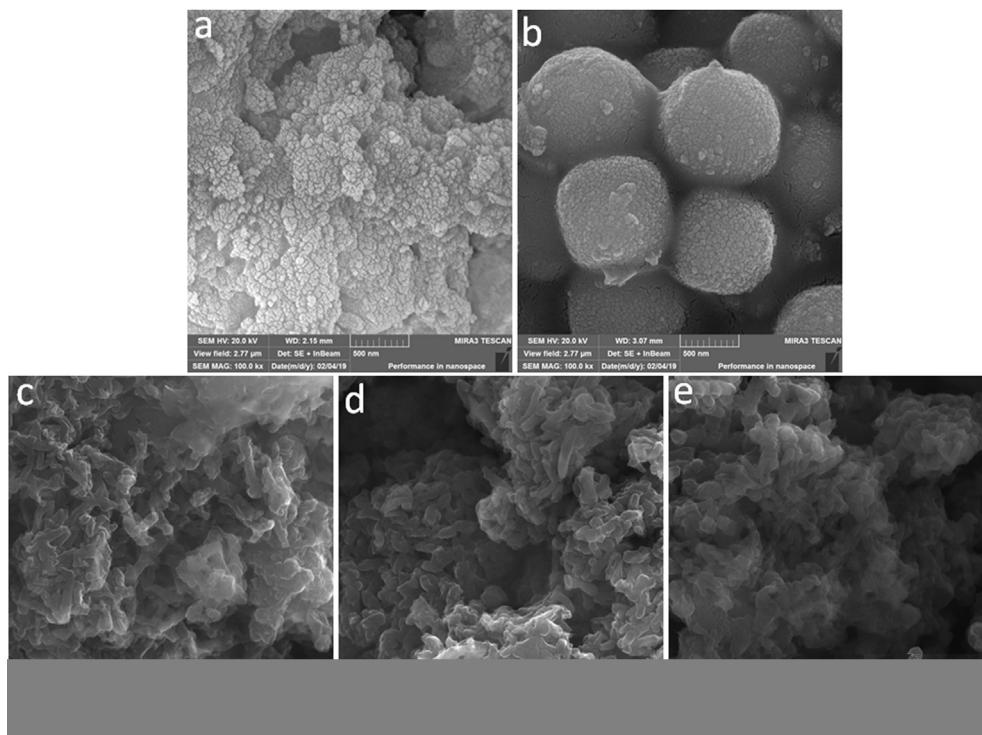
Fig. 2. SEM micrographs of $CeO_{2-\delta}$-SS (a), $CeO_{2-\delta}$-HT particles (b), PANI-ES (c), PANI-ES@$CeO_{2-\delta}$-SS (d) and PANI-ES@$CeO_{2-\delta}$-HT (e).

δ composites (Fig. 2d and e) indicate that the presence of ultrafine nanodispersed $CeO_{2-\delta}$ particles do not influence the original PANI-ES morphology.

3.4. Vibrational spectroscopy study

3.4.1. Infrared spectroscopy

It is well known that FTIR spectrum of PANI is very sensitive to various experimental conditions such as humidity, temperature, pressure, storing and processing of samples and so on [23]. In order to avoid differences caused by the influence of the mentioned parameters we measured the spectra under the same conditions following recommendations by Trchova et al. [23].

Representative FTIR spectra of synthesized polyaniline-based samples are shown in Fig. 3. The characteristic spectrum of protonated emeraldine salt form can be recognized in all samples. The assignation of FTIR bands (well-documented in literature [23—30]), is presented in Supplementary Data. The spectrum of PANI-ES@$CeO_{2-\delta}$ sample is almost the same as the spectrum of pure PANI-ES since the characteristic $CeO_{2-\delta}$ vibrational modes (shown in inset of Fig. 3) cannot be distinguished. This can be associated to very intensive vibrational bands of protonated polyaniline as well as the low amount of cerium oxide in the composite. It can only be noticed that the intensity ratio of $1306/1244\ cm^{-1}$ bands (which are assigned to C—N stretching modes) changes in the presence of the oxide being 1.25, 1.28 and 1.29 for PANI-ES, PANI-ES@$CeO_{2-\delta}$-SS, and PANI-ES@$CeO_{2-\delta}$-HT, respectively. These changes are in correlation with the measured trend of electronic conductivity, and suggest the involvement of nitrogen from the polymer chain in the interaction with oxide.

3.4.2. Raman spectroscopy

The molecular structure of samples was studied also by Raman spectroscopy. The obtained Raman spectrum of PANI-ES (Fig. 4a) is typical for protonated emeraldine form, and its assignment is well-
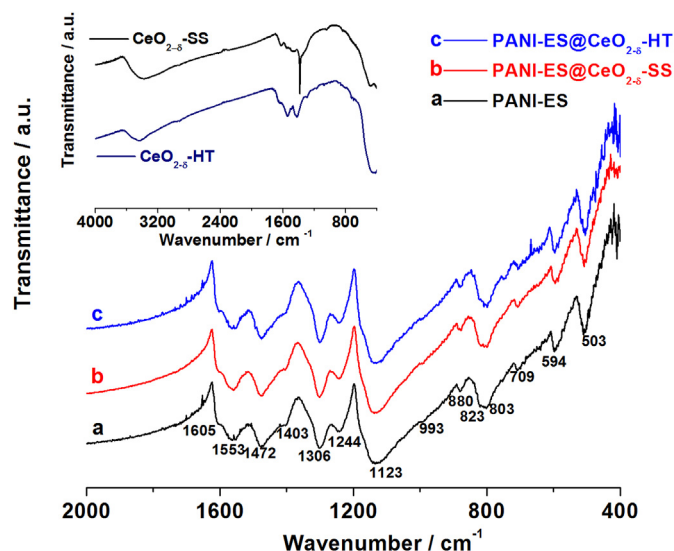

Fig. 3. FTIR spectrum of PANI-ES (a), PANI-ES@$CeO_{2-\delta}$-SS (b) and PANI-ES@$CeO_{2-\delta}$-HT (c). FTIR spectra of pure $CeO_{2-\delta}$-SS and $CeO_{2-\delta}$-HT are given in inset.

documented [27,31—36]. It can be seen in Supplementary Data.

Raman spectra of PANI@$CeO_{2-\delta}$ composites (Fig. 4b and c) show all characteristic modes of PANI-ES, but $CeO_{2-\delta}$ vibrations cannot be distinguished. The $CeO_{2-\delta}$ spectra are measured under the same experimental conditions as that of PANI-ES and presented in the inset of Fig. 4. The high intensity Raman band at $\sim463\ cm^{-1}$ corresponds to the F_{2g} vibrational mode of fluorite $CeO_{2-\delta}$ structure. Interestingly, this high intensity mode is not visible in the spectra of composites. This confirms that the CeO_2 is encapsulated into polymer chains thus forming the core-shell structure, via the polymerization of aniline adsorbed on the cerium oxide as a
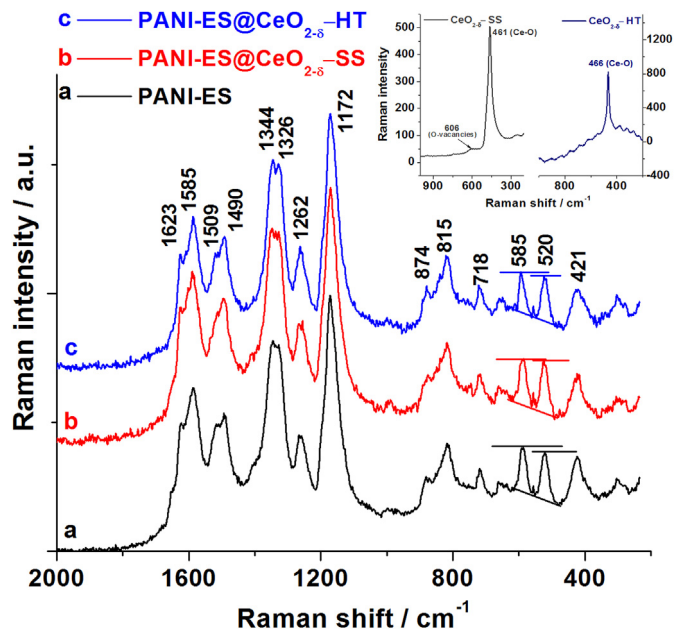
Fig. 4. Raman spectra of PANI-ES (a), PANI-ES@CeO$_{2-\delta}$-SS (b) and PANI-ES@CeO$_{2-\delta}$-HT in the normalized scale (c). Spectra of pure CeO$_{2-\delta}$-SS and CeO$_{2-\delta}$-HT oxides are given in inset.

nucleation core. A weak broadband (at ~ 606 cm^{-1}) in the spectrum of CeO$_{2-\delta}$-SS is related to the presence of oxygen vacancies. The use of more appropriate Raman conditions [35], provides more defined oxide modes, suggesting that both synthesized oxides investigated in this work actually possess a certain amount of vacancies, which is noticeable higher in the CeO$_{2-\delta}$-SS sample.

The changes of the PANI-ES mode positions due to the presence of CeO$_{2-\delta}$ are not visible, but changes of the vibration modes intensity can be noticed. One can notice the CeO$_{2-\delta}$ influence on the band corresponding to the C ~ N$^+$• stretching vibration of the delocalized polaronic structure, which is also identified by FTIR. Actually, the splitting of this band to ~1344 cm^{-1} and ~1326 cm^{-1} modes, which occurs in the pure PANI-ES, is more pronounced in the composites, especially in the PANI@CeO$_{2-\delta}$-HT sample with the lower concentration of vacancies, and consequently, a higher degree of Ce^{4+} ions. It seems that the relative ratio of 1344 cm^{-1}/1326 cm^{-1} bands decreases in the composite thus confirming the involvement of PANI's nitrogen in the interaction with cerium ions handing in electrons. By donating electrons to oxide, the C–N$^+$ stretching bonds became weaker thus appearing at low wavenumbers which is reflected in the decreased intensity of 1344 cm^{-1} band on account of the increase of 1326 cm^{-1} band intensity. The change in the 1509 cm^{-1} mode, corresponding to N–H deformation vibrations, upon PANI-CeO$_{2-\delta}$ interaction, is also visible and is more pronounced in the composite containing CeO$_{2-\delta}$-SS.

The PANI-CeO$_{2-\delta}$ interaction causes also pronounced changes of the vibrational modes intensity in the low-frequency region (in which the oxides modes appear). The relative intensity of the PANI's 421 cm^{-1} band (which is positioned in the vicinity of the most intensive CeO$_{2-\delta}$ mode), is decreased in the composite. It can be correlated to the stronger F$_{2g}$ vibrational mode of fluorite structure of CeO$_{2-\delta}$ which causes the strong interaction. Furthermore, the intensity ratio of bands at 585 cm^{-1} (positioned in the vicinity of oxygen vacancy band) and 520 cm^{-1} is decreased upon CeO$_{2-\delta}$ action (as indicated in Fig. 4), thus following the trend PANI-ES, PANI@CeO$_{2-\delta}$-HT, PANI@CeO$_{2-\delta}$-SS. So, this decrease is more pronounced for PANI@CeO$_{2-\delta}$-SS, which could be related to the presence of higher concentration of oxygen vacancies. Also, the

change in the relative intensity of 718 cm^{-1}-assigned band to other bands follows this trend.

The observed changes in the Raman modes of polyaniline caused by the presence of cerium oxide indicates the existence of two types of PANI-CeO$_{2-\delta}$ interactions including the nitrogen- (from radical cation) and hydrogen (from amine of polarons and bipolarons) bonding. Unlike the interaction involved nitrogen atoms, it seems that the hydrogen bonding interaction is facilitated by oxygen vacancies in the oxide lattice.

3.5. Electrochemical behavior

3.5.1. Narrower voltage interval

The influence of the cerium oxide to the charge storage behavior of PANI was studied by Cyclic Voltammetry. Typical redox pair of PANI, corresponding to the transition of leucoemeraldine to emeraldine salt, was observed in the potential range from −0.2 V vs. SCE to 0.6 V vs. SCE (Fig. 5a) [37]. This redox process is sensitive to the presence and relative fraction of CeO$_{2-\delta}$ in the samples. As shown in Fig. 5a and Fig. S1, the current response of both cerium-oxides, in an acidic solution, is very poor, (below ~1 mA). On the other hand, PANI has more than twenty times higher current response. Theoretically, the ratio of active redox centers, such as Ce^{4+}/Ce^{3+} and the amino/imino centers in the composite (wt%/M for CeO$_{2-\delta}$: wt%/M for C$_6$H$_5$NH), corresponds exactly to the ratio of 1:22, respectively. However, taking into account the mass ratio of individual components in the composite, the current ratio of PANI and oxide (in the composite) would be even higher in favor of PANI. Therefore, the slightly depressed current response of PANI-ES could be expected if the certain fraction of PANI was replaced with CeO$_{2-\delta}$. However, the current response of PANI was somewhat increased after incorporation of cerium-oxide. This enhancement factor depends on the type of used oxide. Actually, the interaction of PANI with CeO$_{2-\delta}$-HT leads to the very small increase of its current (which is practically negligible), while this response became somewhat higher in the presence of CeO$_{2-\delta}$-SS (Fig. 5a and b). Charge/discharge capacitance expressed in F g^{-1}, were found to be 296/294 F g^{-1} for pure PANI, 302/299 Fg^{-1} for PANI@CeO$_{2-\delta}$-HT and 319/314 F g^{-1} for PANI@CeO$_{2-\delta}$-SS, at a common scan rate of 20 mVs^{-1}.

Incorporation of CeO$_{2-\delta}$ into PANI-ES provides a slightly higher coulombic capacity despite the fact that the conductivity of composite was decreased by CeO$_{2-\delta}$ doping (although it decreased, the electronic conductivity of PANI-based composite is still very high). Therefore, the capability of polyaniline chains to attach/release electrolyte ions (without the charge transfer of protons) to compensate acceptance/liberation of electrons upon cycling can be limiting step. This process can be faster in the composite due to improved wettability caused by CeO$_{2-\delta}$ presence [38]. Better charge behavior of PANI@CeO$_{2-\delta}$-SS than PANI@CeO$_{2-\delta}$-HT can be attributed to the differences in wettability. CeO$_{2-\delta}$-SS surface contains a higher amount of surface hydroxyl groups, compared to the one of CeO$_{2-\delta}$-HT surface (Fig. 3). The presence of these groups improves the wettability of both PANI's surface at its boundary with CeO$_{2-\delta}$.

To summarize, both investigated PANI@CeO$_{2-\delta}$ composites present novel materials with a very large charge storage ability in an acidic solution. The synthesized PANI-ES@CeO$_{2-\delta}$ composites are also stable in 1 M HCl solution. This is confirmed by the stability of the charge storage of PANI-ES@CeO$_{2-\delta}$-SS during the long cycling in this acidic electrolyte solution (Fig. S2, Supp.Data). Upon cycling, PANI@CeO$_{2-\delta}$-SS electrode is kept in the electrolyte overnight, after which the same charge storage behavior was measured. TG curve of such cycled electrode powder was identical to the one for the raw powder, thus confirming the same oxide fraction in the composite. It can be concluded that a strong adhesion of PANI with the cerium
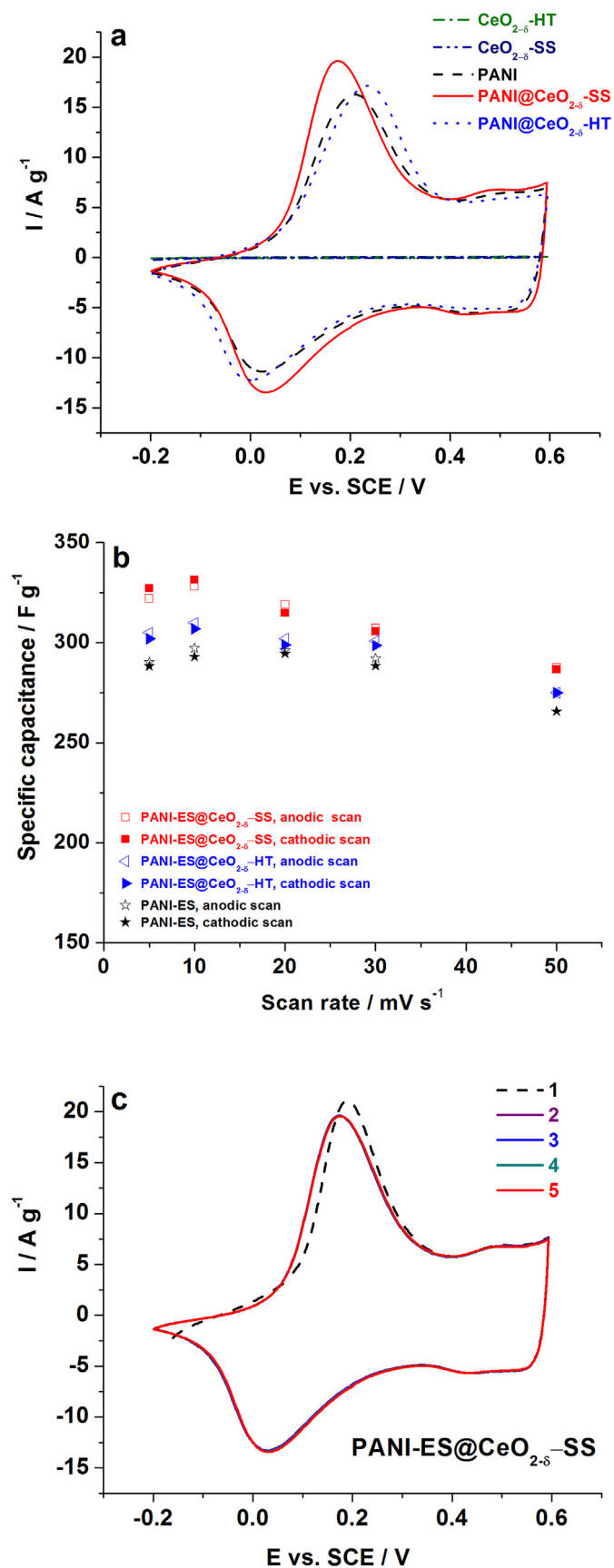
Fig. 5. a) Stabilized CVs of PANI-ES, $CeO_{2-\delta}$, and PANI-ES@$CeO_{2-\delta}$ composites; b) Specific capacitance of PANI-ES, PANI-ES@$CeO_{2-\delta}$-HT, and PANI-ES@$CeO_{2-\delta}$-SS at different scan rates; c) The cyclic stability of PANI-ES@$CeO_{2-\delta}$-SS. The electrolyte was 1 M HCl. The voltage range was 0.2–0.6 V vs. SCE and the scan rate was 20 mV s^{-1}.

oxide surface prevents the oxide from its possible slow dissolution in 1 M HCl. The fact that the cerium oxide in the composite is encapsulated into the shell of polymer chains favors this assumption.

The higher capacitance was obtained for PANI-ES@$CeO_{2-\delta}$-SS, which makes this composite a very promising supercapacitor electrode. Its stable capacitance during consecutive cycling (Fig. 5c and Fig. S2) indicates the stable leucoemeraldine-emeraldine redox process. A small capacity decrease, with the increase of the scan rate, was measured (Fig. 5b).

3.5.2. Extended voltage interval

It is known that over-oxidation of PANI in an acidic solution by applying potentials above ~0.6–0.7 V vs. SCE, results in its capacity decrease. Because of that, the cycling behavior in the deeper positive-going scan (beyond 0.6 V vs. SCE) was rarely examined [39]. Among other things, the idea of this work is to see how the presence of nonstoichiometric cerium-oxide influences the electrochemical over-oxidation of polyaniline.

CVs of all three samples, measured in an extended potential range from −0.2−1 V vs. SCE during ten consecutive cycles were shown in Fig. 6. In the first cycle, beside the main redox couple I (positioned at 0.22/0.01 V vs. SCE), which originates from the oxidation of leucoemeraldine base (LM) to emeraldine salt, one can see another main redox pair (labeled as III) at 0.8/0.65 V vs. SCE, corresponding to the emeraldine/pernigraniline (EM/PN) salt transition. A small redox pair II (0.55/0.45 V vs. SCE) positioned between these two main redox pairs can be also observed. Although the nature of this peak depends on the experimental details of polyaniline synthesis, electrolyte, and pH, this peak is generally attributed to the formation of benzoquinone degradation products and formation of cross-linked polyaniline chains by direct reaction between parts of the polyaniline chain itself [39]. One can see that the current of this middle redox couple increases during consecutive cycling of PANI within the extended water stability window, while the current of both LE-EM and EM-PN redox process decreases. Actually, over-oxidation of polyaniline leads to the irreversible formation of electrochemically inactive structures, which causes the current decrease throughout the consecutive cycling [37,39]. During experiments we noticed that the current of the second redox couple became more pronounced as soon as the current of the third peak has increased. One can conclude that the redox process corresponding to the second peak is still associated with the emeraldine-pernigraniline transformation.

Interestingly, some differences of the relative ratio of anodic peaks I and III can be observed between PANI and the $CeO_{2-\delta}$-modified PANI. A similar current response of these anodic peaks is observed for PANI and PANI@$CeO_{2-\delta}$-SS (Fig. 6a and b), indicating similar kinetics of the LE-EM and EM-PN redox processes in these samples. However, this is not the case for PANI-ES@$CeO_{2-\delta}$-HT (Fig. 6c) where the first anodic peak is noticeable higher than the third one. The process of the PN formation during PANI's oxidation is aggravated by $CeO_{2-\delta}$-HT action. The involvement of positively charged nitrogen in the interaction with cerium oxide impedes PANI-ES deprotonation, resulting in the lower fraction of formed PN upon the first anodic scan (Fig. 7a) and consequently the slower disappearance of the third peak after ten cycles (Fig. 7b). As a result, slightly better capacitance retention of PANI@$CeO_{2-\delta}$-HT (83.4% after 10 cycles or 64.4% after 30 cycles) was observed with respect to the pure PANI (80.8% after 10 cycles or 60.5% after 30 cycles) and PANI@$CeO_{2-\delta}$-SS (76.8% after 10 cycles and 55.6% after 30 cycles).

3.6. PANI-$CeO_{2-\delta}$ interaction
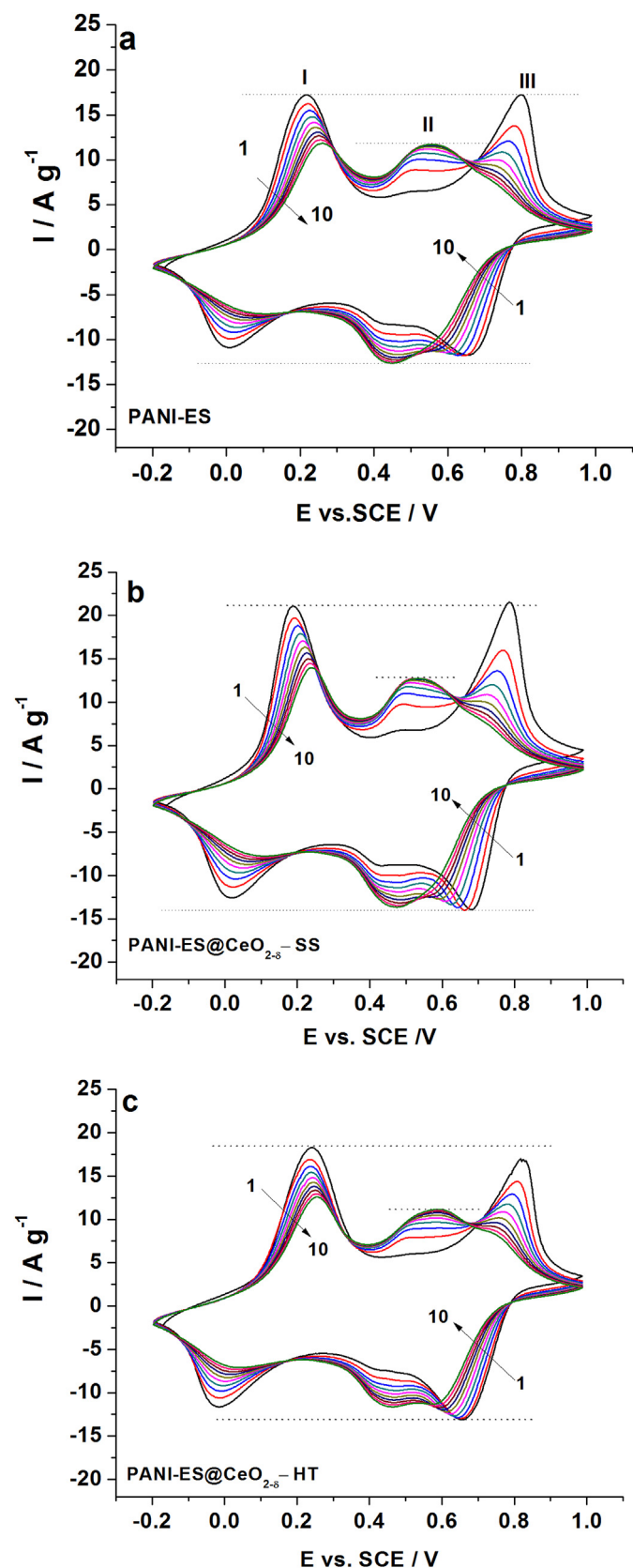
Polyaniline chains can change their redox state from a

Fig. 6. CVs of PANI (a), PANI@CeO$_{2-\delta}$-SS (b) and PANI@CeO$_{2-\delta}$-HT (c) measured in wide potential interval from −0.2–1 V vs. SCE during 10 successive cycling, at a common scan rate at 20 mV s^{-1}.
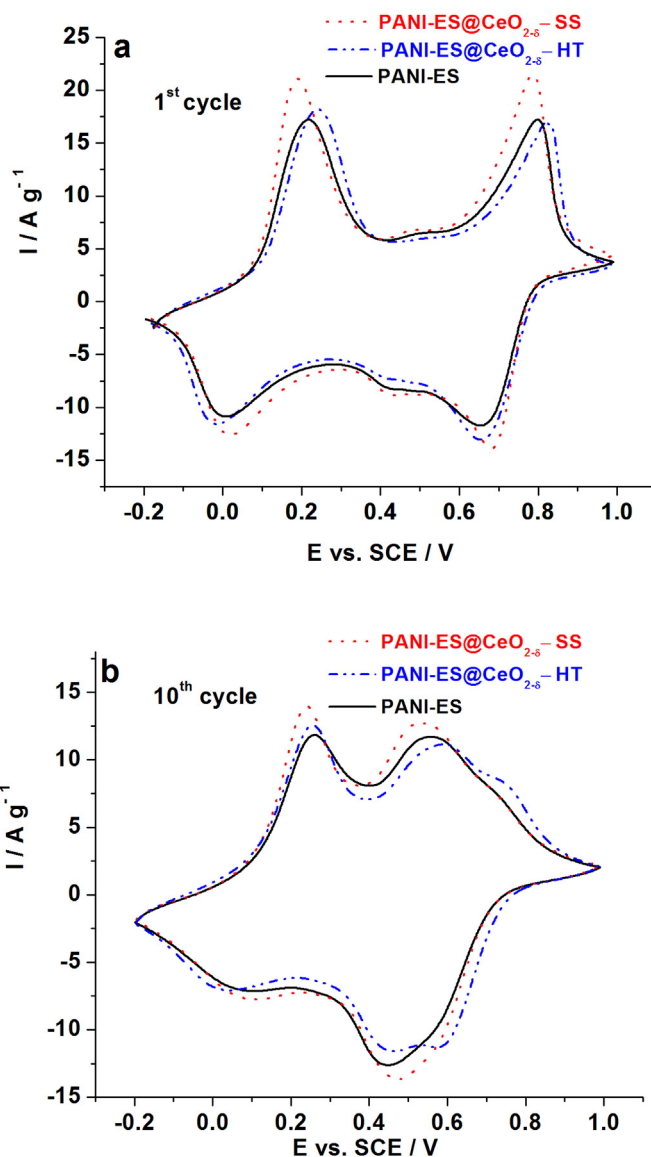

Fig. 7. CVs of PANI-ES, PANI-ES@CeO$_{2-\delta}$-SS and PANI-ES@CeO$_{2-\delta}$-HT samples measured in HCl at a common scan rate of 20 mV s^{-1}: a) the 1st cycle and b) 10th cycle.

completely reduced form (leucoemeraldine), composed of benzenoid units containing amine nitrogen atoms −NH−, to a fully oxidizied form (pernigraniline), composed of quinoid units containing imine nitrogen atoms −N =. A semi-oxidized form of polyaniline, known as emeraldine (either in the form of base or salt), is composed from equal numbers of reduced and oxidized polymer repeat units. The protonation of the emeraldine base, under acidic conditions, includes the addition of protons to imine nitrogen sites to generate radical cations (some amine nitrogen atoms can also be protonated to give NH$_2^+$ groups even if all the imines are not protonated), which can significantly increase the conductivity of polyaniline (up to 11 orders of magnitude) [25,40], reaching the metallic values.

On the other hand, cerium oxide crystallized in the fluorite type cubic crystal lattice where the Ce^{4+} cation is surrounded by eight O^{2-} anions, each of which is coordinated to four Ce^{4+} cations. Both theoretical and experimental results revealed that in oxygen deficient cerium oxide the adsorbed water molecules prefer to dissociate near the oxygen vacancy sites thus forming surface hydroxyl

groups [41,42]. Therefore, both chemisorbed H_2O and OH groups coexist at the reduced cerium oxide surface, so their presence can be expected at the surface of the $CeO_{2-\delta}$-SS and $CeO_{2-\delta}$-HT oxides, as confirmed by their FTIR spectra (inset in Fig. 3, O−H stretching vibrations around 3500 cm^{-1}). Their lower content in the $CeO_{2-\delta}$-HT can be correlated to the lower reactivity of surface towards the water dissociation, due to the smaller fraction of oxygen vacancies.

The experimentally determined pH values of $CeO_{2-\delta}$-SS, at zero point of charge (pH$_{ZPC}$ = 6.3), showed that the oxide surface became positively charged in the reaction solution of HCl (Fig. 8). Namely, surface hydroxyl groups are protonated, according to the equation

$$Ce-OH + H^+ \leftrightarrow Ce-OH_2^+$$

Such formed positively charged cerium oxide nanoparticles can electrostatically attract Cl^- ions from the acidic solution (Fig. 8a).

The adsorbed Cl^- ions can easily attract the anilinium cation (formed by adding aniline into acidic solution) which undergoes further polymerization to the emeraldine salt when the oxidant is added in the acidic medium. Consequently, there is possibility that various oligomers with an active radical cation head (positive head) are adsorbed to the surface of $CeO_{2-\delta}$ particles as well, but this possibility is reduced by the fact that the adsorption centers of cerium oxide were previously saturated with protonated aniline species. In this way, $CeO_{2-\delta}$ particles become wrapped into PANI chains thus forming the "core-shell" nanostructure. This type of structure has been already recognized for polyaniline/cerium oxide system [6,7,12,43−45]. These data showed that the interaction of protonated form of polyaniline with $CeO_{2-\delta}$ is usually achieved through the formation of hydrogen bond between surface hydroxyl (−OH) groups of oxide and hydrogen of the polymer chain [6,44−46]. Based on both Raman and FTIR measurements, the similar type of interaction is also identified in as-synthesized PANI@$CeO_{2-\delta}$ composites. Namely, zeta potential-pH dependence, measured for oxygen deficient cerium oxide [21], revealed that the maximum positive charge, at the surface, was achieved for the pH solution of about 4−5. Besides, some of OH groups at the cerium-oxide surface can be found un-protonated, thus participating in the formation of hydrogen bonds, acting as the bridge between polymer and oxide (Fig. 8b). This type of interaction is more pronounced in the $CeO_{2-\delta}$-SS since the higher fraction of oxygen vacancies (relative to $CeO_{2-\delta}$-HT) results in the higher amount of hydroxyl groups. Besides, another type of oxide-polyaniline interaction (Fig. 8c), involving positively charged nitrogen (-N$^{\bullet+}$H-), is identified by vibrational spectroscopy study. This interaction is found to be stronger in the case of composite with the hydrothermally synthesized oxide, which has the smaller oxygen vacancy population (i.e. higher concentration of Ce^{4+} ions). Theoretical

study on $CeO_{2-\delta}$ revealed that the electrons can be localized at cerium ions or oxygen vacancies [35]. Having in mind, that the nitrogen-involved interaction is more manifested in $CeO_{2-\delta}$-HT than in $CeO_{2-\delta}$-SS, and easier reduction of Ce^{4+} to Ce^{3+} ions, one can assume that delocalized π electrons of polymer chains became localized at 4f states of cerium ions. This may result in the decreased of the electronic conductivity of PANI when bonded to cerium oxide, following the trend PANI, PANI-ES@$CeO_{2-\delta}$-SS and PANI-ES@$CeO_{2-\delta}$-HT. Also, it could be responsible for the higher amount of bonded $CeO_{2-\delta}$-HT and consequently improved thermal stability of PANI-ES@$CeO_{2-\delta}$-HT composite. The mechanism of PANI-$CeO_{2-\delta}$ interaction is illustrated in Fig. 9.

A small amount of oxide (about 4%wt), incorporated into the shell of conducting polymer, was found to decrease its conductive behavior (in the extent that depends on properties of the used oxides), but conversely to improve its charge storage capability. The interactions at the PANI@$CeO_{2-\delta}$ interface weakened the polymer interchain bonds providing an easier attraction of electrolyte ions. Whether the higher amount of $CeO_{2-\delta}$ can improve electrochemical performance even more is the main question which arises here? Our attempt to answer this question, by increasing the amount of doped $CeO_{2-\delta}$ oxide during the synthesis, failed. Interestingly, PANI was not capable to bind a higher amount of $CeO_{2-\delta}$ (under applied synthesis conditions) regardless to the increase of its initial amount into reaction medium. Actually, the doubling of the initial content of $CeO_{2-\delta}$ (from 50 mg to 100 mg) for the aniline oxidation did not increase the content of bonded-$CeO_{2-\delta}$ at all. Such behavior is opposite to the case of TiO_2 added upon aniline oxidation, under completely same experimental conditions. In a set of separated experiments we showed that the initial amounts of 9 mg, 50 mg and 100 mg of TiO_2 (under same synthesis conditions), resulted in the ~4 wt%, ~18 wt% and ~34 wt% of oxide (calculated per mass of dried sample), in the composites (Fig. S3), respectively, which is in agreement with results of Bian et al. [18]. We try to explain this peculiar behavior using TG analysis. It can be seen from TG curves of composites, doped with a small percent (3−4%) of either $CeO_{2-\delta}$ (Fig. 1) or TiO_2 (Fig. S1), that the presence of such doped concentration did not change the final amount of internal dopant (HCl) in the composite. One can suggest that the type of interaction of these oxides in the case of their small doped fraction is similar i.e. both oxides coexist together with Cl^- ions (some of the Cl^- ions are adsorbed on the protonated hydroxyl groups) thus interacting also with hydrogen/nitrogen and weakening PANI's bonds with dopant. Furthermore, it can be seen that the amount of doped acid is noticeably decreased after mixing PANI with the higher percent (18% or 34%) of TiO_2 (Fig. 1). By competing with dopant ions for the positions of chains (close to the nitrogen atoms) during the synthesis, titanium oxide molecules (in higher concentration), are capable to eliminate some of dopant ions thus making complex
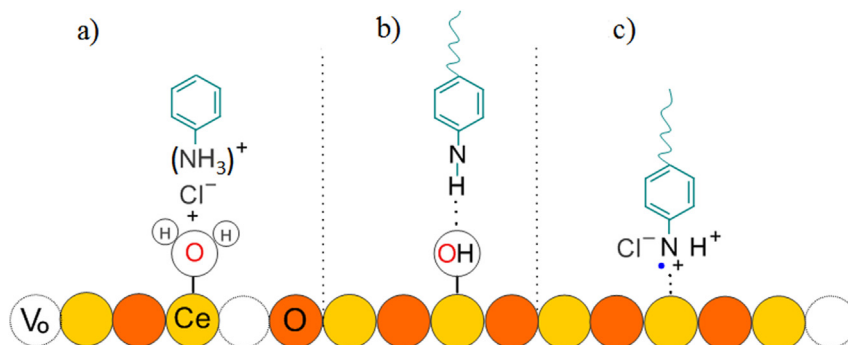

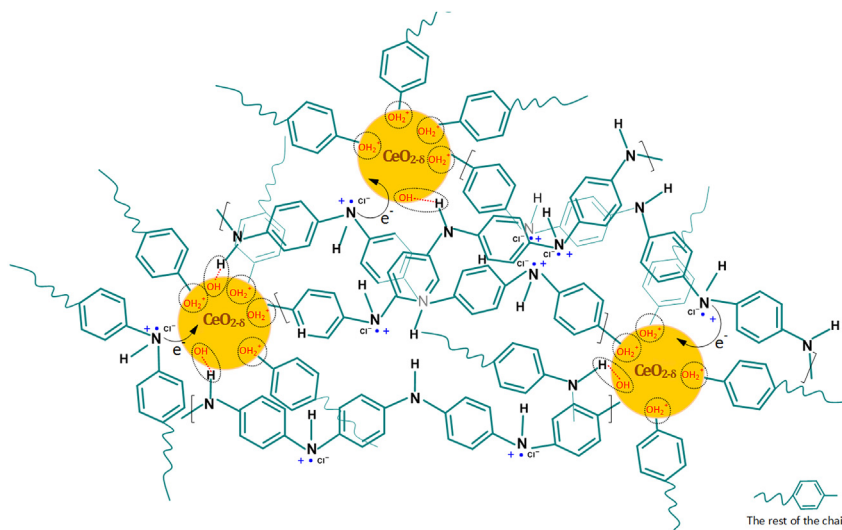**Fig. 8.** The initial stage of polymerization (a) and hydrogen (b) and nitrogen-involved interactions (c).

Fig. 9. Schematic illustration of the formation of PANI chains on the surface of CeO$_{2-\delta}$ nanoparticles (core-shell structure).

with nitrogen atoms of PANI. It could be related to a strong tendency of titanium to form coordination compounds with nitrogen [47]. On the other hand, nano-CeO$_{2-\delta}$, in spite of the higher concentration in the reaction solution, does not show this capability under the same experimental conditions, which resulted in its unsuccessful high-level bonding.

4. Conclusions

The use of non-stoichiometric cerium oxide as the adsorption center for the polymerization of aniline, in highly acidic conditions, influences thermal, electrical and charge storage properties of the formed emeraldine salt. These changes are the consequence of the strong interaction of polyaniline chains with cerium oxide ultrafine nanoparticles. The oxygen vacancies control indirectly the intensity of these interactions. A higher fraction of O-vacancies in CeO$_{2-\delta}$ promotes the dissociation of chemisorbed H$_2$O to OH groups at the oxide's surface, which in the protonated form, play the role of chemically active sites for the growth of PANI chains. Besides, unprotonated hydroxyl groups of cerium oxide surface interact with the hydrogen of polymer chains through the formation of hydrogen bonds. A lower fraction of O-vacancies provides the higher concentration of Ce^{4+} ions into crystal lattice, thus intensifying the interaction of Ce^{4+} cation with the nitrogen of the polaron structure (C ~ N$^{\bullet+}$), through the trapping of electrons into localized 4f states of cerium ions.

By encapsulating small weight percent of oxygen deficient cerium oxide, into highly conductive emeraldine salt, the improvement of both thermal stability and charge storage behavior is achieved. The highest and stable capacitance, amounting to 314 F g^{-1}, was obtained for the oxide with the higher degree of deficient oxygen (PANI-ES@CeO$_{2-\delta}$-SS), thus making this material promising as electrode for supercapacitors.

Appendix A. Supplementary data

Supplementary data to this article can be found online at https://doi.org/10.1016/j.electacta.2019.03.135.

References

[1] H. Wang, J. Lin, Z.X. Shen, Polyaniline (PANi) based electrode materials for energy storage and conversion, J. Sci. Adv. Mater. Dev. 1 (2016) 225.
[2] F.-Y. Chuang, S.-M. Yang, Cerium dioxide/polyaniline core–shell nanocomposites, J. Colloid Interface Sci. 320 (2008) 194.
[3] S. Daikh, F.Z. Zeggai, A. Bellil, A. Benyoucef, Chemical polymerization, characterization and electrochemical studies of PANI/ZnO doped with hydrochloric acid and/or zinc chloride: differences between the synthesized nanocomposites, J. Phys. Chem. Solids 121 (2018) 78.
[4] H. Wei, X. Yan, S. Wu, Z. Luo, S. Wei, Z. Guo, Electropolymerized polyaniline stabilized tungsten oxide nanocomposite films: electrochromic behavior and electrochemical energy storage, J. Phys. Chem. C 116 (2012) 25052.
[5] C.-G. Wu, D.C. DeGroot, H.O. Marcy, J.L. Schindler, C.R. Kannewurf, Y.-J. Liu, W. Hirpo, M.G. Kanatzidis, Redox intercalative polymerization of aniline in V2O5 xerogel. The postintercalative intralamellar polymer growth in polyaniline/metal oxide nanocomposites is facilitated by molecular oxygen, Chem. Mater. 8 (1996) 1992.
[6] C. Liu, H. Tai, P. Zhang, Z. Yuan, X. Du, G. Xie, Y. Jiang, A high-performance flexible gas sensor based on self-assembled PANI-CeO2 nanocomposite thin film for trace-level NH3 detection at room temperature, Sens. Actuators B Chem. 261 (2018) 587.
[7] L. Wang, H. Huang, S. Xiao, D. Cai, Y. Liu, B. Liu, D. Wang, C. Wang, H. Li, Y. Wang, Q. Li, T. Wang, Enhanced sensitivity and stability of room-temperature NH3 sensors using core-shell CeO2 Nanoparticles@Cross-linked PANI with p–n heterojunctions, Appl. Mater. Interfaces 6 (2014) 14131.
[8] A.A. Ansari, G. Sumana, R. Khan, B.D. Malhotra, Polyaniline-cerium oxide nanocomposite for hydrogen peroxide sensor, J. Nanosci. Nanotechnol. 9 (2009) 4679.
[9] N. Parvatikar, S. Jain, S.V. Bhoraskar, M.V.N.A. Prasad, Spectroscopic and electrical properties of polyaniline/CeO2 composites and their application as humidity sensor, J. Appl. Polym. Sci. 102 (2006) 5533.
[10] M. Singh, N. Nesakumar, S. Sethuraman, U. Maheswari, Journal of Colloid and Interface Science Electrochemical biosensor with ceria – polyaniline core shell nano-interface for the detection of carbonic acid in blood, J. Colloid Interface Sci. 425 (2014) 52.
[11] M.B. Gumpu, N. Nesakumar, S. Sethuraman, U.M. Krishnan, J.B.B. Rayappan, Electrochemical biosensor with ceria-PANI core-shell nano-interface for the detection of histamine, Sens. Actuators B Chem. 199 (2014) 330.
[12] H. Huang, Z. Guo, Preparation and characterization of conductive polyaniline/cerium dioxide composites, Mater. Sci. Forum 663–665 (2011) 686.
[13] S. Wang, Z. Huang, J. Wang, Y. Li, Z. Tan, Thermal stability of several

polyaniline/rare earth oxide composites (I): polyaniline/CeO2 composites, J. Therm. Anal. Calorim. 107 (2012) 1199.

[14] B. Ramezanzadeh, G. Bahlakeh, M. Ramezanzadeh, Polyaniline-cerium oxide (PAni-CeO2) coated graphene oxide for enhancement of epoxy coating corrosion protection performance on mild steel, Corros. Sci. 137 (2018) 111.

[15] N. Maheswari, G. Muralidharan, Fabrication of CeO2/PANI composites for high energy density supercapacitors, Mater. Res. Bull. 106 (2018) 357.

[16] Q. Gong, Y. Li, H. Huang, J. Zhang, T. Gao, G. Zhou, Shape-controlled synthesis of Ni-CeO2@PANI nanocomposites and their synergetic effects on super-capacitors, Chem. Eng. J. 344 (2018) 290.

[17] Y. Fei, H. Huang, S. Song, L. Jin, X. Zhang, Z. Guo, Preparation of thermostable and electroconductive PANI/TDI–CeO2 composite by graft polymerization and its electrochemical properties, Int. J. Electrochem. Sci. 13 (2018) 1308.

[18] C. Bian, Y. Yu, G. Xue, Synthesis of conducting polyaniline/TiO2 composite nanofibres by one-step in situ polymerization method, J. Appl. Polym. Sci. 104 (2007) 21.

[19] S. Phokha, S. Pinitsoontorn, P. Chirawatkul, Y. Poo-arporn, S. Maensiri, Synthesis, characterization, and magnetic properties of monodisperse CeO 2 nanospheres prepared by PVP-assisted hydrothermal method, Nanoscale Ress. Lett. 7 (2012) 425.

[20] X. Yu, F. Li, X. Ye, X. Xin, Synthesis of cerium(IV) oxide ultrafine particles by solid-state reactions, J. Am. Ceram. Soc. 83 (2000) 964.

[21] N. Tomić, Z.D. Dohčević-Mitrović, N.M. Paunović, D.Ž. Mijin, N.D. Radić, B.V. Grbić, S.M. Aškrabić, B.M. Babić, D.V. Bajuk-Bogdanović, Nanocrystalline CeO2−δ as Effective Adsorbent of Azo Dyes 30 (2014) 11582.

[22] Y. Wei, K.F. Hsueh, Thermal analysis of chemically synthesized polyaniline and effects of thermal aging on conductivity, J. Polym. Sci., Part A: Polym. Chem. 27 (1989) 4351.

[23] M. Trchová, J. Stejskal, Polyaniline: the infrared spectroscopy of conducting polymer nanotubes, Pure Appl. Chem. 83 (2011) 1803—1817, https://doi.org/10.1351/PAC-REP-10-02-01.

[24] M. Hasik, C. Paluszkiewicz, E. Bielánska, Reactions of Polyaniline with Transition Metal Ions in Nonaqueous Solutions, 2005, pp. 744—747, 677.

[25] Z. Ping, In situ FTIR-attenuated total reflection spectroscopic investigations on the base-acid transitions of polyaniline, J. Chem. Soc., Faraday Trans. 92 (1996) 3063.

[26] M. Lohrasbi, N. Hedayat, S.S.C. Chuang, In-situ infrared study of the synthesis of polyaniline under acid and neutral pH, Top. Catal. 57 (2014) 1570.

[27] M. Trchová, Z. Morávková, I. Šeděnková, J. Stejskal, Spectroscopy of thin polyaniline films deposited during chemical oxidation of aniline, Chem. Pap. 66 (2012) 415.

[28] M. Hasik, A. Drelinkiewicz, E. Wenda, C. Paluszkiewicz, S. Quillard, FTIR spectroscopic investigations of polyaniline derivatives-palladium systems, J. Mol. Struct. 596 (2001) 89.

[29] M. Trchová, I. Šeděnková, E.N. Konyushenko, J. Stejskal, P. Holler, G. Ćirić-Marjanović, Evolution of polyaniline nanotubes: the oxidation of aniline in water, J. Phys. Chem. B 110 (2006) 9461.

[30] M.R. Devi, B. Lawrence, N. Prithivikumaran, N. Jeyakumaran, Synthesis and

characterization of conducting polymer Polyaniline doped with Salicylic Acid, Int.J. ChemTech Res. 6 (2014) 5400.

[31] G. Ćirić-Marjanović, M. Trchová, J. Stejskal, The chemical oxidative polymerization of aniline in water: Raman spectroscopy, J. Raman Spectrosc. 39 (2008) 1375.

[32] G.M. do Nascimento, V.R.L. Constantino, R. Landers, M.L.A. Temperini, Aniline polymerization into montmorillonite clay: a spectroscopic investigation of the intercalated conducting polymer, Macromolecules 37 (2004) 937.

[33] M. Tagowska, B. Pałys, K. Jackowska, Polyaniline nanotubules - anion effect on conformation and oxidation state of polyaniline studied by, Raman spectroscopy 142 (2004) 223.

[34] B.Z. Wei, M. Wan, T. Lin, L. Dai, Polyaniline nanotubes doped with sulfonated carbon nanotubes made via a self-assembly, Adv. Mater. 15 (2003) 136.

[35] M. Radović, B. Stojadinovic, N. Tomić, A. Golubović, B. Matovic, I. Veljković, Z. Dohčević-Mitrović, Investigation of surface defect states in CeO2-y nano-crystals by Scanning-tunneling microscopy/spectroscopy and ellipsometry, J. Appl. Phys. 116 (2014) 234305.

[36] A. Drury, S. Chaure, M. Kröll, V. Nicolosi, N. Chaure, W.J. Blau, Fabrication and characterization of silver/polyaniline composite nanowires in porous anodic alumina, Chem. Mater. 19 (2007) 4252.

[37] E. Song, J.-W. Choi, Conducting polyaniline nanowire and its applications in chemiresistive sensing, Nanomaterials 3 (2013) 498.

[38] S. Popescu, M. Mîndroiu, D. Cabuzu, C. Pîrvu, The Roll of NaPSS Surfactant on the Ceria Nanoparticles Embedding in Polypyrrole Films, 2016, 2016, p. 1.

[39] R. Pauliukaite, C.M.A. Brett, A.P. Monkman, Polyaniline fibres as electrodes, Electrochemical characterisation in acid solutions 50 (2004) 159.

[40] A.G. MacDiarmid, A.J. Epstein, Conducting polymers: science and technology, in: P.N. Prasad (Ed.), Frontiers of Polymers and Advanced Materials, Plenum Press, New York, 1994, p. 251.

[41] Z. Yang, Q. Wang, S. Wei, D. Ma, Q. Sun, The effect of environment on the reaction of water on the ceria(111) surface: a DFT+U study, J. Phys. Chem. C 114 (2010) 14891.

[42] Lj Kundakovic, D.R. Mullins, S.H. Overbury, Adsorption and reaction of H2O and CO on oxidized and reduced Rh/CeOx(111) surfaces, Surf. Sci. 457 (2000) 51.

[43] E. Kumar, P. Selvarajan, D. Muthuraj, Preparation and characterization of polyaniline/cerium dioxide (CeO2) nanocomposite via in situ polymerization, J. Mater. Sci. 47 (2012) 7148.

[44] Y. Sasikumar, A.M. Kumar, Z.M. Gasem, E.E. Ebenso, Hybrid nanocomposite from aniline and CeO2 nanoparticles: surface protective performance on mild steel in acidic environment, Appl. Surf. Sci. 330 (2015) 207.

[45] F. Liu, H. Yongjun-He, J.-S. Huh, Study on the synthesis and characterization of PANi/nano-CeO2 composites, Solid State Phenom. 124−126 (2007) 287.

[46] Y. He, Synthesis of polyaniline/nano-CeO2 composite microspheres via a solid-stabilized emulsion route, Mater. Chem. Phys. 92 (2005) 134.

[47] X. Li, G. Wang, X. Li, D. Lu, Surface properties of polyaniline/nano-TiO2 composites, Appl. Surf. Sci. 229 (2004) 395.

Article

Photocatalytic Activity of the V$_2$O$_5$ Catalyst toward Selected Pharmaceuticals and Their Mixture: Influence of the Molecular Structure on the Efficiency of the Process

Sanja J. Armaković [1],[*] , Aleksandra Jovanoski Kostić [1] , Andrijana Bilić [1] , Maria M. Savanović [1] , Nataša Tomić [2] , Aleksandar Kremenović [3] , Maja Šćepanović [2] , Mirjana Grujić-Brojčin [2] , Jovana Ćirković [4] and Stevan Armaković [5]

[1] University of Novi Sad, Faculty of Sciences, Department of Chemistry, Biochemistry and Environmental Protection, 21000 Novi Sad, Serbia
[2] Center for Solid State and New Materials, Institute of Physics Belgrade, 11000 Belgrade, Serbia
[3] Laboratory of Crystallography, Faculty of Mining and Geology, University of Belgrade, Đušina 7, 11000 Belgrade, Serbia
[4] Institute for Multidisciplinary Research, University of Belgrade, 11000 Belgrade, Serbia
[5] University of Novi Sad, Faculty of Sciences, Department of Physics, 21000 Novi Sad, Serbia
[*] Correspondence: sanja.armakovic@dh.uns.ac.rs; Tel.: +381-21-485-2754

Abstract: Due to the inability of conventional wastewater treatment procedures to remove organic pharmaceutical pollutants, active pharmaceutical components remain in wastewater and even reach tap water. In terms of pharmaceutical pollutants, the scientific community focuses on β-blockers due to their extensive (over)usage and moderately high solubility. In this study, the photocatalytic activity of V$_2$O$_5$ was investigated through the degradation of nadolol (NAD), pindolol (PIN), metoprolol (MET), and their mixture under ultraviolet (UV) irradiation in water. For the preparation of V$_2$O$_5$, facile hydrothermal synthesis was used. The structural, morphological, and surface properties and purity of synthesized V$_2$O$_5$ powder were investigated by scanning electron microscopy (SEM), X-ray, and Raman spectroscopy. SEM micrographs showed hexagonal-shaped platelets with well-defined morphology of materials with diameters in the range of 10–65 μm and thickness of around a few microns. X-ray diffraction identified only one crystalline phase in the sample. The Raman scattering measurements taken on the catalyst confirmed the result of XRPD. Degradation kinetics were monitored by ultra-fast liquid chromatography with diode array detection. The results showed that in individual solutions, photocatalytic degradation of MET and NAD was relatively insignificant (<10%). However, in the PIN case, the degradation was significant (64%). In the mixture, the photodegradation efficiency of MET and NAD slightly increased (15% and 13%). Conversely, it reduced the PIN to the still satisfactory value of 40%. Computational analysis based on molecular and periodic density functional theory calculations was used to complement our experimental findings. Calculations of the average local ionization energy indicate that the PIN is the most reactive of all three considered molecules in terms of removing an electron from it.

Keywords: β-blocker; nadolol; pindolol; metoprolol; photocatalysis; nanomaterial characterization; DFT analysis

1. Introduction

The World Health Organization noted in its reports that pharmaceuticals are present in natural and treated water in concentrations from 0.1 to 0.05 mg/L [1]. Among all pharmaceuticals, a large increase was noted for β-blockers due to an increase in cardiovascular diseases [2]. Because of their moderately high solubility [3] and incomplete removal by wastewater treatment plants, β-blockers are persistent in water environments and they may show potential toxic properties against nontarget organisms, i.e., aquatic organisms

and even human health. For example, metoprolol (MET, Figure 1) is one of the most used medicines in this class, and its usage increased four times in recent years [4]. Pindolol (PIN, Figure 1) possesses lipophilic properties and at natural pH is almost completely insoluble in water [5,6]. Nadolol (NAD, Figure 1) is another medicine from the β-blockers class, which is highly soluble in water and hydrolytically stable, and thanks to that property, is highly bioavailable in the environment [7,8]. Usually, β-blockers are present in the environment in combination with other β-blockers and various organic pollutants. Their mutual reactions may manifest additional health and environmental risks caused by unexpected interactions between them.
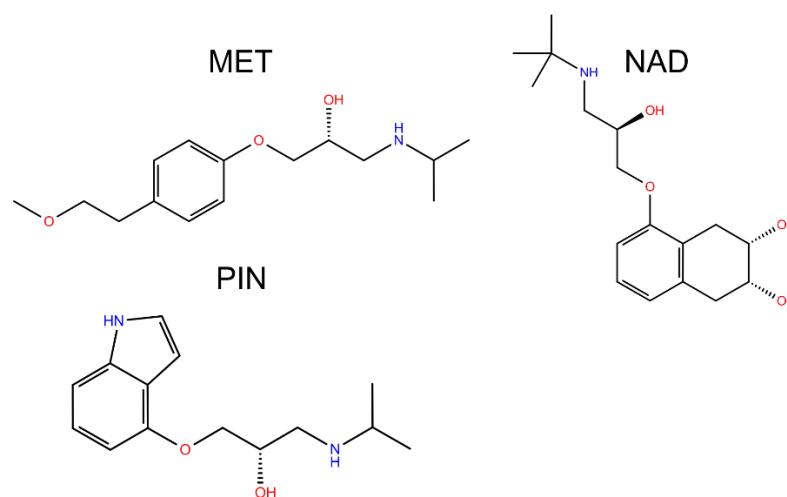

Figure 1. Structural formulas of studied beta blockers.

Conventional water treatment plants (WWTPs) lack the potential to remove emerging pollutants, such as pharmaceuticals, especially β-blockers [9]. The poor efficiency of conventional WWTPs in removing β-blockers is proven by the presence of β-blockers in various water organisms [10]. The average removal efficiency of these compounds is around 30–40% [11]. The degradation of individual β-blockers depends on various factors, such as temperature, pH value, compound's polarity, cation-exchange properties, biodegradability, etc. [12]. Multiple strategies have been applied in their removals, such as adsorption [13], chemical treatment for tackling water contamination, and advanced oxidation processes (AOPs) [14,15]. However, to achieve easy operation, low equipment cost, and cheap raw materials, AOPs are highly desirable. In addition, AOP, such as photodegradation, is considered most commonly used due to its ability to remove most organic pollutants from water [16]. To prevent and eliminate their unexpected toxic properties, there is a need for new efficient methods and materials for β-blockers removal from the water environment. A slow degradation rate during photolysis requires catalysts activated by interaction with light, after which the degradation process is more efficient [8]. For more than ten years, semiconductor-based photocatalysts have focused on water purification because of their high potential for the degradation of pollutants [17]. Some latest photocatalysts used are nanocrystalline M-type hexaferrite $Ca_{0.5}Pb_{0.5}-xYb_xZn_yFe_{12-y}O_{19}$ synthesized by sol–gel autocombustion method [15], the $C_3N_{4x}/AgO_y@Co_{1-x}Bi_{1-y}O_7$ synthesized by the combination of sol–gel and annealing approaches [14], porous methacrylic organosilica materials (Ag@PMOS) synthesized by reducing the silver moieties on and in the surfaces of porous methacrylic organic silicates [18], V_2O_5 nanoparticles [19], V_2O_5 nanorods [20], etc.

Vanadium oxide is a compound with colossal potential in water treatment because of its capability of light absorption, lower bandgap (2.3 eV) than TiO_2 and ZnO, chemical stability, and surface catalytic properties [21–25]. Following previously obtained results (Table 1), the V_2O_5 catalyst showed significant photocatalytic activity toward various organic pollutants [21,23–27]. Most studied molecules are branched with at least one aromatic ring and nitrogen and oxygen atoms in their structure. Degradation pathways and degra-

dation rate is determined by the nature of substituents on aromatic rings [25]. For example, Fu et al. noted that surface OH groups play a vital role in increasing the degradation rate of nitrobenzene and methylene blue after introducing Al_2O_3 particles. The structural similarity of previously investigated compounds and selected β-blockers and obtained results in those experiments served as a starting point for this research.

Table 1. Some previous research on the photocatalytic activity of V_2O_5 toward organic pollutants.

Synthesis Method	Compounds	Irradiation	Efficiency	Reference
Hydrothermal method V_2O_5 pure vanadium pentoxide nanoparticles	Methyl orange (MO) Congo red (CR)	Visible light	After 180 min degradation of MO was 82% and CR was 99.61%	[21]
Coprecipitation—calcination V_2O_5/Al_2O_3 composite photocatalyst The highest activities were obtained for the sample with the V/Al ratio of 1:1	Reduction of Cr(VI), nitrobenzene (NB), and degradation of methylene blue (MB)	UV	After irradiation for 20, 300, and 20 min, the highest removal (or conversion) efficiencies for Cr(VI), NB, and MB over the optimal sample were found to be 79%, 67%, and 31%, respectively	[23]
Ultrasound-assisted V_2O_5 nanoparticles	Rose Bengal dye (RB)	Solar light	After 150 min degradation of RB was around 99%	[24]
Chemical precipitation from ammonium metavanadate using Triton X-100 as surfactant V_2O_5 powder	Phenol and derivatives	Natural sunlight	No contribution to the photocatalytic process	[25]
Growing radially on PET fibers V_2O_5 nanoflakes	Rhodamine B (RhB)	Visible light	After 60 min degradation of RhB was around 50%	[26]
Simple thermal decomposition method V_2O_5/ZnO nanocomposites	MB	Visible light	After 120 min degradation of MB was around 97%	[27]

In this paper, we investigate the photocatalytic properties of V_2O_5 nanopowder for the degradation of three β-blockers (MET, NAD, and PIN) separately and in a mixture. Several methods of characterization, such as X-ray powder diffraction (XRPD), scanning electron microscopy (SEM), energy-dispersive X-ray spectroscopy (EDS), Brunauer–Emmett–Teller (BET) measurements, Fourier transform infrared (FTIR) and Raman spectroscopy, are employed to correlate structural and morphological properties of synthesized nanopowders and their photocatalytic activity under ultraviolet (UV) irradiation. The efficiency of the photodegradation process was compared with the efficiency of direct photolysis (DF). The experimentally obtained results were correlated with the molecular and periodic DFT analysis to explain the influence of molecular structure on the efficiency of the degradation process.

2. Results and Discussion

2.1. XRPD

Only one crystalline phase Shcherbinaite, V_2O_5 (PDF card no. 01-072-0433; orthorhombic P*mnm* space group) could be identified in the sample, Figure 2. Refined unit cell parameter values (a = 11.506 (2), b = 4.3708 (6), c = 3.5627 (4) Å, V = 179.17 (4) Å^3) are in good agreement with reference values reported in upper mentioned PDF card (a = 11.5100, b = 4.3690, c = 3.5630 Å, V = 179.173 Å^3). The significant presence of an amorphous component is not evident. Crystallite-sized (1251(35) Å) and lattice strain (0.16(2)%) values point to well crystalline material with important lattice strain.
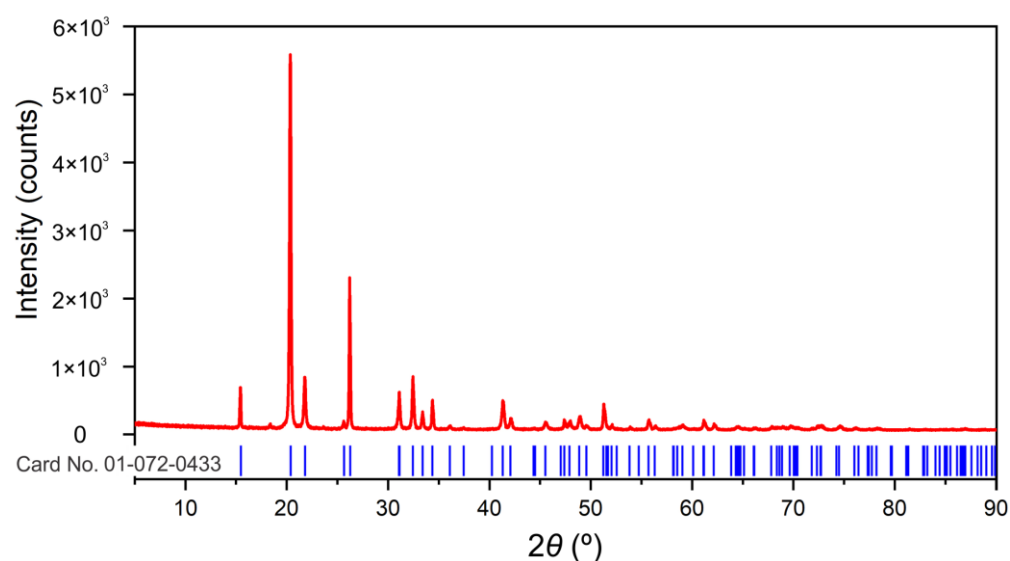
Figure 2. Experimental XRPD pattern in red. Peak positions for Shcherbinaite, V_2O_5 (card number 01-072-0433; ICDD (PDF-2 Release 2016 RDB)) in blue are shown below the experimental pattern.

2.2. SEM/EDS

By applying the hydrothermal method, where ammonium metavanadate was used as a precursor in an acidic media, hexagonal-shaped platelets with well-defined morphology were obtained as a major entity (Figure 3). The diameters of the platelets are in the range of 10–65 μm, whereas their thickness may be estimated to be a few microns. Rashed et al. [28] obtained similar information regarding the morphology, where the cetyltrimethylammonium bromide (CTAB) was used as a surfactant. Due to this, the thinner nanoflake particles were formed with an average diameter of ~70 nm for the sample annealed at 500 °C for 2 h. A similar procedure was conducted by Abdullah et al. [29] with the same surfactant: after annealing at 500 °C for 4 h, the nanoflakes with thicknesses close to 65–80 nm were obtained.
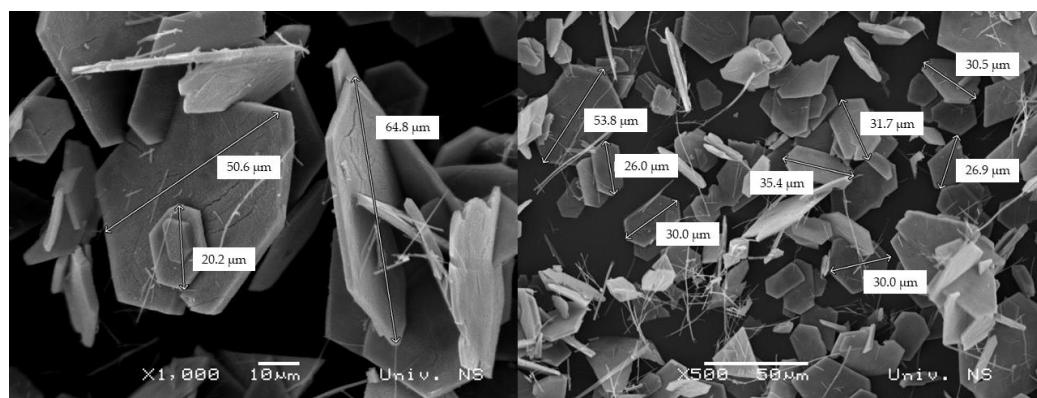
Figure 3. SEM micrographs of V_2O_5 powder with different magnifications.

The EDS analysis indicates that the main elements of the catalyst are vanadium and oxygen, and no other impurity elements could be detected (Figure 4). The atomic percentage of V and O in Spectrum 1 is estimated as 39.86% and 60.14%, respectively, indicating possible oxygen deficiency on the edge of the platelet. The values obtained in Spectrum 2, at the flat surface of the platelet, estimated as 25.47% for V and 74.53% for O, are close to the values of stoichiometric V_2O_5.

Figure 4. SEM image (**left**) with corresponding EDS spectra (**right**) of V_2O_5 catalyst.
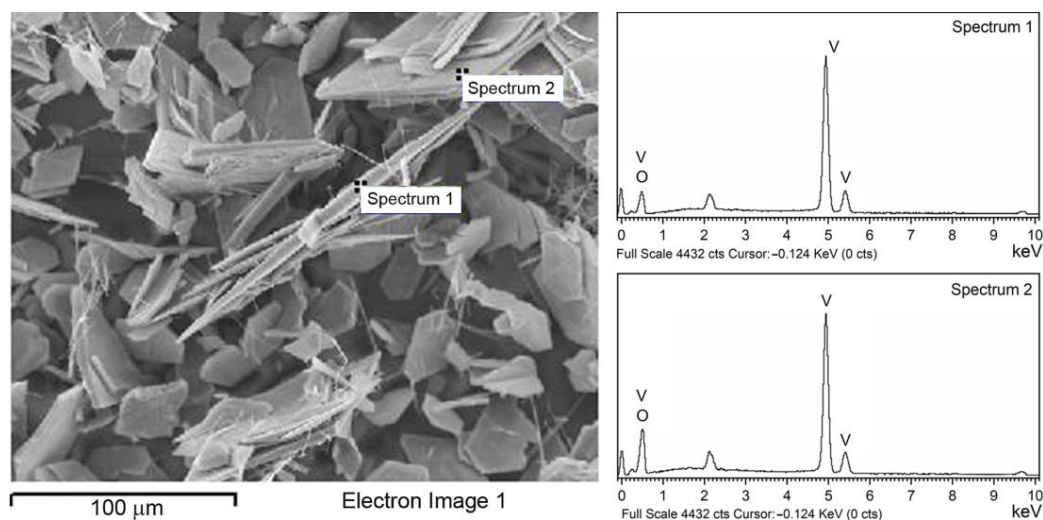
2.3. Raman Scattering Measurements

The Raman scattering measurements taken on the catalyst sample have confirmed the results of XRPD regarding orthorhombic α-V_2O_5 structure with P*mnm* symmetry. This structure is associated with 21 Raman active modes ($7_{Ag} + 3B_{1g} + 7B_{2g} + 4B_{3g}$) [30], 10 of which are registered in the spectrum shown in Figure 5. These modes are unambiguously assigned to α-V_2O_5 structure [30,31]: ~104(A_g), 146(B_{1g}/B_{3g}), 198 (A_g/B_{2g}), 285 (B_{1g}/B_{3g}), 306 (A_g), 406 (A_g), 483 (A_g), 528 (A_g), 701 (B_{1g}/B_{2g}), and 995 cm^{-1} (A_g). A good agreement of the position of the Raman mode at 995 cm^{-1} with corresponding bulk value, together with the absence of ~840 cm^{-1} mode in the spectra of the catalyst, reveals a good crystallinity of the V_2O_5 phase [30–32]. A broad feature at ~1020 cm^{-1} may be ascribed to surface VO_x species on V_2O_5 [33].
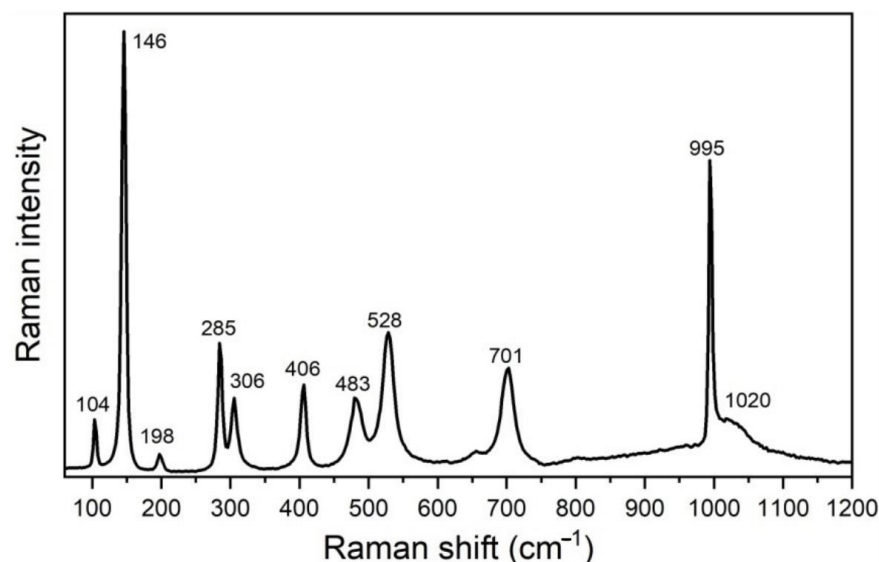

Figure 5. Experimental Raman spectrum of V_2O_5 catalyst (after a baseline correction).

2.4. UV-Vis

In order to estimate the energy bandgap of V_2O_5 powder, Kubelka–Munk functions $F(R)$ [34] were calculated as $F(R) = (1 − R)^2/2R$, where R is the diffuse reflectance of the

V_2O_5 sample. Taking into account that $F(R)$ is proportional to the absorption coefficient α, the Tauc plot [35] was obtained by using the following equation:

$$(h\nu\, F(R))^{1/n} = A\left(h\nu - E_g\right)$$

where h is Planck's constant, ν—photon's frequency, E_g—bandgap, A—proportional constant, and the n factor depends on the nature of the electron transition. They equal 1/2 or 2 for allowed direct and indirect transition band gaps [36]. The band gap values were deduced by extrapolating the linear portion of the curves to the energy axis, as shown in Figure 6. According to this procedure, the bandgap energy E_g values, assuming the allowed direct and indirect transitions, are estimated as ~2.24 and ~2.11 eV, respectively.
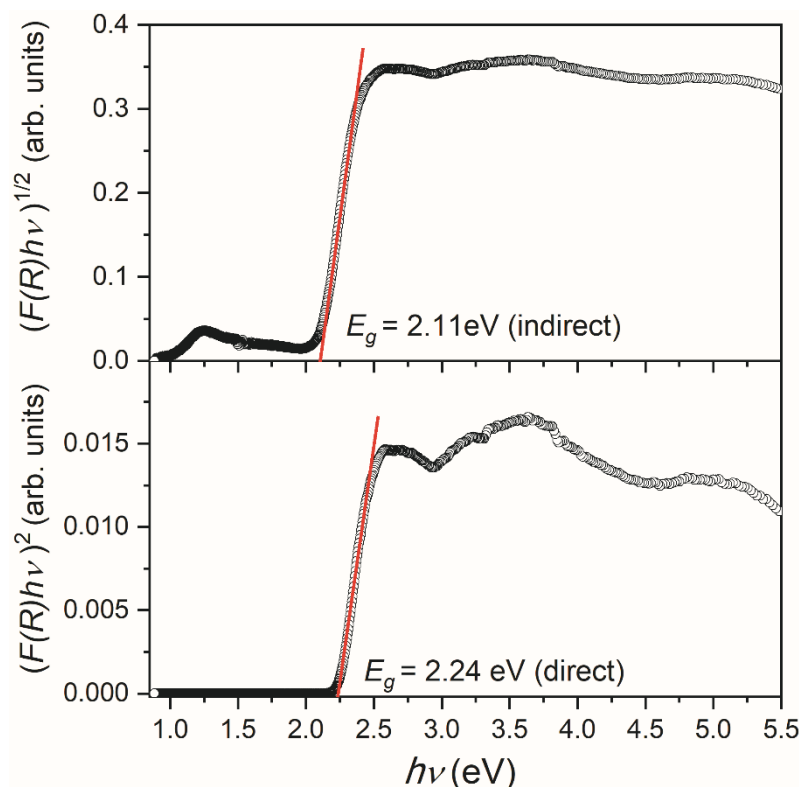

Figure 6. Transformed Kubelka–Munk functions $(F(R)\, h\nu)^2$ and $(F(R)\, h\nu)^{1/2}$ assuming direct and indirect energy bandgap in the V_2O_5 sample, respectively.

It should be noted that different V_2O_5 structures may undergo direct and indirect transitions, and it is not often easy to decide which type of electron inter-band transition is predominant [37]. According to a detailed analysis of available literature data and the film properties, Schneider concluded that the direct allowed transition could be considered the most probable in investigated V_2O_5 films [37]. Conversely, Mousavi et al. [38] have suggested the direct bandgap in the V_2O_5 nanoparticles based on the best line fitting of Kubelka–Munk functions. Still, in our case, it is impossible to decide the character of the allowed transition, considering the good quality of line fitting (Figure 6).

In this work, the DFT approach was used to perform band structure calculations to complement our experimental observations and to compare band gaps. The model of V_2O_5 was generated according to the previously mentioned information regarding the crystal structure of V_2O_5. The model of V_2O_5 was first subjected to geometrical optimization, followed by band structure calculations, using the PBE-D3 level of theory with Hubbard U value set to 3.5 eV for vanadium 3d states, a value reported to produce excellent results in terms of band gap for this material [39]. The obtained band structure is presented in Figure 7.
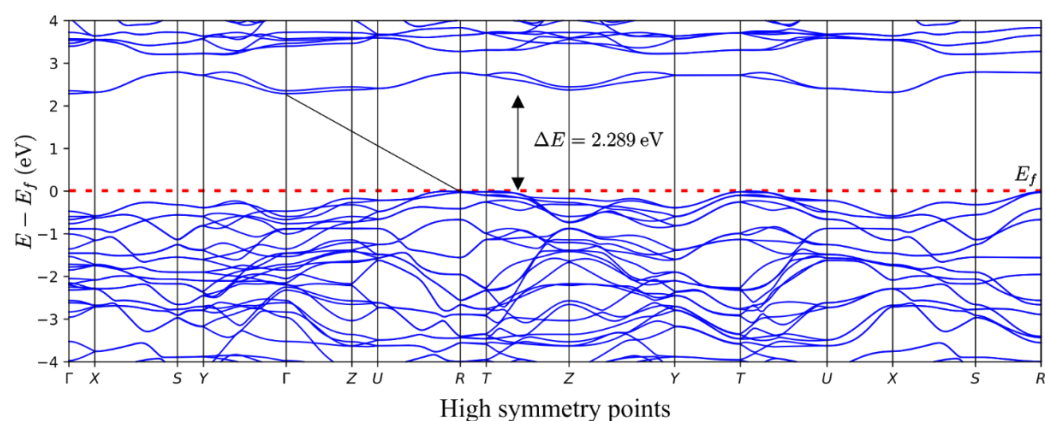
Figure 7. Band structure of V_2O_5. The red dotted line denotes the Fermi level. The black line connects the top of the valence and the bottom of the conduction zones.

As presented in Figure 7, it can be seen that the DFT calculations lead to excellent matching between experimental and computational results. Our DFT calculations indicate that an indirect band gap characterizes the V_2O_5. Additionally, the DFT + U approach utilized in this work yielded a band gap value of 2.289 eV, which is in excellent agreement with our experimental observations and reports of other research groups [40,41]. The importance of Hubbard U correction was essential for reaching this level of agreement. However, it is also interesting to note that the absence of Hubbard U correction led to a reasonably decent band gap value equal to 1.880 eV (again, with the indirect band gap type).

2.5. Photocatalytic Application

The photocatalytic activity of the V_2O_5 catalyst was studied through the photocatalytic degradation of NAD, PIN, and MET and their mixture. The results of the degradation efficiency were compared with the efficiency of DF.

Since light absorption is an important parameter influencing the degradation efficiency, we have also analyzed the excitations within studied pharmaceutical molecules. For these purposes, we have performed TD-DFT calculations with CAM-B3LYP functional and 6-311++G(d,p) basis set, which enabled us to simulate the UV spectra of the compounds mentioned above (Figure 8). The obtained results agree with the investigated compounds' experimental spectra.

Figure 8. (**a**) Computational and (**b**) experimental UV spectra of MET, NAD, and PIN.
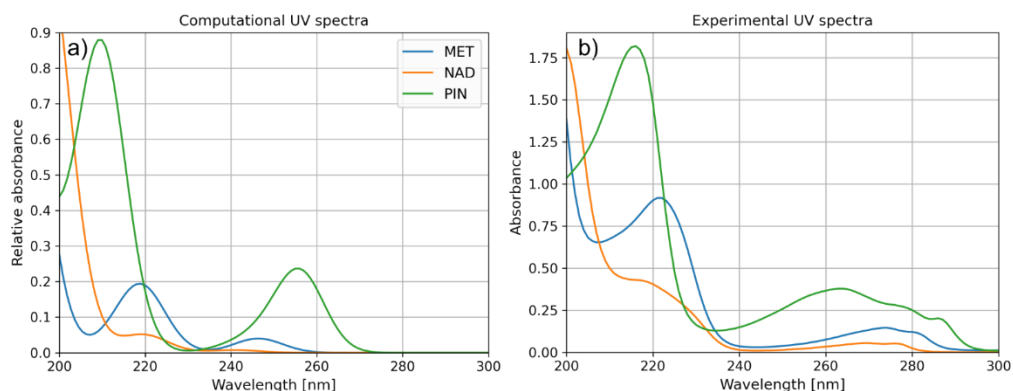
UV spectra presented in Figure 8 indicate one more interesting property of the PIN molecule, in line with the experimentally observed degradation efficiencies. Namely, aside from the excitations at wavelengths around 200 nm, the PIN molecule is also characterized by relatively strong light absorption at 260 nm. The stronger light absorption of the

molecule is significant for photocatalytically assisted degradation and, in the case of the present study, may be a crucial factor leading to the superior degradation efficiency of PIN over other molecules (Figure 9).
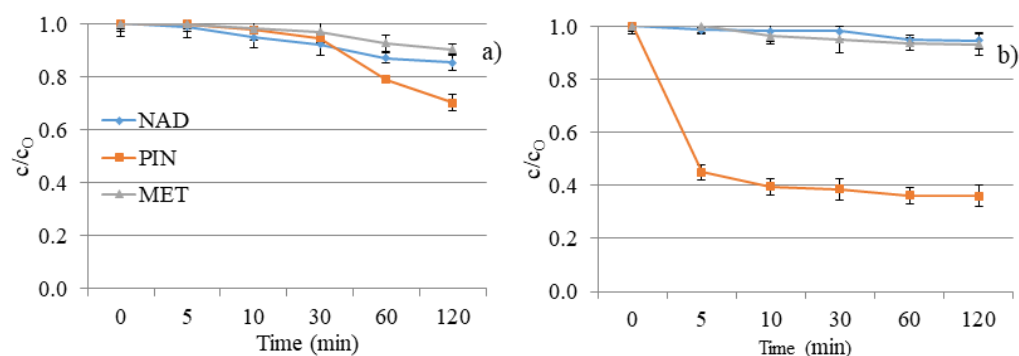

Figure 9. NAD, PIN, and MET degradation kinetics under UV irradiation: (**a**) without V_2O_5 and (**b**) with V_2O_5 catalyst.

The poor degradation efficiency of investigated compounds was expected, considering the investigated compounds' absorption maxima and the UV lamp's characteristics. Namely, the absorption maximum of the used lamp corresponds to the UV/A-B region of the spectrum. As shown in Figure 9a, MET and NAD expressed 10% and 15% degradation after 120 min. DF of separate solutions offers slight removal of NAD and MET and a two- to three-times higher degradation rate for PIN (30%). The nature of the substituents attached to the aromatic ring and the secondary interaction of released ions have significant roles in the degradation progress and regulate the degradation pathways. The obtained results can be explained based on the structural characteristics of the tested compounds.

The efficiency of DF is usually improved when irradiation is combined with a photocatalyst. However, V_2O_5 did not show a positive effect on the removal of NAD and MET from the aqueous solution (Figure 9b). Moreover, the efficiency of the process has decreased in comparison to DF. We can conclude that the turbidity of the solution resulting from the presence of nanomaterials decreased the removal efficiency of the mentioned two beta blockers. However, PIN showed higher efficiency than MET and NAD in the presence and absence of a V_2O_5 catalyst. Namely, 64% of PIN was eliminated by photocatalytic degradation within 120 min.

In addition to the fact that it is necessary to overlap at least partially the radiation spectrum and the compounds that DF decomposes, the pH of the solution plays a vital role in the creation of reactive oxygen species and the further interaction of released ions and radicals. The pH value of the aqueous solutions for DF was about 7.5 ± 1.0 (Figure 10). At the specified pH value of the aqueous solution, reactive oxygen species can be created in the water, contributing to the degradation efficiency.

In the presence of V_2O_5, the pH values of water suspensions were around 4.0 ± 0.5 (Figure 10). The effect of pH solution on photocatalytic degradation is complex due to the electrostatic interaction between the semiconductor surface, solvent molecules, substrate, and radicals formed during the photodegradation reaction.

V_2O_5 is a transition metal oxide of vanadium that has a narrow band gap (2.3 eV) [22,24]. It can capture a significant fraction of the UV spectrum to generate active redox centers. Photoactivation happens with wavelengths less than 443 nm [42]. Catalyst also accelerated the degradation of PIN two times compared to the DF study within 120 min (64% and 30%, respectively). However, the catalyst did not have expected behavior towards MET and NAD, wherein the degradation rate was almost the same for these two β-blockers (7% and 5%, respectively). Differences between the efficiency of PIN removal and removal of MET and NAD result from differences in these compounds' structural and electronic properties. With the addition of V_2O_5, the pH value of NAD and PIN solutions decreased from 8.0 to

around 3.5. There was no significant change in pH value for the MET solution after V_2O_5 addition, and the pH value was about 4.4 during 120 min of photocatalysis.
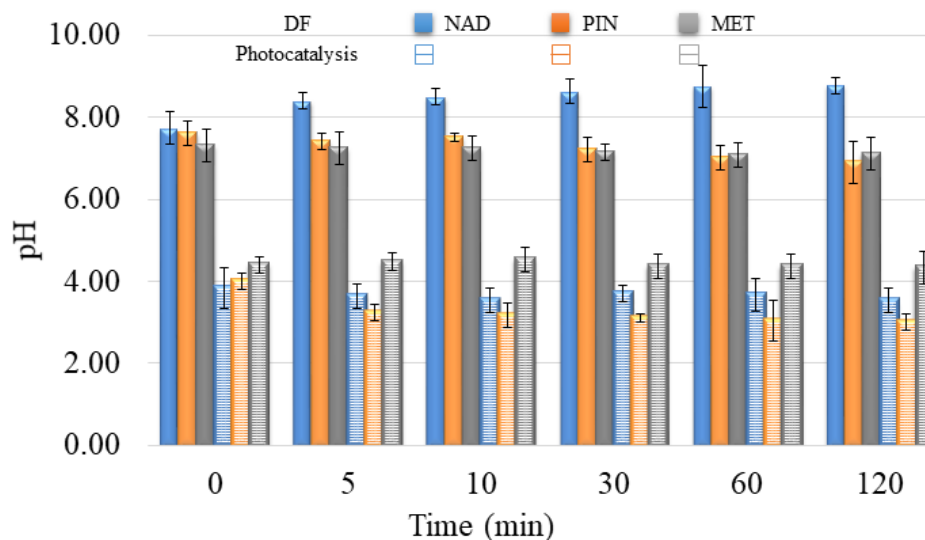

Figure 10. pH value during degradation of selected pharmaceuticals under UV irradiation without V_2O_5 (DF) and with V_2O_5 catalyst (Photocatalysis).

When the pH is ≥ 7 •OH radicals are the main reactive species, while at lower pH values, the reactive species are h^+ [43,44]. Based on pH value, it can be determined through which reactive species the process takes place in the presence of V_2O_5. Since the pH value is less than 7 for all three β-blockers, the reactive species are h^+. However, because the efficiency for MET and NAD is low in the presence of V_2O_5, it implies that degradation did not occur via h^+. In contrast, the degradation of PIN takes place via h^+. To better understand the interaction between MET and the •OH radicals, Armaković et al. [45] have conducted a DFT computational analysis. The interaction of •OH radicals with MET formed a new bond. It was concluded that •OH binds to the aromatic ring of MET. Moreover, the structural properties of MET indicated the highest interaction of MET and •OH, compared to other radicals and h^+. These data are essential, considering that MET and NAD are similar β-blockers, concluding that NAD will also interact with •OH radicals. Data obtained in this work also supported similar behavior of MET and NAD in reaction with V_2O_5. Armaković et al. [46] have determined the Fukui f_0 function of the PIN molecule, which provides information about the sensitivity towards radical attacks. Since positive values of Fukui f_0 were mainly located at the PIN rings, they suggested that this molecular site is the most sensitive to radical attacks. However, they emphasized that the h^+ generated during the photocatalytic process significantly increases degradation efficiency. Jovanoski Kostić et al. [47] have stated that the influence of h^+ on the photodegradation of PIN is favored in acidic conditions. The obtained pH value (Figure 10) within the photodegradation of PIN using V_2O_5 indicated that the mechanism of degradation of PIN occurs mainly via h^+.

To explain the observed difference in degradation efficiencies, we performed a computational analysis of all molecules in the framework of the DFT approach. Since the degradation efficiency generally depends on the reactivity of molecules and photophysical properties of the catalyst, we decided to compare the reactivity of considered molecules by calculating the average local ionization energy (ALIE), a well-known quantum molecular descriptor. The analysis of the ALIE quantum-molecular descriptor precisely identifies the PIN molecule as the most reactive of all three considered, see Figure 11.
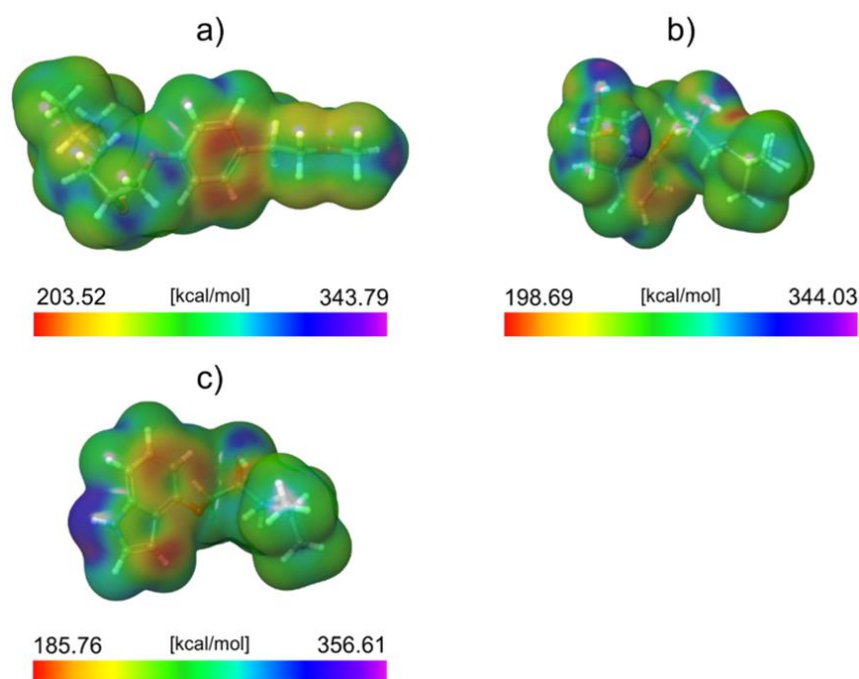
Figure 11. ALIE surfaces of (**a**) MET, (**b**) NAD, and (**c**) PIN.

This work visualized the ALIE descriptor as an electron density surface mapped with the ALIE values. ALIE values indicate the energy required to remove an electron from a certain point around the molecule. The lower this energy is, the easier it is to remove an electron from a certain point around the molecule. The results presented in Figure 11 indicate that the PIN is by far the most reactive of all three considered molecules in terms of how easy it is to remove an electron from it. Both MET and NAD have relatively similar lowest values of the ALIE descriptor (the difference is ~4 kcal/mol). On the other side, the PIN has around 14 kcal/mol lower minimal ALIE value than NAD and about 19 kcal/mol lower minimal ALIE value than MET.

This significant difference in ALIE indicates that the PIN molecule is much more sensitive to the influence of positive charge than the other two molecules. This also suggests that the positively charged h^+ might be responsible for the efficient degradation of the PIN. Since, according to the ALIE descriptor, the other two molecules are not sensitive to positive charge as the PIN is, their degradation efficiency is very low. The distribution of ALIE values on the electron density surface leads to one more important conclusion regarding the PIN's degradation efficiency. Namely, the lowest ALIE values are delocalized to a much greater extent over the PIN molecule than the MET and NAD. This means that a much higher surface area of the PIN molecule is sensitive toward the positive charge compared to the MET and NAD.

Further, the mixture of NAD, PIN, and MET was subjected to DF and a photocatalytic reaction with V_2O_5 to study their degradation when coexisting in environmental waters, as it occurs in nature. As seen in Figure 12a, exposure of the NAD, PIN, and MET mixture to UV did not cause a higher degradation efficiency of these three compounds. The DF of the separate solution of each β-blocker was a more efficient process. The reason may be caused by the additive or synergistic effects of the structures of these three β-blockers and the same amount of UV energy distributed over all three compounds [11]. Moreover, the pH value during decomposition (Figure 13) was constant and slightly basic (around 7.7 ± 0.2), indicating no changes in the aqueous solution.
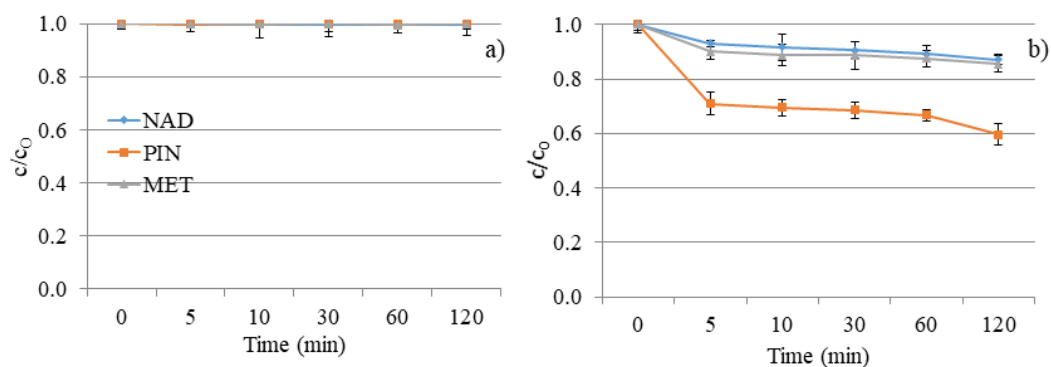
Figure 12. NAD, PIN, and MET mixture degradation kinetics under UV irradiation: (**a**) without V_2O_5 and (**b**) with V_2O_5 catalyst.
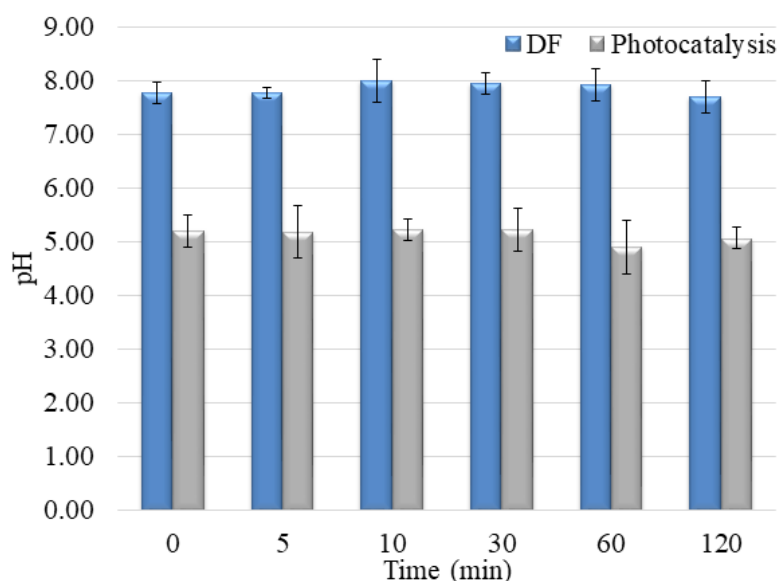

Figure 13. pH values during NAD, PIN, and MET mixture degradation under UV irradiation without/with V_2O_5 catalyst.

The lower photocatalytic efficiency of the PIN removal was achieved in a mixture with NAD and MET than in an individual solution. However, a much more interesting result is the increase in the degradation rate of NAD and MET in the presence of PIN (Figures 9b and 12b). One of the possible reasons for the acceleration of the decomposition process of NAD and MET in the mixture with PIN could be the higher concentration of NAD and MET molecules on the surface of the catalyst, which is also an explanation for the lower decomposition efficiency of PIN. Namely, 5 min after the beginning of UV irradiation, a certain amount of each compound was removed, and it continued to slightly increase up to a degradation rate of 13% for NAD, 40% for PIN, and 15% for MET within 120 min.

The mixture solution's pH was also acidic, but a 1.0 value higher than in the separate pharmaceuticals solutions (around 5.0 ± 0.2). These results also indicate that the presence of all three compounds in water changes starting pH. Moreover, the changing pH during degradation is different, showing the other degradation mechanism and the generation of various intermediates during the degradation process (Figures 10 and 13).

3. Materials and Methods

3.1. Chemicals and Solutions

The active components of β-blockers, NAD ($\geq$99%, Sigma-Aldrich, Hamburg, Germany), PIN ($\geq$99%, Sigma-Aldrich, Hamburg, Germany), and MET ($\geq$99%, Sigma-Aldrich,

Hamburg, Germany) were used as received. All three solutions were made using ultrapure water (UPW, κ = 0.055 μS/cm, pH 6.6).

As the catalyst, V_2O_5 was used at a concentration of 1.0 mg/cm^3. Detailed information about the V_2O_5 synthesis is given in Sections 3.2 and 3.3.

Ammonium metavanadate (NH_4VO_3, ACS reagent, ≥99.0%, Sigma-Aldrich, Hamburg, Germany), acetic acid (glacial) 100% (CH_3CO_2H) anhydrous for analysis (EMSURE ACS, ISO, Reag. Ph Eur, Supelco, Bellefonte, PA, USA), ethanol absolute (CH_3CH_2OH, ACS reagent absolute, Supelco) were used as received.

3.2. Powder Synthesis

The facile hydrothermal synthesis method was used to prepare V_2O_5 powders [14,48]. For that purpose, 0.1 M ammonium metavanadate (NH_4VO_3) was dissolved in 80 mL of distilled water, resulting in a pale yellow solution. To adjust the pH of the reaction solution to about 4, the diluted acetic acid (CH_3COOH/H_2O = 1:1 *v/v*) was added drop-wise. The final orange solution was placed into a Teflon-lined stainless steel autoclave and kept at 180 °C for 24 h and then naturally cooled down to room temperature. The orange product was centrifuged with distilled water and absolute ethanol and dried at 80 °C for 12 h. The as-prepared sample was annealed at 500 °C for 2 h in air.

3.3. Characterization

The catalyst was investigated by X-ray powder diffraction (XRPD). Measurements were conducted on a Rigaku Smartlab X-ray diffractometer in θ-θ geometry (the sample in horizontal position) in part focusing on Bragg–Brentano geometry using a D/teX Ultra 250 strip detector in 1D standard mode with a CuK$\alpha_{1,2}$ radiation source (U = 40 kV and I = 30 mA). The XRPD patterns were collected in the 4–90° 2θ range, with a step of 0.01°, and a data collection speed of 5.1 °/min. The low background single crystal silicon sample holder minimizes the background. Unit cell parameters and average crystallite size and lattice strain values were obtained by PDXL2 integrated X-ray powder diffraction software (Version 2.8.30; Rigaku Corporation, Tokyo, Japan).

The morphology and composition/quality of the catalyst were analyzed on SEM (JEOL JSM–6460LV, with the operating voltage of 20 keV) equipped with an EDS INCAx-sight detector and an "INAx-stream" pulse processor (Oxford Instruments, Abingdon, UK).

The Raman scattering spectra of the catalyst were taken in the backscattering geometry at room temperature in the air using Jobin-Yvon T64000 triple spectrometer (with 1800 grooves mm^{-1} grating) equipped with a confocal microscope and a nitrogen–cooled charge-coupled device detector. The spectra were excited by a 514.5 nm line of Ar^+/Kr^+ ion laser with an output power of less than 10 mW.

The UV–vis diffuse reflectance (UV–vis DR) spectrum was recorded in the wavelength range of 200−1400 nm using the Shimadzu UV-2600 spectrophotometer equipped with an integrated sphere. The reflectance spectra were measured relative to a reference sample of $BaSO_4$.

3.4. Photodegradation Experiments

Photocatalytic degradation experiments were conducted through NAD, PIN, and MET solutions (0.05 mmol/dm^3) exposed to UV irradiation in the presence of catalyst V_2O_5 (1.0 mg/cm^3). In the case of the DF study, solutions were exposed to UV irradiation without a catalyst. Each solution, separately (in the volume of 20 cm^3), and then a mixture of all three β-blockers, was placed in a cell made of Pyrex glass (total volume ca. 40 cm^3, liquid layer thickness 35 mm) with a water circulating jacket. The cell was then placed in an ultrasonic bath, and suspensions were sonicated for 15 min. Afterward, a magnetic stir was added to the cell and placed on a magnetic stirrer in the stream of O_2, thermostated at 25 ± 0.5 °C. The cell has a plain window on which the UV light beam was focused. The UV radiation source was a 125 W high-pressure mercury lamp (emission bands at 290,

293, 296, 304, 314, 335, and 366 nm, with maximum emission at 366 nm and intensity of 2.6×10^{-3} W/cm^2 in the visible region and 1.4×10^{-2} W/cm^2 in the UV region).

In order to investigate the adsorption of selected β-blockers on the surface of the material, a solution of the corresponding compound was analyzed in the presence of V_2O_5 under identical conditions as photocatalytic degradation but without irradiation of the solution. The results showed negligible adsorption (less than 1% in 120 min in all three cases).

3.5. Analytical Procedure

For each solution (NAD, PIN, and MET) the sample was collected before cell exposure to the UV irradiation, filtered through a Millipore membrane filter (Milex-GV, 0.22 μm), and placed in a chromatographic vial. Then, the samples were collected and filtered after 5, 10, 30, 60, and 120 min from the beginning of exposure to the UV irradiation. At each sample point, the pH value was measured.

In order to study the degradation kinetics, 20 μL of the filtrate was analyzed by Shimadzu UFLC-PDA (Shimadzu Scientific Instruments, Columbia, Maryland, USA) Eclipse XDB-C18 column, 1550 mm × 4.6 mm i.d., particle size 5 μm, 30 °C). The UV/Vis PDA detector was set at wavelengths of maximum absorption of each β-blocker: 210 nm (for NAD), 217 nm (for PIN), and 223 nm (for MET). To achieve better peak separation, gradient elution was used (flow rate 0.7 mL min^{-1}, ACN, and water mixture—15% ACN at the beginning increased to 25% ACN at 6 min, and after that, it was constant for the next 2 min; post time 1 min).

3.6. Computational Details

All molecular DFT calculations were performed using the B3LYP density functional [49–52] in combination with a 6-31G(d,p) basis set [53–55]. All molecules were subjected to frequency calculations to check that geometrical optimizations identified the true ground states. Frequency calculations yielded only positive values. During geometrical optimizations, frequency, and property calculations, solvent effects (water) were considered in the Poisson–Boltzmann solver framework. Molecular DFT calculations were performed with the Jaguar program [56–59], as implemented in the Schrödinger Materials Science Suite 2022-2. TD-DFT analyses were performed using the long-range corrected version of B3LYP, namely the CAM-B3LYP density functional [60], together with the 6-311++G(d,p) basis set [61,62]. TD-DFT calculations were performed with ORCA 5.0.3. molecular modeling package developed by Prof. Frank Neese and coworkers [63–70]. Input files for TD-DFT analyses were prepared with the online ORCA input generator of the atomistica.online web application [71], available at https://atomistica.online.

All periodic DFT calculations were performed using the PBE density functional [72], including the empirically derived correction (D3 variant) developed by Prof. Stefan Grimme and coworkers [73–77]. Additionally, we included the Hubbard U correction for vanadium atoms to consider the underestimation of the band gap by the DFT approach [78]. In this case, we set the U value for vanadium to be 3.5 eV [39]. All periodic DFT calculations were performed with the Quantum Espresso program [79–82], as implemented in the Schrödinger Materials Science Suite 2022-2.

4. Conclusions

For the preparation of V_2O_5, facile hydrothermal synthesis was used. X-ray diffraction identifies only one crystalline phase in the sample, which is proven by the fact that the crystallite size (1251(35) Å) and lattice strain (0.16(2)%) values point to well-crystallized material with a significant lattice strain. SEM micrographs show that hexagonal-shaped platelets with well-defined morphology were obtained as substantial entities with diameters in the range of 10–65 μm and thicknesses of around a few microns, following previously conducted similar procedures available in the literature. EDS spectra indicate that the main elements of the catalyst are vanadium and oxygen with no other impurities, and the

estimated contribution of each component is close to stoichiometric V_2O_5. The Raman scattering measurements taken on the catalyst confirmed the result of XRPD.

The efficiency of DF of the individual solutions was poor, except for PIN (10% for MET, 15% for NAD, and 30% for PIN). Adding a catalyst in the water solution of MET and NAD did not improve the degradation. However, the degradation efficiency of PIN increased up to 64% within 120 min. This study considered various perspectives to determine why PIN showed the highest efficiency. The fact that PIN absorbs light at a wavelength of around 200 nm and has relatively strong light absorption at 260 nm may indicate its superior degradation efficiency over the other two molecules. Calculations of ALIE indicate that the PIN is by far the most reactive of all three considered molecules in terms of how easy it is to remove an electron from it. MET and NAD have similar minimal ALIE values, and PIN has around 14 kcal/mol lower minimal ALIE value than NAD and about 19 kcal/mol more down minimal ALIE value than MET. Moreover, the pH value indicated different intermediates of photocatalysis. Namely, following the fact that PIN degradation was at a pH value below 4, it can be concluded that PIN degradation occurs via h^+.

A photocatalytic study of a mixture of NAD, MET, and PIN, as they occur in nature, shows that the degradation processes for MET and NAD were accelerated compared to individual solutions of these two compounds. This can be explained by a higher concentration of NAD and MET molecules on the surface of the catalyst, which also explains the lower decomposition efficiency of PIN. Conditions in the mixture were acidic, with a pH value higher than in individual solutions. pH values were changing differently, indicating the other degradation mechanism and generation of various intermediates during the degradation process.

This and other research demonstrated that V_2O_5 has a significant potential for practical applications to eliminate organic pollutants from the most precious natural resource—water. However, an extensive literature survey performed for this research has indicated several more essential facts regarding the potential of V_2O_5 for practical applications. One of the most important facts concerns bandgap engineering in the case of the V_2O_5. Namely, it was demonstrated that the bandgap value can be efficiently tuned, either by manipulating the structure of V_2O_5 or by applying an external stimulus. It has been reported that the band gap of V_2O_5 can either be decreased or increased, depending on the selected technique. The ability to finely tune the band gap of V_2O_5 is essential for its practical application as a photocatalyst. Finally, the readily available synthesis of this material is one more factor determining the bright future of the material.

Conflicts of Interest: The authors declare no conflict of interest.

Sample Availability: Samples of the compounds are not available from the authors.

References

1. Fallah, Z.; Zare, E.; Ghomi, M.; Ahmadijokani, F.; Amini, M.; Tajbakhsh, M.; Arjmand, M.; Sharma, G.; Ali, H.; Ahmad, A. Toxicity and remediation of pharmaceuticals and pesticides using metal oxides and carbon nanomaterials. *Chemosphere* **2021**, *275*, 130055. [CrossRef]
2. Ali, I.; Alothman, Z.; Alwarthan, A. Uptake of propranolol on ionic liquid iron nanocomposite adsorbent: Kinetic, thermodynamics and mechanism of adsorption. *J. Mol. Liq.* **2017**, *236*, 205–213. [CrossRef]
3. Kibbey, T.; Paruchuri, R.; Sabatini, D.; Chen, L. Adsorption of beta blockers to environmental surfaces. *Environ. Sci. Technol.* **2007**, *41*, 5349–5356. [CrossRef] [PubMed]
4. Alder, A.; Schaffner, C.; Majewsky, M.; Klasmeier, J.; Fenner, K. Fate of β-blocker human pharmaceuticals in surface water: Comparison of measured and simulated concentrations in the Glatt Valley Watershed, Switzerland. *Water Res.* **2010**, *44*, 936–948. [CrossRef]
5. Kim, K.; Cho, E.; Choi, J.; Kim, H.; Jang, A.; Choi, Y.; Yu, J.-H.; Jung, S. Intermolecular complexation of low-molecular-weight succinoglycans directs solubility enhancement of pindolol. *Carbohydr. Polym.* **2014**, *106*, 101–108. [CrossRef]
6. Perlovich, G.; Volkova, T.; Bauer-Brandl, A. Thermodynamic study of sublimation, solubility, solvation, and distribution processes of atenolol and pindolol. *Mol. Pharm.* **2007**, *4*, 929–935. [CrossRef] [PubMed]
7. Hernando, M.; Gómez, M.; Agüera, A.; Fernández-Alba, A. LC-MS analysis of basic pharmaceuticals (beta-blockers and anti-ulcer agents) in wastewater and surface water. *TrAC Trends Anal. Chem.* **2007**, *26*, 581–594. [CrossRef]
8. Dhangar, K.; Kumar, M. Tricks and tracks in removal of emerging contaminants from the wastewater through hybrid treatment systems: A review. *Sci. Total Environ.* **2020**, *738*, 140320. [CrossRef] [PubMed]
9. Bijlsma, L.; Pitarch, E.; Fonseca, E.; Ibanez, M.; Botero, A.; Claros, J.; Pastor, L.; Hernandez, F. Investigation of pharmaceuticals in a conventional wastewater treatment plant: Removal efficiency, seasonal variation and impact of a nearby hospital. *J. Environ. Chem. Eng.* **2021**, *9*, 105548. [CrossRef]
10. Ye, Y.; Feng, Y.; Bruning, H.; Yntema, D.; Rijnaarts, H. Photocatalytic degradation of metoprolol by TiO_2 nanotube arrays and UV-LED: Effects of catalyst properties, operational parameters, commonly present water constituents, and photo-induced reactive species. *Appl. Catal. B Environ.* **2018**, *220*, 171–181. [CrossRef]
11. Stankiewicz, A.; Giebułtowicz, J.; Stankiewicz, U.; Wroczyński, P.; Nałęcz-Jawecki, G. Determination of selected cardiovascular active compounds in environmental aquatic samples–methods and results, a review of global publications from the last 10 years. *Chemosphere* **2015**, *138*, 642–656. [CrossRef] [PubMed]
12. Radjenović, J.; Petrović, M.; Barceló, D. Fate and distribution of pharmaceuticals in wastewater and sewage sludge of the conventional activated sludge (CAS) and advanced membrane bioreactor (MBR) treatment. *Water Res.* **2009**, *43*, 831–841. [CrossRef]
13. Liu, H.; Chen, M.; Wei, D.; Ma, Y.; Wang, F.; Zhang, Q.; Shi, J.; Zhang, H.; Peng, J.; Liu, G. Smart removal of dye pollutants via dark adsorption and light desorption at recyclable $Bi_2O_2CO_3$ nanosheets interface. *ACS Appl. Mater. Interfaces.* **2020**, *12*, 20490–20499. [CrossRef] [PubMed]
14. Kumar, O.; Shahzad, K.; Nazir, M.; Farooq, N.; Malik, M.; Shah, S.; ur Rehman, A. Photo-Fenton activated $C_3N_{4x}/AgO_y@Co_{1-x}Bi_{0.1-y}O_7$ dual s-scheme heterojunction towards degradation of organic pollutants. *Opt. Mater.* **2022**, *126*, 112199. [CrossRef]
15. Jamshaid, M.; Nazir, M.; Najam, T.; Shah, S.; Khan, H.; ur Rehman, A. Facile synthesis of Yb^{3+}-Zn^{2+} substituted M type hexaferrites: Structural, electric and photocatalytic properties under visible light for methylene blue removal. *Chem. Phys. Lett.* **2022**, *805*, 139939. [CrossRef]
16. Oluwole, A.O.; Omotola, E.O.; Olatunji, O.S. Pharmaceuticals and personal care products in water and wastewater: A review of treatment processes and use of photocatalyst immobilized on functionalized carbon in AOP degradation. *BMC Chem.* **2020**, *14*, 62. [CrossRef]
17. Soares, S.F.; Simoes, T.; Antonio, M.; Trindade, T.; Daniel-da-Silva, A.L. Hybrid nanoadsorbents for the magnetically assisted removal of metoprolol from water. *Chem. Eng. J.* **2016**, *302*, 560–569. [CrossRef]
18. Shahzad, K.; Khan, M.I.; Shanableh, A.; Elboughdiri, N.; Jabeen, M.A.; Nazir, M.; Farooq, N.; Ali, H.; Abdelfattah, A.U.; ur Rehman, A. Silver supported-Ag@ PMOS onto thumb structured porous organosilica materials with efficient hetero-junction active sites for photo-degradation of methyl orange dye. *Inorg. Nano-Met. Chem.* **2022**, *52*, 407–416.
19. Suresh, R.; Giribabu, K.; Manigandan, R.; Munusamy, S.; Kumar, S.; Muthamizh, S.; Stephen, A.; Narayanan, V. Doping of Co into V_2O_5 nanoparticles enhances photodegradation of methylene blue. *J. Alloys Compd.* **2014**, *598*, 151–160. [CrossRef]
20. Jayaraj, S.; Sadishkumar, V.; Arun, T.; Thangadurai, P. Enhanced photocatalytic activity of V_2O_5 nanorods for the photodegradation of organic dyes: A detailed understanding of the mechanism and their antibacterial activity. *Mater. Sci. Semicond. Process.* **2018**, *85*, 122–133. [CrossRef]

21. Sajid, M.; Shad, N.; Javed, Y.; Khan, S.; Zhang, Z.; Amin, N.; Zhai, H. Preparation and characterization of Vanadium pentoxide (V$_2$O$_5$) for photocatalytic degradation of monoazo and diazo dyes. *Surf. Interfaces* **2020**, *19*, 100502. [CrossRef]

22. Sun, J.; Li, X.; Zhao, Q.; Ke, J.; Zhang, D. Novel V2O5/BiVO4/TiO2 nanocomposites with high visible-light-induced photocatalytic activity for the degradation of toluene. *J. Phys. Chem. C* **2014**, *118*, 10113–10121. [CrossRef]

23. Fu, X.; Tang, W.; Ji, L.; Chen, S. V$_2$O$_5$/Al$_2$O$_3$ composite photocatalyst: Preparation, characterization, and the role of Al$_2$O$_3$. *Chem. Eng. J.* **2012**, *180*, 170–177. [CrossRef]

24. Karthik, K.; Nikolova, M.; Phuruangrat, A.; Pushpa, S.; Revathi, V.; Subbulakshmi, M. Ultrasound-assisted synthesis of V$_2$O$_5$ nanoparticles for photocatalytic and antibacterial studies. *Mater. Res. Innov.* **2020**, *24*, 229–234. [CrossRef]

25. Aslam, M.; Ismail, I.; Salah, N.; Chandrasekaran, S.; Qamar, M.; Hameed, A. Evaluation of sunlight induced structural changes and their effect on the photocatalytic activity of V$_2$O$_5$ for the degradation of phenols. *J. Hazard. Mater.* **2015**, *286*, 127–135. [CrossRef]

26. Chan, Y.-L.; Pung, S.-Y. Sreekantan, Synthesis of V$_2$O$_5$ nanoflakes on PET fiber as visible-light-driven photocatalysts for degradation of RhB dye. *J. Catal.* **2014**, *2014*, 370696.

27. Saravanan, R.; Gupta, V.; Mosquera, E.; Gracia, F. Preparation and characterization of V$_2$O$_5$/ZnO nanocomposite system for photocatalytic application. *J. Mol. Liq.* **2014**, *198*, 409–412. [CrossRef]

28. Rasheed, R.; Mansoor, H.; Abdullah, T.; Juzsakova, T.; Al-Jammal, N.; Salman, A.D.; Al-Shaikhly, R.R.; Le, P.; Domokos, E.; Abdulla, T.A. Synthesis, characterization of V$_2$O$_5$ nanoparticles and determination of catalase mimetic activity by new colorimetric method. *J. Therm. Anal. Calorim.* **2021**, *145*, 297–307. [CrossRef]

29. Abdullah, T.; Juzsakova, T.; Rasheed, R.; Mallah, M.; Salman, A.; Cuong, L.; Jakab, M.; Zsirka, B.; Kułacz, K.; Sebestyén, V. V$_2$O$_5$, CeO$_2$ and Their MWCNTs Nanocomposites Modified for the Removal of Kerosene from Water. *Nanomaterials* **2022**, *12*, 189. [CrossRef] [PubMed]

30. Shvets, P.; Dikaya, O.; Maksimova, K.; Goikhman, A. A review of Raman spectroscopy of vanadium oxides. *J. Raman Spectrosc.* **2019**, *50*, 1226–1244. [CrossRef]

31. Ureña-Begara, F.; Crunteanu, A.; Raskin, J.-P. Raman and XPS characterization of vanadium oxide thin films with temperature. *Appl. Surf. Sci.* **2017**, *403*, 717–727. [CrossRef]

32. Ilahi, B.; Abdel-Rahman, M.; Zaaboub, Z.; Zia, M.; Alduraibi, M.; Maaref, H. Thermal annealing induced multiple phase in V/V$_2$O$_5$ alternating multilayer structure. *Int. J. Mod. Phys. B* **2016**, *30*, 1650210. [CrossRef]

33. Wang, Y.; Rosowski, F.; Schlögl, R.; Trunschke, A. Oxygen Exchange on Vanadium Pentoxide. *J. Phys. Chem. C* **2022**, *126*, 3443–3456. [CrossRef]

34. Kubelka, P. New contributions to the optics of intensely light-scattering materials. Part I. *Josa* **1948**, *38*, 448–457. [CrossRef] [PubMed]

35. Tauc, J. Optical properties and electronic structure of amorphous Ge and Si. *Mater. Res. Bull.* **1968**, *3*, 37–46. [CrossRef]

36. Makuła, P.; Pacia, M.; Macyk, W. How to correctly determine the band gap energy of modified semiconductor photocatalysts based on UV–Vis spectra. *J. Phys. Chem. Lett.* **2018**, *9*, 6814–6817. [CrossRef]

37. Schneider, K. Optical properties and electronic structure of V$_2$O$_5$, V$_2$O$_3$ and VO$_2$. *J. Mater. Sci. Mater. Electron.* **2020**, *31*, 10478–10488. [CrossRef]

38. Mousavi, M.; Yazdi, S.T.; Khorrami, G. Structural, Optical and Magnetic Characterization of Vanadium Pentoxide Nanoparticles Synthesized in a Gelatin Medium. *J. Nanostruct.* **2021**, *11*, 105–113.

39. Das, T.; Tosoni, S.; Pacchioni, G. Structural and electronic properties of bulk and ultrathin layers of V$_2$O$_5$ and MoO$_3$. *Comput. Mater. Sci.* **2019**, *163*, 230–240. [CrossRef]

40. Khyzhun, O.; Strunskus, T.; Grünert, W.; Wöll, C. Valence band electronic structure of V$_2$O$_5$ as determined by resonant soft X-ray emission spectroscopy. *J. Electron Spectrosc. Relat. Phenom.* **2005**, *149*, 45–50. [CrossRef]

41. Srilakshmi, P.; Maheswari, A.; Sajeev, V.; Sivakumar, M. Tuning the optical bandgap of V$_2$O$_5$ nanoparticles by doping transition metal ions. *Mater. Today Proc.* **2019**, *18*, 1375–1379. [CrossRef]

42. Karunakaran, C.; Senthilvelan, S. Vanadia-catalyzed solar photooxidation of aniline. *J. Colloid Interface Sci.* **2005**, *289*, 466–471. [CrossRef] [PubMed]

43. Konstantinou, I.; Albanis, T. TiO$_2$-assisted photocatalytic degradation of azo dyes in aqueous solution: Kinetic and mechanistic investigations: A review. *Appl. Catal. B Environ.* **2004**, *49*, 1–14. [CrossRef]

44. Faisal, M.; Tariq, M.; Muneer, M. Photocatalysed degradation of two selected dyes in UV-irradiated aqueous suspensions of titania. *Dyes Pigments* **2007**, *72*, 233–239. [CrossRef]

45. Armaković, S.; Armaković, S.; Finčur, N.; Šibul, F.; Vione, D.; Šetrajčić, J.; Abramović, B. Influence of electron acceptors on the kinetics of metoprolol photocatalytic degradation in TiO$_2$ suspension. A combined experimental and theoretical study. *RSC Adv.* **2015**, *5*, 54589–54604. [CrossRef]

46. Armaković, S.; Armaković, S.; Šibul, F.; Četojević-Simin, D.; Tubić, A.; Abramović, B. Kinetics, mechanism and toxicity of intermediates of solar light induced photocatalytic degradation of pindolol: Experimental and computational modeling approach. *J. Hazard. Mater.* **2020**, *393*, 122490. [CrossRef]

47. Kostić, A.J.; Kanas, N.; Rajić, V.; Sharma, A.; Bhattacharya, S.; Armaković, S.; Savanović, M.; Armaković, S. Evaluation of Photocatalytic Performance of Nano-Sized Sr$_{0.9}$La$_{0.1}$TiO$_3$ and Sr$_{0.25}$Ca$_{0.25}$Na$_{0.25}$Pr$_{0.25}$TiO$_3$ Ceramic Powders for Water Purification. *Nanomaterials* **2022**, *12*, 4193. [CrossRef]

48. Li, B.; Xu, Y.; Rong, G.; Jing, M.; Xie, Y. Vanadium pentoxide nanobelts and nanorolls: From controllable synthesis to investigation of their electrochemical properties and photocatalytic activities. *Nanotechnology* **2006**, *17*, 2560. [CrossRef]

49. Stephens, P.; Devlin, F.; Chabalowski, C.; Frisch, M. Ab Initio Calculation of Vibrational Absorption and Circular Dichroism Spectra Using Density Functional Force Fields. *J. Phys. Chem.* **1994**, *98*, 11623–11627. [CrossRef]

50. Vosko, S.H.; Wilk, L.; Nusair, M. Accurate spin-dependent electron liquid correlation energies for local spin density calculations: A critical analysis. *Can. J. Phys.* **1980**, *58*, 1200–1211. [CrossRef]

51. Becke, A. Density-functional thermochemistry. III. The role of exact exchange. *J. Chem. Phys.* **1993**, *98*, 5648–5652. [CrossRef]

52. Lee, C.; Yang, W.; Parr, R. Development of the Colle-Salvetti correlation-energy formula into a functional of the electron density. *Phys. Rev. B* **1988**, *37*, 785. [CrossRef] [PubMed]

53. Rassolov, V.; Pople, J.; Ratner, M.; Windus, T.L. 6-31G* basis set for atoms K through Zn. *J. Chem. Phys.* **1998**, *109*, 1223–1229. [CrossRef]

54. Rassolov, V.; Ratner, M.; Pople, J.; Redfern, P.; Curtiss, L. 6-31G* basis set for third-row atoms. *J. Comput. Chem.* **2001**, *22*, 976–984. [CrossRef]

55. Ditchfield, R.; Hehre, W.; Pople, J. Self-Consistent Molecular-Orbital Methods. IX. An Extended Gaussian-Type Basis for Molecular-Orbital Studies of Organic Molecules. *J. Chem. Phys.* **1971**, *54*, 724–728. [CrossRef]

56. Jacobson, L.; Bochevarov, A.; Watson, M.; Hughes, T.; Rinaldo, D.; Ehrlich, S.; Steinbrecher, T.; Vaitheeswaran, S.; Philipp, D.; Halls, M. Automated transition state search and its application to diverse types of organic reactions. *J. Chem. Theory Comput.* **2017**, *13*, 5780–5797. [CrossRef]

57. Cao, Y.; Hughes, T.; Giesen, D.; Halls, M.; Goldberg, A.; Vadicherla, T.; Sastry, M.; Patel, B.; Sherman, W.; Weisman, A.; et al. Highly efficient implementation of pseudospectral time-dependent density-functional theory for the calculation of excitation energies of large molecules. *J. Comput. Chem.* **2016**, *37*, 1425–1441. [CrossRef]

58. Bochevarov, A.; Harder, E.; Hughes, T.; Greenwood, J.; Braden, D.; Philipp, D.; Rinaldo, D.; Halls, M.; Zhang, J.; Friesner, R. Jaguar: A high-performance quantum chemistry software program with strengths in life and materials sciences. *Int. J. Quantum Chem.* **2013**, *113*, 2110–2142. [CrossRef]

59. Cao, Y.; Halls, M.; Vadicherla, T.; Friesner, R.A. Pseudospectral implementations of long-range corrected density functional theory. *J. Comput. Chem.* **2021**, *42*, 2089–2102. [CrossRef]

60. Yanai, T.; Tew, D.; Handy, N. A new hybrid exchange–correlation functional using the Coulomb-attenuating method (CAM-B3LYP). *Chem. Phys. Lett.* **2004**, *393*, 51–57. [CrossRef]

61. McLean, A.; Chandler, G. Contracted Gaussian basis sets for molecular calculations. I. Second row atoms, Z = 11–18. *J. Chem. Phys.* **1980**, *72*, 5639–5648. [CrossRef]

62. Krishnan, R.; Binkley, J.; Seeger, R.; Pople, J.A. Self-consistent molecular orbital methods. XX. A basis set for correlated wave functions. *J. Chem. Phys.* **1980**, *72*, 650–654. [CrossRef]

63. Liakos, D.; Guo, Y.; Neese, F. Comprehensive Benchmark Results for the Domain Based Local Pair Natural Orbital Coupled Cluster Method (DLPNO-CCSD(T)) for Closed- and Open-Shell Systems. *J. Phys. Chem. A* **2020**, *124*, 90–100. [CrossRef]

64. Neese, F.; Wennmohs, F.; Hansen, A.; Becker, U. Efficient, approximate and parallel Hartree–Fock and hybrid DFT calculations. A 'chain-of-spheres' algorithm for the Hartree–Fock exchange. *Mov. Front. Quantum Chem.* **2009**, *356*, 98–109. [CrossRef]

65. Guo, Y.; Riplinger, C.; Liakos, D.; Becker, U.; Saitow, M.; Neese, F. Linear scaling perturbative triples correction approximations for open-shell domain-based local pair natural orbital coupled cluster singles and doubles theory [DLPNO-CCSD(T0/T)]. *J. Chem. Phys.* **2020**, *152*, 024116. [CrossRef]

66. Neese, F. Software update: The ORCA program system—Version 5.0. *WIREs Comput. Mol. Sci.* **2022**, *12*, e1606. [CrossRef]

67. Neese, F. Software update: The ORCA program system, version 4.0. *WIREs Comput. Mol. Sci.* **2018**, *8*, e1327. [CrossRef]

68. Neese, F. The ORCA program system. *WIREs Comput. Mol. Sci.* **2012**, *2*, 73–78. [CrossRef]

69. Neese, F.; Wennmohs, F.; Becker, U.; Riplinger, C. The ORCA quantum chemistry program package. *J. Chem. Phys.* **2020**, *152*, 224108. [CrossRef] [PubMed]

70. Neese, F. The SHARK integral generation and digestion system. *J. Comput. Chem.* **2022**, *44*, 381–396. [CrossRef]

71. Armaković, S.; Armaković, S. Atomistica.online—Web application for generating input files for ORCA molecular modelling package made with the Anvil platform. *Mol. Simul.* **2023**, *49*, 117–123. [CrossRef]

72. Perdew, J.; Burke, K.; Ernzerhof, M. Generalized Gradient Approximation Made Simple. *Phys. Rev. Lett.* **1996**, *77*, 3865–3868; Erratum in *Phys. Rev. Lett.* **1997**, *78*, 1396. [CrossRef]

73. Grimme, S.; Antony, J.; Ehrlich, S.; Krieg, H. A consistent and accurate ab initio parametrization of density functional dispersion correction (DFT-D) for the 94 elements H-Pu. *J. Chem. Phys.* **2010**, *132*, 154104. [CrossRef] [PubMed]

74. Caldeweyher, E.; Ehlert, S.; Hansen, A.; Neugebauer, H.; Spicher, S.; Bannwarth, C.; Grimme, S. A generally applicable atomic-charge dependent London dispersion correction. *J. Chem. Phys.* **2019**, *150*, 154122. [CrossRef] [PubMed]

75. Grimme, S.; Ehrlich, S.; Goerigk, L. Effect of the damping function in dispersion corrected density functional theory. *J. Comput. Chem.* **2011**, *32*, 1456–1465. [CrossRef] [PubMed]

76. Caldeweyher, E.; Bannwarth, C.; Grimme, S. Extension of the D3 dispersion coefficient model. *J. Chem. Phys.* **2017**, *147*, 034112. [CrossRef]

77. Smith, D.; Burns, L.; Patkowski, K.; Sherrill, C.D. Revised Damping Parameters for the D3 Dispersion Correction to Density Functional Theory. *J. Phys. Chem. Lett.* **2016**, *7*, 2197–2203. [CrossRef] [PubMed]

78. Anisimov, V.; Zaanen, J.; Andersen, O.K. Band theory and Mott insulators: Hubbard U instead of Stoner I. *Phys. Rev. B* **1991**, *44*, 943–954. [CrossRef] [PubMed]

79. Giannozzi, P.; Andreussi, O.; Brumme, T.; Bunau, O.; Nardelli, M.B.; Calandra, M.; Car, R.; Cavazzoni, C.; Ceresoli, D.; Cococcioni, M.; et al. Advanced capabilities for materials modelling with Quantum ESPRESSO. *J. Phys. Condens. Matter.* **2017**, *29*, 465901. [CrossRef] [PubMed]

80. Scandolo, S.; Giannozzi, P.; Cavazzoni, C.; de Gironcoli, S.; Pasquarello, A. Baroni, First-principles codes for computational crystallography in the Quantum-ESPRESSO package. *Z. Krist. Cryst. Mater.* **2005**, *220*, 574–579. [CrossRef]

81. Giannozzi, P.; Baseggio, O.; Bonfà, P.; Brunato, D.; Car, R.; Carnimeo, I.; Cavazzoni, C.; de Gironcoli, S.; Delugas, P.; Ruffino, F.F.; et al. Quantum ESPRESSO toward the exascale. *J. Chem. Phys.* **2020**, *152*, 154105. [CrossRef] [PubMed]

82. Giannozzi, P.; Baroni, S.; Bonini, N.; Calandra, M.; Car, R.; Cavazzoni, C.; Ceresoli, D.; Chiarotti, G.L.; Cococcioni, M.; Dabo, I.; et al. QUANTUM ESPRESSO: A modular and open-source software project for quantum simulations of materials. *J. Phys. Condens. Matter.* **2009**, *21*, 395502. [CrossRef] [PubMed]

ORIGINAL PAPER

Atmospheric Plasma Supported by TiO$_2$ Catalyst for Decolourisation of Reactive Orange 16 Dye in Water

Tatjana Mitrović[1] · Nataša Tomić[2] · Aleksandra Djukić-Vuković[3] · Zorana Dohčević-Mitrović[4] · Saša Lazović[2]

Abstract

Purpose Every advanced oxidation process (AOP) has its limitations in water purification. Novel designs with simultaneous application of different AOPs can offer better solutions for cleaner water.

Methods We have comparatively studied two advanced oxidation processes (AOPs) on decolourisation of Reactive Orange 16 (RO 16) azo dye pollutant from water: gas plasma treatment by low power atmospheric pressure plasma using novel plasma needle configuration, and semiconductor heterogeneous photocatalysis using titanium dioxide (TiO$_2$) nanopowders. Additionally, simultaneous application of two advanced oxidation processes on azo dye decolourisation was studied.

Results It was found that plasma treatment is very efficient system for the dye removal even for low flow rates (1 slm) of the Ar as feed gas. The presence of 10% of O$_2$ in Ar flow intensified dye oxidation process and shortened required time for total decolourisation. When plasma and catalyst were simultaneously applied, TiO$_2$ was activated with a few Watts plasma source as well as 300 W UV lamp source. The synergic effect of two AOPs was more pronounced for higher feed gas flow rates, resulting in improved decolourisation efficiency.

Conclusion Plasma needle can efficiently remove Reactive Orange 16 azo dye from water with a power consumption of only few Watts. With the addition of TiO$_2$ the removal efficiency is significantly improved.

Graphic Abstract
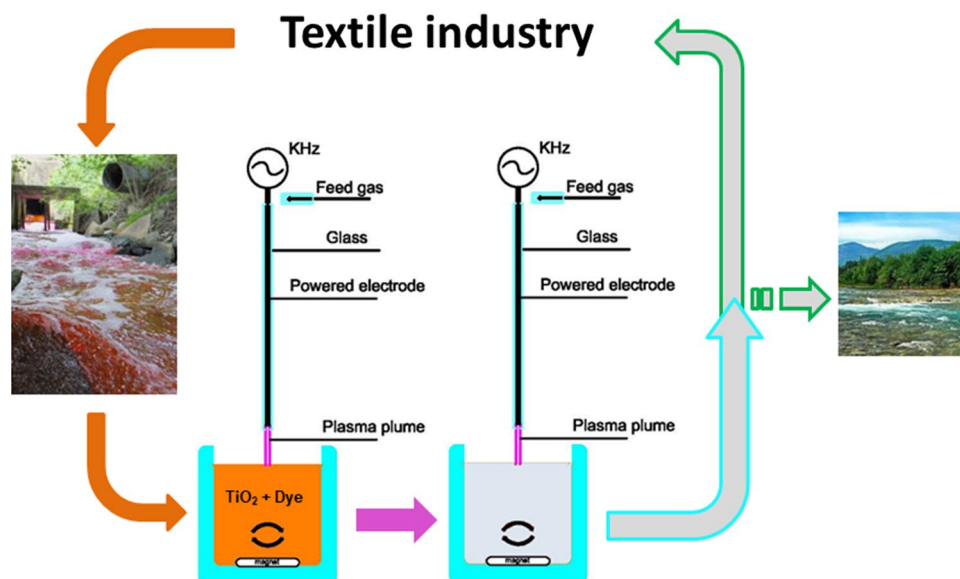
Extended author information available on the last page of the article

Statement of Novelty

Textile industry consumes around 2000 L of water to produce a single pair of jeans. Ten to fifteen percent of the global production of dyes is discharged into the waterbodies. This is not sustainable. Treated wastewater has to be reused. We propose a novel and efficient method for treatment of textile industry wastewater. A combination of two advanced oxidation processes—low power atmospheric pressure plasma and TiO_2 heterogeneous photocatalysis is used for decolourisation of Reactive Orange 16 azo dye pollutant.

Introduction

Since water is one of the most important resources, its availability and quality have become one of the biggest social priorities today. Increasing pollution of the water system, including textile industries and agriculture, affects ecosystem and human health directly and represent the widespread concern.

Textile and paper industries generate complex and diverse effluents and they belong to the most polluting industrial sectors [1]. Organic dyes as the main components of these effluents, are considered to be very toxic, mutagenic, and potentially carcinogenic [2, 3]. About 10–15% of the total world production of dyes are discharged into different waterbodies affecting directly aquatic life by disrupting the amount of dissolved O_2 and consequently photosynthesis and respiration processes [4-6].

Azo dyes are organic molecules generally with an azo bond (R–N $=$ N–R') as main chromophore group. They are widely used in textile industry and because of their chemical complexity and low biodegradability; the wastewater treatment is very demanding. Different methods are applied to remove these organic compounds from the water sources: biological, physicochemical (adsorption, coagulation/flocculation, reverse osmosis) or chemical treatments (chlorination and ozonation). However, these methods have certain limitations. The biological treatments are not effective in the case of stable and resistant azo dyes. Only few unstable azo dyes can be degraded under aerobic conditions. On the other hand, anaerobic degradation causes aromatic amines generation which are toxic and carcinogenic [7]. The physicochemical treatments often cause formation of secondary pollution, generating large amounts of sludge and transferring pollutants from water to solid phase. Therefore, incomplete degradation and necessity for additional operations including final degradation of

the waste and adsorbent regeneration limit the application of these treatments [8]. Chemical treatments like chlorination can result in complete decolourisation of dyes, but chlorinated organic by-products are very hazardous [9]. Ozone oxidizes dyes as well, but its extreme oxidizing effects can harm the atmosphere. Thus, ozonation system must include a control unit which prevents excessive use of chemicals [10].

Advanced oxidation processes (AOPs) have shown some advantages over the conventional water purification technologies. Based on the production of very strong and unselective oxidizing species (hydroxyl radicals—OH), these techniques are used in mineralization of soluble complex organic pollutants. The ultimate goal of this process is to decompose pollutants to CO_2, H_2O, and some inorganic ions. Most common AOPs are: gas plasma oxidation [11, 12], (heterogeneous) photocatalytic oxidation [13, 14], ultrasounds [15], photo Fenton oxidation [16, 17], etc.

Among above-mentioned treatments, gas plasma is a relatively novel AOP method for wastewater decontamination. The method is based on ionized gas produced by an electrical discharge, generating electrons, radicals (OH, H, O), ions (OH−, H_2O+, H+, HO_2⁻) and neutrals (H_2O_2, O_3). Plasma systems can be generally divided into thermal or non–thermal plasma. Thermal plasma typically needs more power than non–thermal and creates high flux of heat, which can be used for degradation of very resistant organic molecules. In the case of non–thermal plasma, electrons are at temperatures as high as 11,000 K, and are colliding with gas molecules at temperatures as low as the room temperature, promoting the generation of chemically active species [18].

Previous studies reported that non-thermal plasma generated in the gas phase above the water surface initiates many chemical and physical effects including a high electric field, intense ultraviolet radiation, overpressure shock waves and, of particular importance, formation of various chemically strong oxidative species like radicals and molecules (OH, H, O_2⁻, O, H_2O_2, O_3). These species, dissolved in water, initiate oxidation processes [19, 20].

Until now, various types of non–thermal plasma devices such as plasma jets [21, 22], plasma needle [23-25], gliding arc [26, 27], dielectric barrier discharge [28, 29], pulsed corona discharges [30, 31] have been developed. These systems have strong oxidizing ability and include simple feed conditions such as temperature and atmospheric pressure. During the treatment, various complex chemical reactions (collision, addition, dissociation and transformation reactions) can be initiated in the polluted solution [26]. Among above mentioned types of non-thermal plasma devices, plasma needle may be easily operated under atmospheric pressure and room temperature and do not require expensive vacuum systems. Its simple configuration provides very easy to work and it can be applied to a

wide range of vessels for treatment. Plasma needle is non-aggressive oxidation method which produces chemically active species at low gas temperature, thus meets all the necessary conditions for the treatment of organic materials, living tissues (wound sterilization, cancer treatment and other biomedical applications) and delicate materials which are unable to withstand vacuum or are thermally sensitive (heat- sensitive polymers, foodstuffs).

Liquid and gas plasma chemistry have been largely studied during the last decade and it is concluded that the degradation takes place mainly because of the formation of reactive radicals. The amount of radicals and their oxidation mechanisms depend on the discharge type and properties, such as the feed gas composition and flow rate, but also on the properties of the liquid [32]. Since the efficiency of non–thermal plasma treatment is highly dependent on the characteristics of both contaminant and liquid media, it is necessary to study and develop adequate treatment scheme for every pollutant/wastewater system.

Another most explored AOP is heterogeneous photocatalysis, because it is suitable for the destruction of resistant hazardous contaminants, as it uses inexpensive operational parameters such as light and semiconductors [33, 34]. It is based on the application of semiconductors and their capability to generate electron–hole pairs under light irradiation, which participate in different redox reactions on the catalyst surface leading to mineralization of the pollutant.

Nowadays, one of the most promising treatments for wastewater remediation combines plasma treatment with metal oxide catalysts [35]. The most common catalysts reported in literature are: TiO_2 [8, 36-38], ZnO [39], Fe_2O_3 [40], NiO [41], and Al_2O_3 [42]. It is expected that combined plasma—catalyst treatment can overcome drawbacks of individual plasma treatment and photocatalysis, preventing at the same time the electron–hole recombination at metal oxide surface and enhancing the mass transport of the reactants to the solid surface [18].

In this paper, we have investigated the decolourisation of toxic RO 16 azo dye through different treatments: low power atmospheric pressure gas plasma (plasma needle configuration); heterogeneous photocatalysis using TiO_2 as catalyst; and combined plasma–catalysis application. To the best of our knowledge, the joint application of plasma needle and catalyst employed for decolourisation of organic dye has not been studied yet. We have developed plasma needle setup to study the effects of flow rate, feed gas composition (Ar and Ar/O_2 mixture), and the eventual UV influence on the oxidation process. Furthermore, we attempted to enhance the efficiency of the decolourization process by combining plasma and TiO_2 photocatalyst and to evaluate the synergic effect of non–thermal plasma and TiO_2 for the decomposition of RO 16 in aqueous solution.

Experimental Section

Chemicals and Sample Preparation

RO 16 (C.I. 17,757; CAS 20262–58–2; $C_{20}H_{17}N_3O_{11}S_3Na_2$, Sigma Aldrich) was used as a model pollutant. The TiO_2 nanopowders were prepared by a sol–gel method using tetrabutyltitanate (Ti $(OBu)_4$) as a precursor, hydrochloride acid as the catalyst, ethanol as the solvent and water for the hydrolysis. The hydrolysis and polycondensation reactions of Ti($OBu)_4$ were carried out on the ice–bath. The reagent molar ratio was Ti($OBu)_4$:HCl:EtOH:H_2O = 1:0.3:15:4 [43]. After the gelation, the wet gel was dried at 80 °C, and then calcinated at 500 °C for 1.5 h.

TiO_2 Characterization

Phase identification of TiO_2 sample was performed by X–ray powder diffraction (XRPD) (Ital Structures APD2000, Italy) using Cu–Kα radiation ($\lambda = 1.5406$ Å). The measurements were performed at room temperature in the 2θ range from 20 to 80° in a continuous scan mode with a step width of 0.1° and the counting time of 0.5 s/step. Software MDI Jade 5.0 was used for the calculation of the structural and microstructural parameters. The powder specific surface area of the sample was calculated following the multipoint BET procedure on the Quantachrome ChemBet-3000 setup. The nitrogen adsorption–desorption isotherm was obtained at 77 K. Morphology of the synthesized nanopowders has been studied on a Tescan MIRA3 field emission gun scanning electron microscope (FE-SEM), at 20 kV in high vacuum. The infrared (IR) transmission spectrum of TiO_2 using the potassium bromide pellet was measured on a Thermo Nicolet 6700 Fourier transform infrared spectrophotometer at the room temperature.

Treatment Setups

In Fig. 1 five different treatment setups are presented: plasma treatment – PT (Fig. 1a), PT with quartz glass (Fig. 1b), heterogeneous photocatalysis–HP (Fig. 1c), plasma coupled with catalyst—PC (Fig. 1d) and PC with quartz glass (Fig. 1e).

The plasma needle setup, which we have adapted for this research (Fig. 1a), consists of a body made of Teflon and a central copper electrode inserted in the glass tube 1 mm above the sample. Its electrical properties are presented by Zaplotnik et al. [44]. Discharge is generated at the tip of a copper wire. Ar (5.0 purity) and a mixture of Ar and O_2 ($Ar/10\%O_2$) are used as feed gases. The flow rates vary from
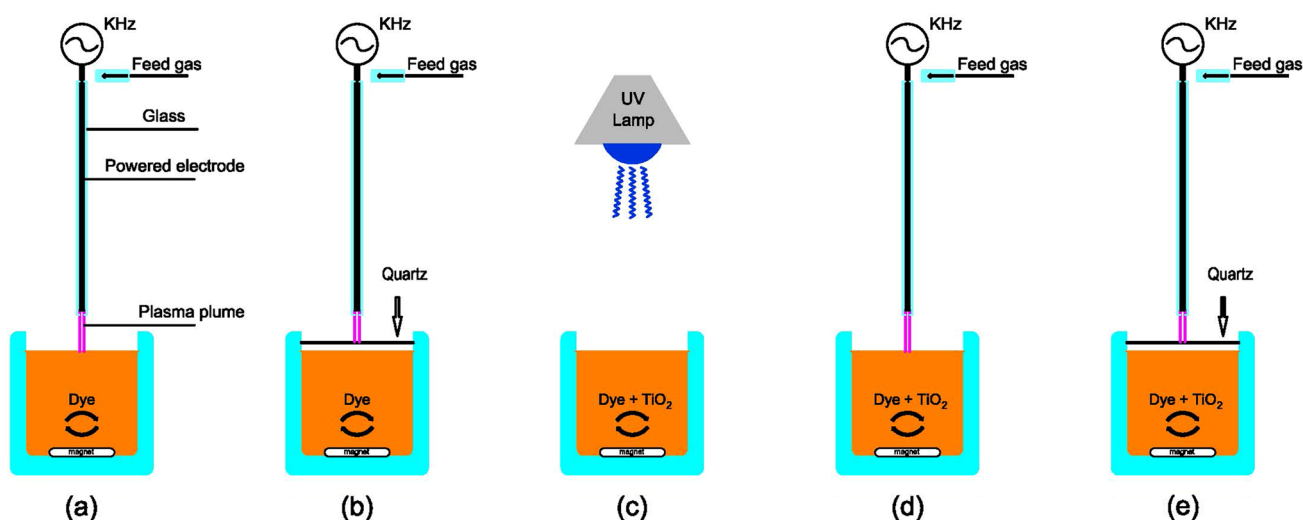
Fig. 1 Different treatment setups used in the study: **a** Plasma treatment (PT), **b** Plasma treatment (PT) with quartz glass, **c** semiconductor heterogeneous photocatalysis (HP), **d** plasma coupled with catalyst (PC), **e** plasma coupled with catalyst (PC) with quartz glass

1 to 4 slm. The exposure times for all treatments range from 5 to 150 min.

In the first set of experiments (PT, Fig. 1a) we have analysed the decolourisation effects of plasma needle on the RO 16 solution, by changing its flow rate and feed gas composition. UV contribution of plasma needle to decolourisation process was investigated by putting a quartz glass (190 to 2500 nm) between the sample and the plasma source (Fig. 1b). In such a way only UV contribution from plasma source to the decolourisation process can be estimated, as in this configuration reactive radicals generated in plasma are prevented to reach the sample surface and oxidize the dye.

The photocatalytic experiment (Fig. 1c) was performed as follows: TiO_2 (2 g/l as the optimal concentration for RO 16 photodegradation) [13] was added to the RO 16 solution and magnetically stirred for 30 min in the dark in order to uniformly disperse nanopowder and to achieve the adsorption–desorption equilibrium. Afterwards, a mercury lamp (300 W, UVA/UVB, Osram Vitalux) as a light source placed 40 cm above the sample was switched on in order to initiate the photocatalytic reaction.

In the third set of experiments, we have used plasma needle in the presence of TiO_2 (Fig. 1d) in order to examine whether there is a synergic oxidation outcome. The effects of plasma generated UV radiation on the TiO_2 activation was investigated by using quartz glass in order to restrict reactive radicals to participate in the dye oxidation process (Fig. 1e).

Decolourisation Measurements

The above–mentioned experiments were conducted in magnetically stirred thermostated glass vessel. The concentration of dye solution (c = 50 mg/l) and working volume

(V = 25 ml) were kept fixed during all treatments. At certain time intervals, aliquots were withdrawn, centrifuged (in the case of TiO_2) and analysed on UV/VIS spectrophotometer (Varian Superscan 3, USA). RO 16 concentration was followed by measuring the variation of the intensity of main absorption band at 494 nm. This absorption band originates from $n \rightarrow \pi^*$ transition in the chromophore group (–N=N–) and its disappearance indicates that the main chromophores of the dye were destroyed. The measurements were repeated three times to check their reproducibility and the mean value was taken into consideration.

Detection of Reactive Hydroxyl Radicals

In order to detect the formation of free hydroxyl radicals, photoluminescence (PL) measurements were performed using terephthalic acid (TA), which in reaction with hydroxyl radicals induced on the photocatalysts surface produces highly fluorescent 2-hydroxyterephthalic acid. The experiment was carried out at room temperature, where 20 mL of working solution was prepared using distilled water in such a manner that the concentrations of the terephthalic acid (TA) and NaOH were 5×10^{-4} M and 2×10^{-3} M, respectively. The nanopowder TiO_2 (50 mg) was dispersed and solution was constantly stirred on a magnetic stirrer. A 300 W UV lamp, (Osram Vitalux) was used as a light source, placed 40 cm above the solution. At given time intervals (5, 10, 15, 20 and 30 min), aliquots were withdrawn, centrifuged and filtered to remove the catalyst particles. The room- temperature PL spectra at 425 nm of the supernatant were analyzed on the Fluorescence Spectrometer (Spex Fluorolog) using 320 nm as excitation light, in order to estimate the concentration of 2- hydroxyterephthalic acid.

Results and Discussion

The RO 16 decolourisation mechanism by plasma needle is dependent on the generation of plasma directly above the treated sample in the continuous gas phase simultaneously contacting molecules, clusters, aerosols, droplets, and planar surfaces of the liquid [45]. The complexity of physical and chemical phenomena, which appear during the discharges in both gas and liquid phase, is considerable. For this reason, we studied different plasma needle treatment parameters (e.g. feed gas flow rate and composition) and their influence on the RO 16 oxidation process (decolourisation). Later, we have also studied combined plasma–heterogeneous photocatalysis in order to examine the potential oxidation synergic effects of plasma and catalyst and to verify whether plasma UV radiation was adequate to activate the TiO_2 surface. The TiO_2 based heterogeneous photocatalysis on RO 16 degradation was used as a benchmark.

Effects of Plasma Treatment on the RO 16 Decolourisation

Producing concurrently large amount of active species with high reduction potential (Table 1) [46] UV radiation and shock waves, plasma decomposes organic matter with no additional procedures and no sludge production [47]. Chemically reactive radicals reach the liquid surface, diffuse into the bulk, and oxidize the hazardous component. Therefore, plasma chemistry, which occurs in these atmospheric and subsequently aqueous conditions, is highly relevant to the evolution of the reactive radicals and their influence on the target compound. Figure 2 illustrates the formation mechanisms of possible reactive species, whereas the oxidation potential of plasma reactive species are given in Table 1.

Key reactions from Fig. 2 which take place during the air discharge are described in the following sections.

Depending on the electron energies formed by electrical discharges, high–energy electrons collide with ambient molecules resulting in the several possible reactions such as excitation, dissociation, electron capture or ionization, (Eqs. 1–5):
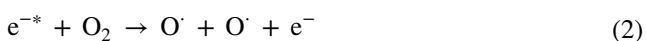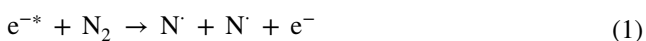
$$e^{-*} + N_2 \rightarrow N^{\cdot} + N^{\cdot} + e^- \tag{1}$$

$$e^{-*} + O_2 \rightarrow O^{\cdot} + O^{\cdot} + e^- \tag{2}$$

Table 1 Oxidation potential of plasma reactive species

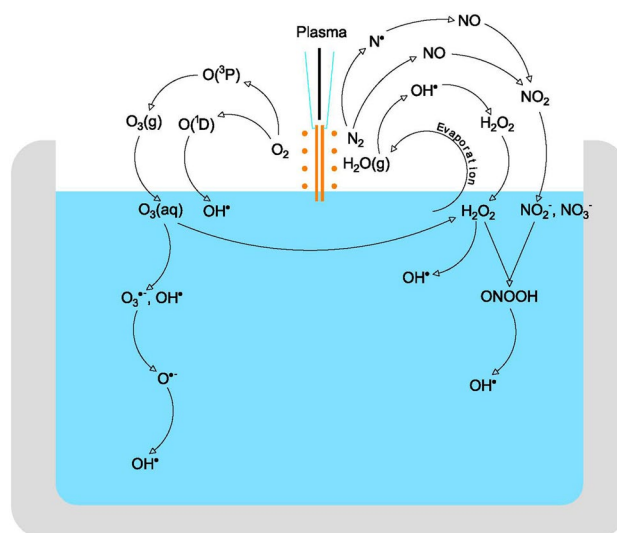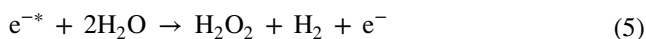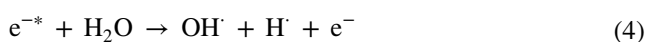|		
$OH^{\cdot} + H^+ + e^- \rightarrow H_2O$	E^0_{OH/H_2O}	2.85 V
$O^{\cdot} + 2H^+ + 2e^- \rightarrow 2H_2O$	E^0_{O/H_2O}	2.42 V
$O_3 + 2H^+ + 2e^- \rightarrow O_2 + H_2O$	$E^0_{O_3/O_2}$	2.07 V
$H_2O_2 + 2H^+ + 2e^- \rightarrow 2H_2O$	$E^0_{H_2O_2/H_2O}$	1.77 V
$O_2 + 4H^+ + 4e^- \rightarrow 2H_2O$	$E^0_{O_2/H_2O}$	1.23 V

Fig. 2 Important chemical species in the gas and liquid phase induced by Ar fed plasma needle discharge

$$e^{-*} + H_2O \rightarrow O(^1D) + O^{\cdot} + e^- \tag{3}$$

$$e^{-*} + H_2O \rightarrow OH^{\cdot} + H^{\cdot} + e^- \tag{4}$$

$$e^{-*} + 2H_2O \rightarrow H_2O_2 + H_2 + e^- \tag{5}$$
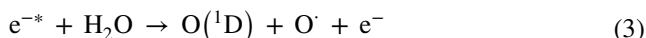
Further important reactions related to the formation of the primary long live reactive species (O_3, H_2O_2, NO_3^-, NO_2^-) and their dissolution in water are described below. $O^{\cdot}$ generated in air plasma together with O_2 produce O_3 which reacting with water molecules forms H_2O_2 (Eqs. 6–7). Additional H_2O_2 generation mechanism is through the recombination reaction of $OH^{\cdot}$ radicals (Eq. 8).

$$O^{\cdot} + O_2 + M \rightarrow O_3 + M$$
$$(M - \text{third collision partner, which may be Ar, } O_2, N_2, \text{ etc.}) \tag{6}$$

$$O_3 + H_2O \rightleftharpoons O_2 + H_2O_2 \tag{7}$$

$$OH^{\cdot} + OH^{\cdot} \rightarrow H_2O_2 \tag{8}$$
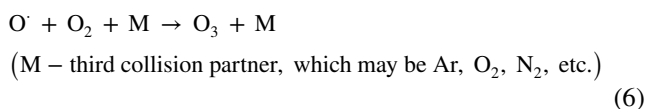
Nitrogen oxides (NO, NO_2) formed in air plasma through reactions between O_2 and N_2 dissolve in the solution creating nitrites and nitrates (Eqs. 9–10) and consequently forming the peroxynitrous acid through the reaction of nitrites with hydrogen peroxide (Eq. 11) [32].

$$2NO_2 + H_2O \rightarrow NO_2^- + NO_3^- + 2H^+ \tag{9}$$

$$NO + NO_2 + H_2O \rightarrow 2NO_2^- + 2H^+ \tag{10}$$

$$NO_2^- + H_2O_2 + H^+ \rightarrow O = NOOH + H_2O \quad (11)$$
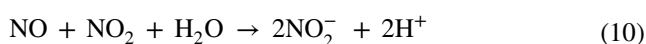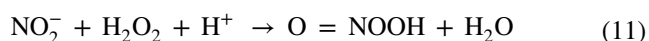
Occurrence of even more reactive species (OH·, O·, NO$_2$·etc.) (Eqs. 12–18) can be expected as well, but because of their short lifetime they can react directly with a pollutant only in its current encirclement where the reaction occurs [5, 48, 49]. Among them, the most influential reactive species found in electric discharges is OH·. It is a very powerful oxidizing agent with a standard reduction potential of $E^0 = 2.8$ V [50] and lifetime (≈ 200 μs in the gas phase and 10^{-9} s in an aqueous solution). Although it has very short lifetime there are additional OH· formation mechanisms in the bulk as a consequence of the transfo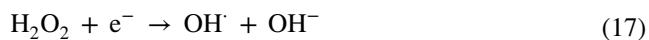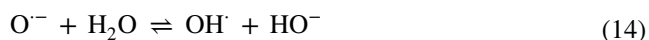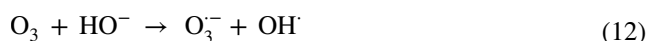rmation of above–mentioned long lifetime species. Several mechanisms are responsible for the OH· formation: electron impacts dissociation of H$_2$O (Eq. 4); ozone dissolution in water [51] (Eqs. 12–14); reactions of excited O atoms and O· with water (Eqs. 15, 16); reaction of e$^-$ and H$_2$O$_2$ (Eq. 17) or via reaction of peroxynitrous acid in water (Eq. 18).

$$O_3 + HO^- \rightarrow O_3^- + OH· \quad (12)$$

$$O_3^- \rightarrow O^- + O_2 \quad (13)$$

$$O^- + H_2O \rightleftharpoons OH· + HO^- \quad (14)$$

$$O(^1D) + H_2O \rightarrow 2OH· \quad (15)$$

$$O· + H_2O \rightarrow 2OH· \quad (16)$$

$$H_2O_2 + e^- \rightarrow OH· + OH^- \quad (17)$$

$$O = NOOH \rightleftharpoons NO_2· + OH· \quad (18)$$

The degradation of dyes is mainly attributed to the attack of these oxidative species, which are among the most influential reactive species found in electric discharges [52] that initially attack the most sensitive chromophore group (–N=N–). The decolorization process of RO16 usually manifests as decrease of the 494 nm band intensity, relatively faster than for other bands. Therefore, it can be concluded that reactive species like OH· initially attack the chromophore group (–N=N–) followed by the degradation of aromatic part, benzene and naphthalene rings, of the dye molecule [38].

The OH· addition to the –N=N– bond probably produces the hydrazyl type radical forms, –·N–N(OH)– as reported in the literature [5], leading to the destruction of the colour in the visible range and finally mineralization into totally innocuous gaseous nitrogen [38]. The oxidation of nitrogen containing organic molecules leading to the NO$_x$ generation is also reported [53], but in small quantities not harmful for the environment.

Influence of Different Flow Rates and Composition of Feed Gas on the Decolourisation Rate

The absorption spectral changes of RO 16 solution at different irradiation time during PT with Ar as feed gas (1 slm), are presented in Fig. 3. The intensity of absorption peaks in the visible region (494 and 386 nm), as well as the intensity of peaks in the ultraviolet region (297 and 254 nm), rapidly decreased in the initial stage of the PT and after 90 min none of the absorption peaks were observed.

The kinetics of RO 16 decolourisation under PT process at different flow rates of Ar is given in Fig. 4. C_0 and C_t represent the initial dye concentration and the dye concentration at reaction time t. The RO 16 concentration of each treated sample was determined using a calibration curve which is

Fig. 3 Absorbance spectra of RO 16 for different PT times by using Ar(1slm) as feed gas
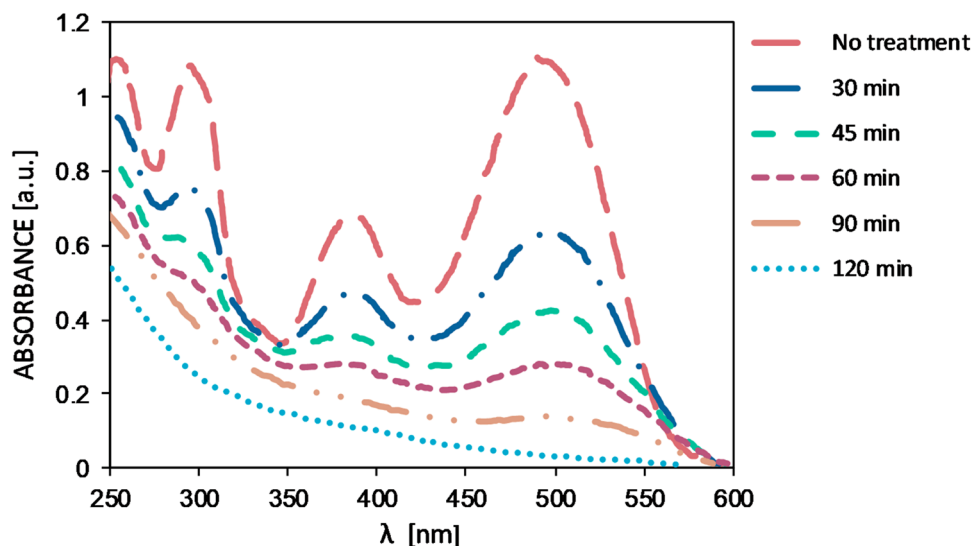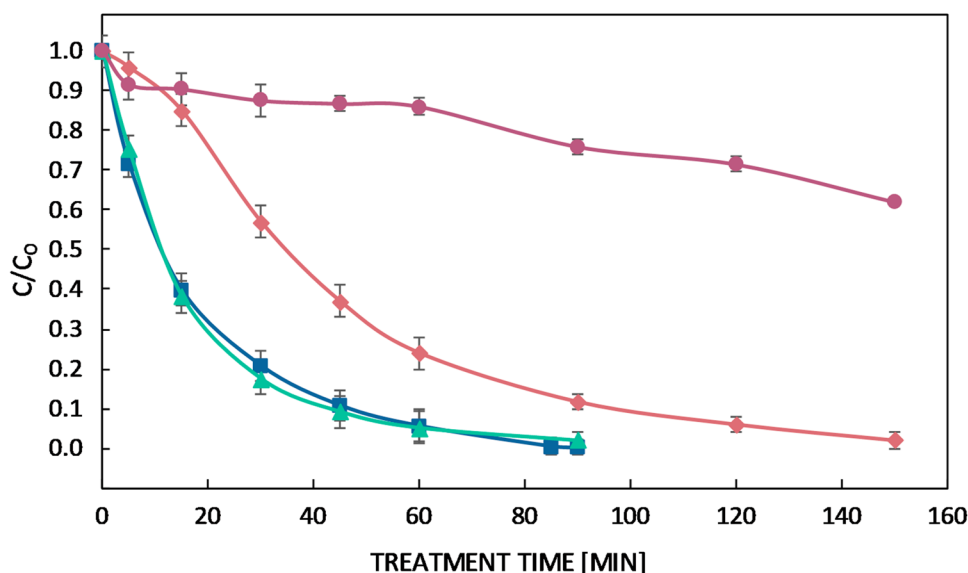
Fig. 4 Decolourisation of RO 16 (c = 50 mg/L, V = 25 mL) under PT treatment using Ar (1 and 4 slm); Ar/O$_2$ (1 slm) and Ar (4 slm + Quartz) as feed gas. Symbols: filled diamond- Ar 1 slm; filled rectangle- Ar 4 slm; filled triangle- Ar/O$_2$ 1 slm; filled circle – 4 slm with Quartz

previously established with prepared standards and theirs related absorbances. It can be observed that RO 16 decolourisation was faster for the increased flow rate of Ar (4 slm) and almost total decolourisation was achieved after 90 min. It is obvious that generation of radicals in plasma depends on gas flow rate. The higher is the flow rate, the faster is the decolourisation. However, the efficiency of radicals generation and plasma chemistry can be also tailored by changing the feed gas composition. For that purpose, in Fig. 4 is presented the kinetics of RO 16 decolourisation when 10% O$_2$ was introduced into Ar flow rate of 1 slm.

The O$_2$ introduction into the feed gas has the similar decolourisation effect on RO 16 as increasing of Ar flow rate from 1 to 4 slm. It is evident that adding only 10% O$_2$ to the feed gas (Ar, 1slm) the decolourisation of RO 16 is faster, reaching almost complete decolourisation after 90 min.

The introduction of O$_2$ into the feed gas evidently influenced the oxidation process kinetics. The better efficiency of the RO 16 oxidation with the addition of O$_2$ can be a consequence of at least two reasons. The most apparent reason is that higher amount of active species, like OH$^.$, can be formed when O$_2$ is introduced in Ar because of the lower energy of the first ionization of O$_2$ (12.1 eV) compared to Ar (15.8 eV). In their work, Gumuchian et al. [24] measured amount of OH$^.$ in different compositions of feed gases and concluded that in Ar/O$_2$ feed gas mixture, the concentration of OH$^.$ was the highest [24]. Beside this, atomic oxygen can react directly with organic pollutants, and together with O$_2$ can produce very reactive ozone (Eq. 6). Nevertheless, in the paper of Miyazaki et al. [54] it was shown that very small amount of ozone was produced if the Ar concentration in Ar/O$_2$ feed gas mixture is equal or higher than 80%. Since in our experiments 90% of Ar, was used, we suppose that ozone contribution in these experiments is not of great

importance. Evidently, the presence of O$_2$ in the feed gas significantly improves the oxidation potentials of plasma needle, presumably due to the formation of more reactive species (Eqs. 2, 15–16).

In order to investigate an isolated effect of plasma generated UV light on dye oxidation, the quartz glass was placed between plasma source and RO 16 solution to block plasma–generated species from reaching the surface, allowing only UV light to pass to the sample. Namely, for 1 slm of Ar flow rate there was no observed UV contribution, while for 4 slm Ar flow rate UV dependent decolourisation was less than 15% after 60 min of treatment. For that reason, it can be concluded that isolated UV light cannot be considered as significant contributing factor to decolourising process of the dye.

Effects of the Heterogeneous Photocatalysis on the RO 16 Removal

Among the semiconductors, titanium dioxide (TiO$_2$) is by far the most frequently studied photocatalyst, highly abundant in nature, photochemically very stable under ambient conditions and environmentally friendly. Among the three TiO$_2$ crystal phases: anatase, rutile and brookite, the anatase is the most frequently applied photocatalyst showing excellent photocatalytic activity, although its application is restricted to the utilization of UV light due to the large band gap (E$_g$ ~ 3.2 eV).

The photochemical decolorization of RO 16 was studied by heterogeneous photocatalysis, using anatase TiO$_2$ nanopowders as catalyst and UV lamp as an excitation source. TiO$_2$ nanopowders were synthesized by sol–gel method and the XRPD pattern of TiO$_2$ is presented in Fig. 5a.

The main diffraction peaks correspond to the anatase crystallite phase (PDF card 782,486) and no other phases were detected. Characteristic Miller indices are denoted for the main diffraction peaks. The average crystallite size, $<D>$ and average lattice strain of the prepared sample were calculated using Williamson–Hall Method and are presented in Table 2 together with cell parameters [55].

To determine the surface area of synthesized nanopowder the nitrogen adsorption–desorption isotherm at 77 K has been measured and shown in Fig. 5b. Prior to adsorption, the sample was outgassed for 1 h under vacuum at room temperature, and additionally for 16 h at 110 °C at the same residual pressure. The specific surface areas (S_{BET}) of sample is calculated from the linear part of the adsorption isotherm by applying the Brunauer-Emmet-Teller (BET) equation [56]. The curves may be interpreted as type IV [57], typical for mesoporous materials, with an H2-type hysteresis loop,

Table 2 The unit cell parameters, average crystallite size $<D>$ and micro strain values of TiO_2

Sample name	Unit cell parameters a, c (Å)	Williamson–Hall method	
		$<D>$ (nm)	Microstrain (%)
TiO_2	$a = 3.784(3)$ $c = 9.53(0)$	24	0.301

indicating the presence of pore networks. The reported value of the BET specific surface area (S_{BET}) is 52 m^2 g^{-1}.

TiO_2 nanoparticles produced by sol–gel method are not porous itself, so the porous structure originates from interparticle voids. From the FE-SEM images given in the Fig. 5c, d, it is clear that we are dealing with spherical and agglomerated nonporous nanoparticles, where the particle size ranges from 30 to 100 nm.
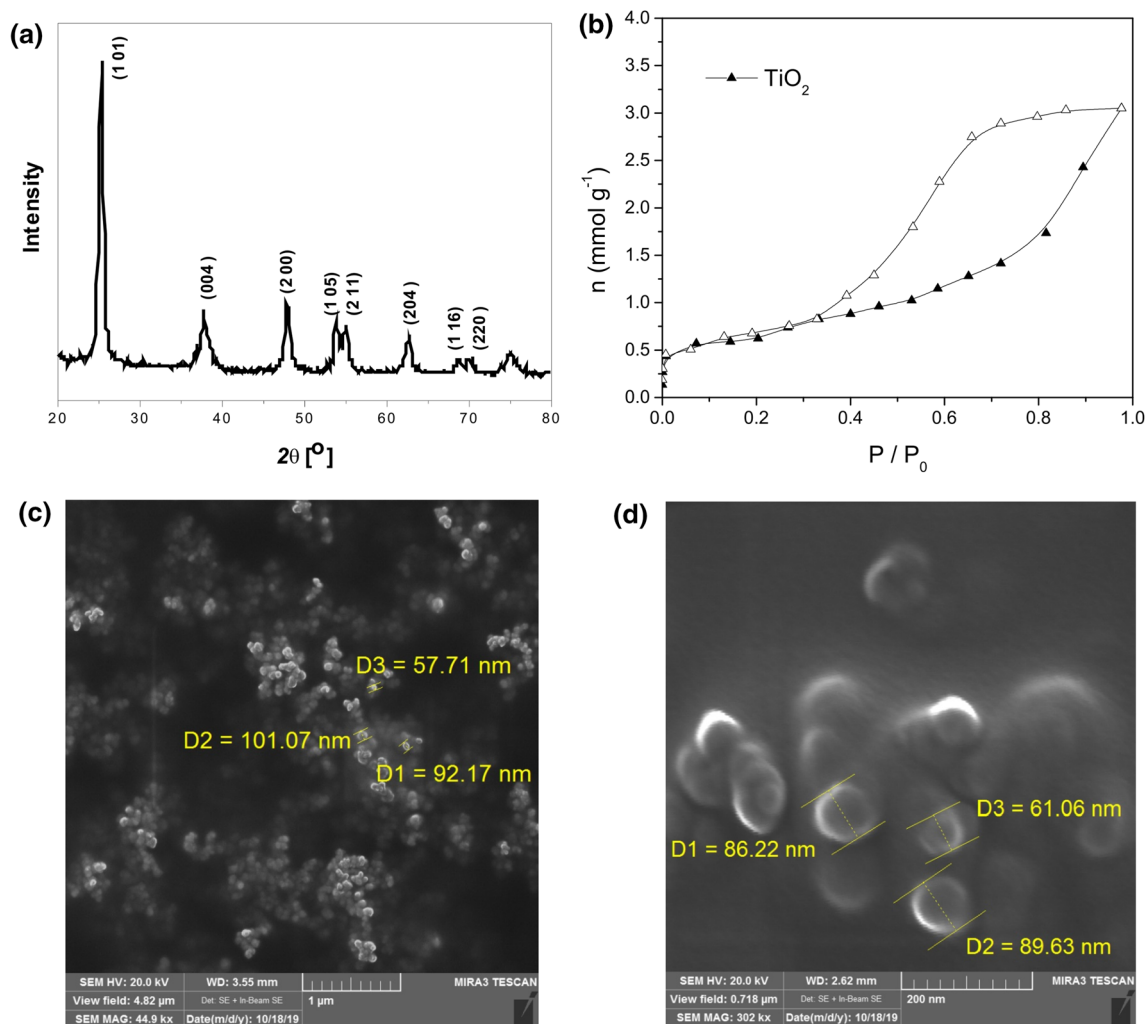

Fig. 5 XRPD pattern of TiO_2 nanopowder obtained by the sol–gel method (**a**); The nitrogen adsorption–desorption isotherm of synthesized TiO_2 nanopowder at 77 K (**b**); FE-SEM images of TiO_2 sample (**c**), (**d**)

When the RO 16–TiO$_2$ solution is illuminated with UV irradiation, main processes, which take place on the nanoparticles surface are illustrated in Fig. 6.

When TiO$_2$ solution is illuminated with light having energy greater than the band gap of the semiconductor, photogenerated electron (e_{cb}^-) –hole (h_{vb}^+) pairs are formed (Eq. 19). These pairs can be recombined within the bulk of the material or at the particle surface. Furthermore, the (e_{cb}^-) and (h_{vb}^+) can migrate to the semiconductor surface [38, 58] and react with adsorbed reactants leading to increased photocatalytic efficiency. The photodegradation mechanism can be summarized as follows:

$$TiO_2 + h\nu \xrightarrow{energy} e_{cb}^- + h_{vb}^+ \tag{19}$$

$$e_{cb}^- + h_{vb}^+ \rightarrow thermal\ energy \tag{20}$$

$$h_{vb}^+ + dye \rightarrow oxidation\ of\ organic\ molecule \tag{21}$$

$$h_{vb}^+ + H_2O \rightarrow H^+ + OH^. \tag{22}$$

$$h_{vb}^+ + OH^- \rightarrow OH^. \tag{23}$$

$$e_{cb}^- + O_2 \rightarrow O_2^- \tag{24}$$

The direct oxidation of organic substances is possible since the holes (h_{vb}^+) have high oxidative potential (Eq. 21), or they can also react with H$_2$O (Eq. 22) and OH$^-$ (Eq. 23) producing very active and unselective OH$^.$ radicals [14, 38, 58]. On the other hand, photogenerated electrons can react with O$_2$ molecules dissolved in water forming superoxide

radical anion (O$_2^{.-}$) (Eq. 24) leading to the production of other very reactive species as follows:

$$O_2^- + H^+ \rightarrow HO_2^. \tag{25}$$

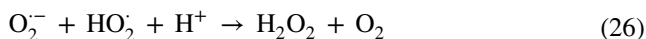$$O_2^- + HO_2^. + H^+ \rightarrow H_2O_2 + O_2 \tag{26}$$

Figure 7 shows the decolourisation rate of RO 16 for TiO$_2$ nanopowder activated by UV lamp. As can be seen from Fig. 7, photodegradation of the dye reached about 90% after 90 min of treatment, similar to the decolourisation effects of plasma needle for Ar 1 slm (Fig. 4). No detectable degradation of RO 16 was registered without the presence of TiO$_2$ sample (triangles on Fig. 7).

The presence of H$_2$O and O$_2$ molecules is crucial for generation of very reactive radicals. In the presence of H$_2$O and O$_2$ molecules, highly reactive radicals such as OH$^.$, O$_2^{.-}$ and HO$_2^.$, generated through processes of photodegradation, substantially contribute to the degradation of organic molecules/pollutants. However, the most important contribution and benefits among these processes arise from reactions accompanying generation of hydroxyl radicals. These radicals are considered as very strong and nonselective oxidizing species [59, 60]. The presence of functional groups at the surface of TiO$_2$ affects the formation of hydroxyl radicals. Infrared spectroscopy is used to analyse the surface of TiO$_2$. The IR spectrum of TiO$_2$ nanopowder is presented in Fig. 8a in the range from 500 to 4000 cm^{-1}. The main bands of O−H groups and H$_2$O are denoted with arrows. Namely, a wide band around ~ 3400 cm^{-1}, corresponds to stretching vibration of the O−H bond involved in hydrogen bonding O−H···O, whereas the band around ~ 1600 cm^{-1} can be ascribed to the bending mode of the water molecules H−O−H.

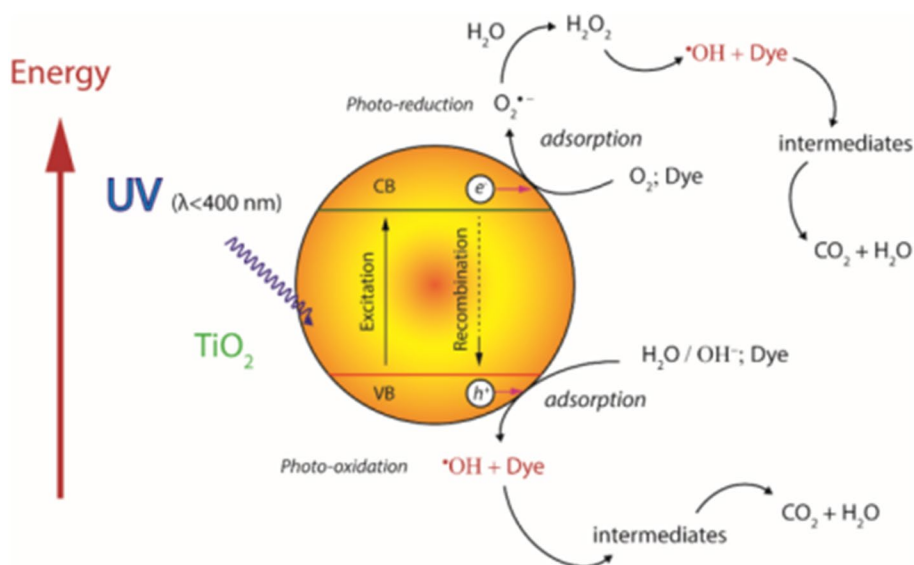**Fig. 6** Formation of e^-/h^+ pars in TiO$_2$ nanoparticles and catalytic processes on TiO$_2$ surface

Fig. 7 Decolourisation efficiency of RO 16 (c = 50 mg/l, V = 25 ml) by using TiO$_2$ (c = 2 g/l) under UV irradiation. Symbols: filled circle- RO 16 + UV + TiO$_2$; filled triangle RO 16 + UV
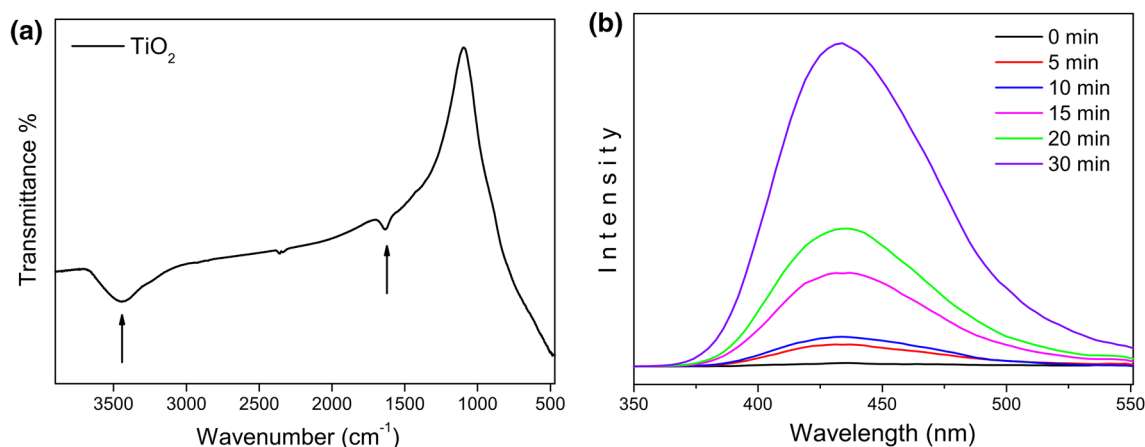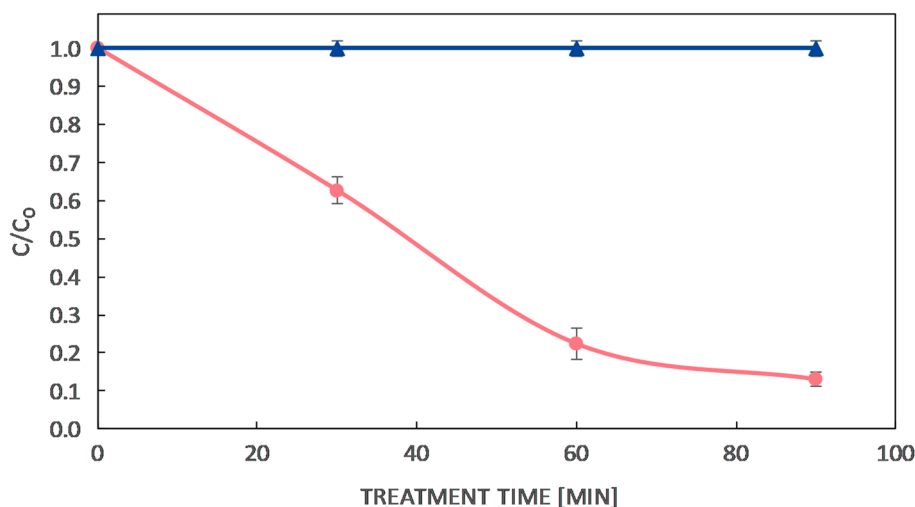

Fig. 8 IR spectrum of TiO$_2$ nanopowder (**a**), PL spectral changes of a TA–OH solution generated by TiO$_2$ under UV light irradiation (**b**)

The IR spectrum confirmed existence of O−H groups and water molecules (H$_2$O), on the surface of TiO$_2$ nanopowder (Fig. 8a), implying that generation of OH˙ radicals in high concentration is likely to occur.

Since the hydroxyl radicals are considered the primary oxidizing species their presence on the surface of the UV illuminated photocatalyst can be confirmed in reaction with terephthalic acid (TA) as a probe molecule. This acid reacts with OH˙ radicals, generated at the water/TiO$_2$ interface, forming a highly fluorescent product: 2-hydroxyterephthalic acid (TA-OH), with intensive peak at about 425 nm [61]. Since PL peak intensity is proportional to the amount of generated OH˙ radicals, by monitoring the changes in the intensity of 425 nm peak the hydroxyl radicals could be detected indirectly. From the Fig. 8b, it can be observed that the intensity of 425 nm peak increases in time, meaning that the concentration of hydroxyl radicals also increases [61, 62]. The spectrum labelled as "0 min" represents the pure TA solution recorded prior the UV

irradiation source. These results clearly demonstrated that with increasing illumination time the increasing amount of OH˙ radicals are formed at TiO$_2$/water interface, responsible for dye degradation.

Effects of the Plasma–Tio$_2$ Catalyst Treatment on the RO 16 Removal

Figure 9 illustrates the degradation kinetics of RO 16 during the combined TiO$_2$ and non–thermal plasma treatment—PC treatment. As can be seen from Fig. 9, PC treatment is more efficient than PT (Fig. 4) for the same Ar flow rate of 1 slm. Namely, after 15 min more than 40% of dye was degraded under the PC treatment, whereas under PT the photodegradation of dye reached only15%. It is also evident that the time for complete decolourisation reduced from 150 to 120 min. Similar effect was observed with increased feed gas flow rate (4 slm) when the time for complete RO 16 decolourisation was shortened from 90 min (PT) to 60 min (PC). Improved

Fig. 9 Decolourisation of RO 16 (c = 50 mg/L, V = 25 mL) under PC treatment by using TiO_2 (c = 2 g/L) and Ar (1, 4 slm) as feed gas. Symbols: filled diamond- Ar 4 slm + Quartz + TiO_2; filled rectangle- Ar 1 slm + TiO_2; filled triangle- Ar 1 slm + Quartz + TiO_2; filled circle – Ar 4 slm + TiO_2
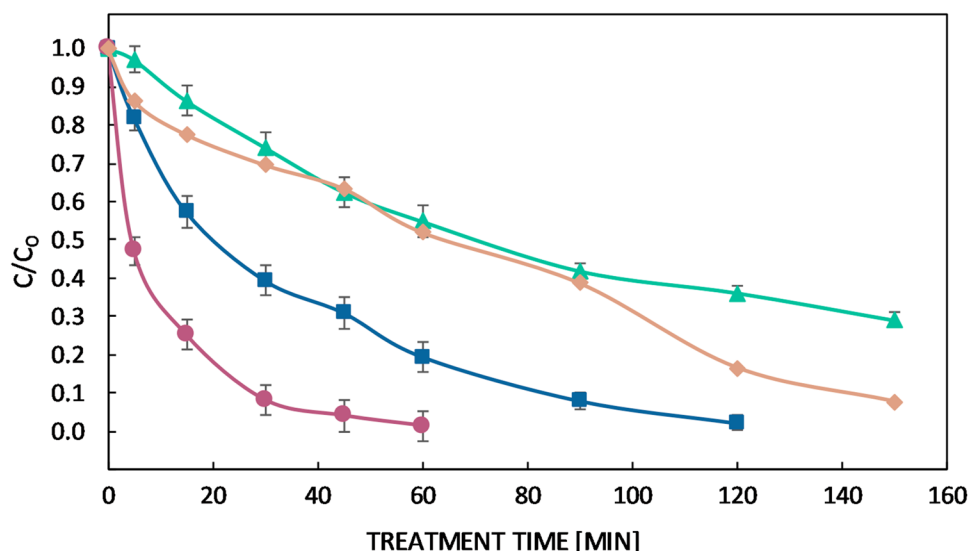
decolourization of RO 16 can be ascribed to the synergic effect of plasma–photocatalysis process.

In order to investigate an isolated effect of plasma generated UV light on dye degradation during the PC treatment, we placed a quartz glass between plasma source and TiO_2–dye solution, allowing only UV light to pass to the solution. From Fig. 9 it is evident that the dye degradation process was much slower compared to the PC experiment without quartz glass. Hence, it is clear that UV emission from the plasma needle activates TiO_2 leading to enhanced synergic effects for pollutant removal.

The oxygen addition (10%) to the feed gas (1 slm of Ar) further improved the PC decolourisation process, i.e. the synergic effect between plasma and photocatalyst was more pronounced, as the total decolourisation was achieved after 60 min (Fig. 10).

The experimental kinetic data for all presented treatments followed pseudo first–order kinetics and were fitted by pseudofirst–order reaction, $ln(C/C_o) = kt$ where k is pseudo–first order constant rate, t the treatment time. The constant rates and correlation coefficient (R^2) for different treatment setups (PT, heterogenous photocatalysis and PC) are presented in Table 3.

In the case of PT treatment, with increasing Ar flow rate from 1 to 4 slm, the constant rate k increases from 24.5 to 51.8×10^{-3} min^{-1}. The k values for Ar 4 slm ($k = 51.8 \times 10^{-3}$ min^{-1}) and mixture of Ar/O_2 1 slm ($k = 47.4 \times 10^{-3}$ min^{-1}) are comparable implying similar final oxidation effect. PT treatment with Ar 1 slm (k = 24.5×10^{-3} min^{-1}) manifest almost the same oxidation degree as heterogeneous photocatalysis (k = 22.8×10^{-3} min^{-1}). This is very important knowing that

Fig. 10 Decolourisation of RO 16 (c = 50 mg/L, V = 25 mL) under the PC treatment using TiO_2 (c = 2 g/L) and Ar (1slm) and Ar/O_2 (1slm) as feed gas. Symbols: filled diamond- Ar/O_2 1 slm + TiO_2; filled rectangle- Ar 1 slm + TiO_2
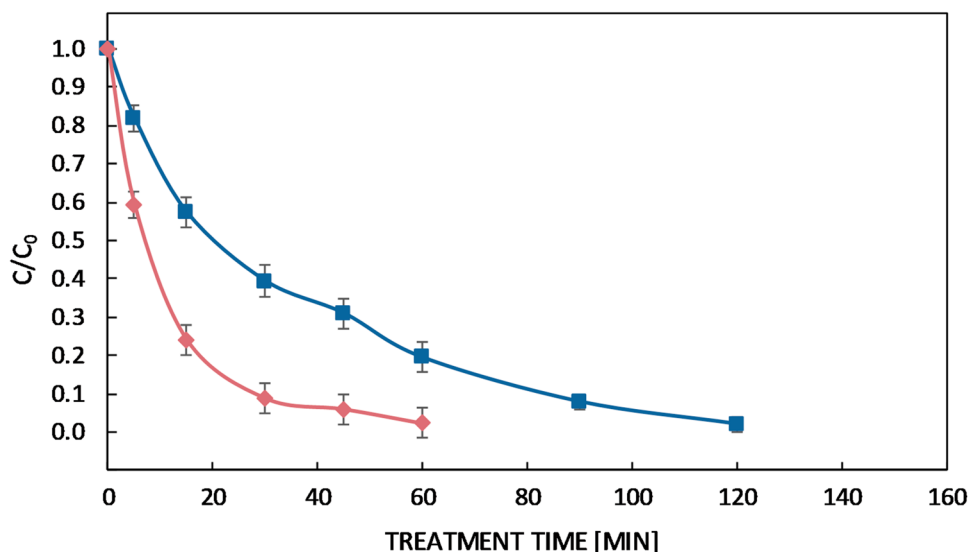
Table 3 Constant rates for different treatment setups

Treatment setups		Constant rates, $k \times 10^{-3}$ (min^{-1})	R^2
PT	1 slm (Ar)	24.5	0.988
PT	4 slm (Ar)	51.8	0.993
PT	1 slm (Ar/O$_2$)	47.4	0.970
HP	TiO$_2$ + UV 300 W	22.8	0.975
PC	1 slm (Ar) + TiO$_2$	30.1	0.986
PC	1 slm (Ar/O$_2$) + TiO$_2$	66.2	0.953
PC	4 slm (Ar) + TiO$_2$	73.1	0.971
PC with quartz	1 slm (Ar) + TiO$_2$ + Quartz	8.9	0.986
PC with quartz	4 slm (Ar) + TiO$_2$ + Quartz	15.5	0.943

plasma needle needs smaller power consumption for TiO$_2$ activation than UV lamp.

In the case of PT treatment with quartz glass, the UV radiation emitted from the 1 slm plasma needle was not enough to decolourise RO 16 dye by itself. For increased Ar flow rate (4 slm) low value of constant rate ($k = 3.1 \times 10^{-3}$ min^{-1}) confirmed that UV light cannot be considered as significant factor during the process of decolourisation.

As expected, the best removal efficiency was obtained with combined plasma/TiO$_2$ process (PC). Namely, among all experiments with different setups (HP, PT and PC), the PC rate constants are the highest (see Table 3).

This is particularly evidenced for increased Ar flow rate (4 slm) when the rate constant is almost 50% higher for PC than for PT treatment ($k = 73.1 \times 10^{-3}$ min^{-1} vs. $k = 51.8 \times 10^{-3}$ min^{-1}). Therefore, it can be concluded that the synergic effect of two AOPs is evident and very dependent on the flow rate of feed gas and gas mixture. PC experiment with quartz glass demonstrated that UV radiation from the plasma needle source evidently has influence on the TiO$_2$ photolytic activity and contribute to the RO 16 decolourisation process. Further investigations will be directed to the estimation of the optimal TiO$_2$ concentration, identification of RO 16 oxidation by–products and determination of their levels of toxicity.

Conclusions

In this paper, we investigated the RO 16 decolourisation process by using two advanced oxidation processes (plasma discharge process and heterogenous photocatalysis), as well as combined plasma/TiO$_2$ process. For that purpose, we have developed a low power atmospheric pressure plasma source (plasma needle). The anatase TiO$_2$ nanopowders, used in experiments, were synthetized by sol–gel method. In the case of only plasma treatment, it was demonstrated that both flow rate and feed gas composition had significant effect on

dye removal. The presence of O$_2$ in the feed gas, as well as, increased feed gas flow rate significantly improved the process of RO16 decolourisation as compared with the TiO$_2$ based heterogenous photocatalysis.

The RO 16 degradation efficiency significantly improved when plasma was combined with TiO$_2$ photocatalyst. Such an improvement can be attributed to synergic effects of radicals generated by the plasma in the gas phase and delivered to the liquid and radicals generated directly in the liquid on the surface of TiO$_2$. The synergic effect of two AOPs was more pronounced at higher flow rate of the plasma feeding gas. Accordingly, we can conclude that simultaneous application of different AOPs can offer better solution for wastewater treatment and improves energy utilization efficiency when using plasma needle as UV source.

Compliance with Ethical Standards

Conflict of interest The authors declare that they have no conflict of interest.

References

1. Bizani, E., Fytianos, K., Poulios, I., Tsiridis, V.: Photocatalytic decolorization and degradation of dye solutions and wastewaters in the presence of titanium dioxide. J. Hazard. Mater. **136**, 85–94 (2006)
2. de Lima, R.O.A., Bazo, A.P., Salvadori, D.M.F., Rech, C.M., de Palma, O.D., de Aragão, U.G.: Mutagenic and carcinogenic potential of a textile azo dye processing plant effluent that impacts a drinking water source. Mutat. Res. Genet. Toxicol. Environ. Mutagen. **626**(1–2), 53–60 (2007)
3. Gao, J., Zhang, Q., Su, K., Chen, R., Peng, Y.: Biosorption of Acid Yellow 17 from aqueous solution by non-living aerobic granular sludge. J. Hazard. Mater. **174**, 215–225 (2010)
4. Dutta, S., Saha, R., Kalita, H.: Rapid reductive degradation of azo and anthraquinone dyes by nanoscale zero-valent iron. Environ. Technol. Innov. **5**, 176–187 (2016)
5. Dojčinović, B.P., Roglić, G.M., Obradović, B.M., Kuraica, M.M., Kostić, M.M., Nešić, J., Manojlović, D.D.: Decolorization of reactive textile dyes using water falling film dielectric barrier discharge. J. Hazard. Mater. **192**, 763–771 (2011)
6. Chandanshive, V.V., Kadam, S.K., Khandare, R.V., Kurade, M.B., Jeon, B.H., Jadhav, J.P., Govindwar, S.P.: In situ phytoremediation of dyes from textile wastewater using garden ornamental plants, effect on soil quality and plant growth. Chemosphere **210**, 968–976 (2018)
7. Pandey, A., Singh, P., Iyengar, L.: Bacterial decolorization and degradation of azo dyes. Int. Biodeterior. Biodegrad. **59**, 73–84 (2007)
8. Ghezzar, M.R., Abdelmalek, F., Belhadj, M., Benderdouche, N., Addou, A.: Enhancement of the bleaching and degradation of

textile wastewaters by Gliding arc discharge plasma in the presence of TiO2 catalyst. J. Hazard. Mater. **164**(2–3), 1266–1274 (2009)

9. Tichonovas, M., Krugly, E., Racys, V., Hippler, R., Kauneliene, V., Stasiulaitiene, I., Martuzevicius, D.: Degradation of various textile dyes as wastewater pollutants under dielectric barrier discharge plasma treatment. Chem. Eng. J. **229**, 9–19 (2013)

10. Tijani, J.O., Fatoba, O.O., Madzivire, G., Petrik, L.F.: A review of combined advanced oxidation technologies for the removal of organic pollutants from water. Water Air Soil Pollut. **225**(9), 2102 (2014)

11. Foster, J.E.: Plasma-based water purification: challenges and prospects for the future. Phys. Plasmas **24**(5), 055501 (2017)

12. Wang, T., Qu, G., Ren, J., Sun, Q., Liang, D., Hu, S.: Organic acids enhanced decoloration of azo dye in gas phase surface discharge plasma system. J. Hazard. Mater. **302**, 65–71 (2016)

13. Mijin, D., Radulovic, M., Zlatic, D., Jovancic, P.: Photocatalytic degradation of textile dye RO 16 in TiO_2 water suspension by simulated solar light. Chem. Ind. Chem. Eng. Q. **13**, 179–185 (2007)

14. Mijin, D., Zlatic, D., Uscumlic, G., Jovancic, P.: Solvent effects on photodegradation of CI reactive orange 16 by simulated solar light. Hem. Ind. **62**, 275–281 (2008)

15. Khan, M.A.N., Siddique, M., Wahid, F., Khan, R.: Removal of reactive blue 19 dye by sono, photo and sonophotocatalytic oxidation using visible light. Ultrason. Sonochem. **26**, 370–377 (2015)

16. Basturk, E., Karatas, M.: Advanced oxidation of Reactive Blue 181 solution: a comparison between Fenton and Sono-Fenton process. Ultrason. Sonochem. **21**, 1881–1885 (2014)

17. Becelic-Tomin, M., Dalmacija, M., Dalmacija, B., Rajic, L., Tomasevic, D.: Degradation of industrial azo dye in aqueous solution by heterogeneous Fenton process (fly ash/H_2O_2). Hem. Ind. **66**, 487–496 (2012)

18. Jiang, B., Zheng, J., Qiu, S., Wu, M., Zhang, Q., Yan, Z., Xue, Q.: Review on electrical discharge plasma technology for wastewater remediation. Chem. Eng. J. **236**, 348–368 (2014)

19. Lukes, P., Clupek, M., Babicky, V., Janda, V., Sunka, P.: Generation of ozone by pulsed corona discharge over water surface in hybrid gas—liquid electrical discharge reactor. J. Phys. D **38**, 409–416 (2005)

20. Sun, Y., Liu, Y., Li, R., Xue, G., Ognier, S.: Degradation of reactive blue 19 by needle-plate non-thermal plasma in different gas atmospheres: kinetics and responsible active species study assisted by CFD calculations. Chemosphere **155**, 243–249 (2016)

21. McKay, K., Salter, T.L., Bowfield, A., Walsh, J.L., Gilmore, I.S., Bradley, J.W.: Comparison of three plasma sources for ambient desorption/ionization mass spectrometry. J. Am. Soc. Mass Spectrom. **25**, 1528–1537 (2014)

22. Dünnbier, M., Schmidt-Bleker, A., Winter, J., Wolfram, M., Hippler, R., Weltmann, K.D., Reuter, S.: Ambient air particle transport into the effluent of a cold atmospheric-pressure argon plasma jet investigated by molecular beam mass spectrometry. J. Phys. D **46**(43), 435203 (2013)

23. Puač, N., Maletić, D., Lazović, S., Malović, G., Dordević, A., Petrović, Z.L.: Time resolved optical emission images of an atmospheric pressure plasma jet with transparent electrodes. Appl. Phys. Lett. **101**(2), 024103 (2012)

24. Gumuchian, D., Cavadias, S., Duten, X., Tatoulian, M., Da Costa, P., Ognier, S.: Organic pollutants oxidation by needle/plate plasma discharge: on the influence of the gas nature. Chem. Eng. Process **82**, 185–192 (2014)

25. Robert, E., Darny, T., Dozias, S., Iseni, S., Pouvesle, J.M.: New insights on the propagation of pulsed atmospheric plasma streams: from single jet to multi jet arrays. Phys. Plasmas **22**(12), 122007 (2015)

26. Ghezzar, M.R., Saïm, N., Belhachemi, S., Abdelmalek, F., Addou, A.: New prototype for the treatment of falling film liquid effluents by gliding arc discharge part I: application to the discoloration and degradation of anthraquinonic Acid Green 25. Chem. Eng. Process. **72**, 42–50 (2013)

27. Kim, H.S., Wright, K.C., Hwang, I.H., Lee, D.H., Rabinovich, A., Fridman, A.A., Cho, Y.I.: Effects of H2O2 and low pH produced by gliding arc discharge on the inactivation of Escherichia coli in water. Plasma Med. **1**(3–4), 295–307 (2011)

28. Hijosa-Valsero, M., Molina, R., Schikora, H., Müller, M., Bayona, J.M.: Removal of priority pollutants from water by means of dielectric barrier discharge atmospheric plasma. J. Hazard. Mater. **262**, 664–673 (2013)

29. Pavlovich, M.J., Chang, H.-W., Sakiyama, Y., Clark, D.S., Graves, D.B.: Ozone correlates with antibacterial effects from indirect air dielectric barrier discharge treatment of water. J. Phys. D **46**, 145202 (2013)

30. Lukes, P., Clupek, M., Babicky, V., Sunka, P.: Ultraviolet radiation from the pulsed corona discharge in water. Plasma Sources Sci. Technol. **17**, 024012 (2008)

31. Lukes, P., Aoki, N., Spetlikova, E., Hosseini, S.H.R., Sakugawa, T., Akiyama, H.: Effects of pulse frequency of input power on the physical and chemical properties of pulsed streamer discharge plasmas in water. J. Phys. D **46**, 125202 (2013)

32. Lukes, P., Dolezalova, E., Sisrova, I., Clupek, M.: Aqueous-phase chemistry and bactericidal effects from an air discharge plasma in contact with water: evidence for the formation of peroxynitrite through a pseudo-second-order post-discharge reaction of H2O2 and HNO2. Plasma Sources Sci. Technol. **23**(1), 015019 (2014)

33. Garcia-Segura, S., Brillas, E.: Applied photoelectrocatalysis on the degradation of organic pollutants in wastewaters. J. Photochem. Photobiol. C **31**, 1–35 (2017)

34. Spasiano, D., Marotta, R., Malato, S., Fernandez-Ibáñez, P., Di Somma, I.: Solar photocatalysis: materials, reactors, some commercial, and pre-industrialized applications. A comprehensive approach. Appl. Catal. B **170**, 90–123 (2015)

35. Whitehead, J.C.: Plasma—catalysis: the known knowns, the known unknowns and the unknown unknowns. J. Phys. D **49**, 243001 (2016)

36. Parvulescu, V.I., Magureanu, M., Lukes, P., Liu, J., Bruggeman, P.J., et al.: Pulsed discharge purification of water containing nondegradable hazardous substances. J. Phys. D **33**, 145202 (2011)

37. Wang, T.C., Lu, N., Li, J., Wu, Y.: Plasma-TiO_2 catalytic method for high-efficiency remediation of p-nitrophenol contaminated soil in pulsed discharge. Environ. Sci. Technol. **45**, 9301–9307 (2011)

38. Ghezzar, M.R., Abdelmalek, F., Belhadj, M., Benderdouche, N., Addou, A.: Gliding arc plasma assisted photocatalytic degradation of anthraquinonic acid green 25 in solution with TiO2. Appl. Catal. B **72**(3–4), 304–313 (2007)

39. Evgenidou, E., Fytianos, K., Poulios, I.: Photocatalytic oxidation of dimethoate in aqueous solutions. J. Photochem. Photobiol. A **175**, 29–38 (2005)

40. Chen, L., Zhang, X., Huang, L., Lei, L.: Application of in-plasma catalysis and post-plasma catalysis for methane partial oxidation to methanol over a Fe_2O_3-CuO/γ- Al_2O_3 catalyst. J. Nat. Gas Chem. **19**, 628–637 (2010)

41. Gallon, H.J., Tu, X., Twigg, M.V., Whitehead, J.C.: Plasma-assisted methane reduction of a NiO catalyst-low temperature activation of methane and formation of carbon nanofibres. Appl. Catal. B **106**, 616–620 (2011)

42. Tu, X., Gallon, H.J., Whitehead, J.C.: Plasma-assisted reduction of a NiO/Al2O3 catalyst in atmospheric pressure H_2/Ar dielectric barrier discharge. Catal. Today. **211**, 120–125 (2013)

43. Du, Y.L., Deng, Y., Zhang, M.S.: Variable-temperature Raman scattering study on anatase titanium dioxide nanocrystals. J. Phys. Chem. Solids. **67**, 2405–2408 (2006)

44. Zaplotnik R, Kregar Z, Bišćan M, Vesel A, Cvelbar U, Mozetič M, Milošević S (2014) Multiple vs. single harmonics AC-driven atmospheric plasma jet. EPL 106(2):25001.

45. Parvulescu, V., Magureanu, M., Lukes, P.: Plasma chemistry and catalysis in gases and liquids. Wiley, New Jersey (2012)

46. Chen, Q., Li, J., Li, Y.: A review of plasma—liquid interactions for nanomaterial synthesis. J. Phys. D 48, 424005 (2015)

47. Malik, P.: Kinetics of decolourisation of azo dyes in wastewater by UV/H_2O_2 process. Sep. Purif. Technol. 36, 167–175 (2004)

48. Malik, M.A., Ghaffar, A., Malik, S.A.: Water purification by electrical discharges. Plasma Sources Sci. Technol. 10, 82–91 (2001)

49. Liu, D.X., Liu, Z.C., Chen, C., Yang, A.J., Li, D., Rong, M.Z., Chen, H.L., Kong, M.G.: Aqueous reactive species induced by a surface air discharge: heterogeneous mass transfer and liquid chemistry pathways. Sci. Rep. 6, 23737 (2016)

50. Ay, F., Kargi, F.: Advanced oxidation of amoxicillin by Fenton's reagent treatment. J. Hazard. Mater. 179, 622–627 (2010)

51. Bruggeman, P., Leys, C.: Non-thermal plasmas in and in contact with liquids. J. Phys. D 42(5), 053001 (2009)

52. Puač, N., Miletić, M., Mojović, M., Popović-Bijelić, A., Vuković, D., Miličić, B., Maletić, D., Lazović, S., Malović, G., Petrović, Z.L.: Sterilization of bacteria suspensions and identification of radicals deposited during plasma treatment. Open Chem. 13, 332–338 (2015)

53. Garcia-Segura, S., Mostafa, E., Baltruschat, H.: Could NOx be released during mineralization of pollutants containing nitrogen by hydroxyl radical? Ascertaining the release of N-volatile species. Appl. Catal. B 207, 376–384 (2017)

54. Miyazaki, Y., Satoh, K., Itoh, H.: Pulsed discharge purification of water containing nondegradable hazardous substances. Electr. Eng. Japan. 174, 1–8 (2011)

55. Williamson, G.K., Hall, W.H.: X-ray line broadening from filed aluminium and wolfram. Acta Metall. 1, 22 (1953)

56. Brunauer, S., Emmett, P.H., Teller, E.: Adsorption of gases in multimolecular layers. J. Am. Chem. Soc. 60(2), 309–319 (1938)

57. Rouquerol, J., Avnir, D., Fairbridge, C.W., Everett, D.H., Haynes, J.H., Pernicone, N., Ramsay, J.D., Sing, K.S.W., Unger, K.K.: Recommendations for the characteruzation of porous solids. Pure Appl. Chem. 66, 1739–1758 (1994)

58. Ribeiro, A.R., Nunes, O.C., Pereira, M.F.R., Silva, A.M.T.: An overview on the advanced oxidation processes applied for the treatment of water pollutants defined in the recently launched Directive 2013/39/EU. Environ. Int. 75, 33–51 (2015)

59. Daneshvar N, Rasoulifard MH, Khataee AR, Hosseinzadeh F (2007) Removal of C.I. acid orange 7 from aqueous solution by UV irradiation in the presence of ZnO nanopowder. J. Hazard. Mater. 143(1–2), 95–101.

60. Turchi, C.S., Ollis, D.F.: Photocatalytic degradation of organic water contaminants: mechanisms involving hydroxyl radical attack. J. Catal. 122, 178–192 (1990)

61. Yu, J., Wang, W., Cheng, B., Su, B.L.: Enhancement of photocatalytic activity of mesoporous TiO_2 powders by hydrothermal surface fluorination treatment. J. Phys. Chem. C. 113, 6743–6750 (2009)

62. Su, T.M., Liu, Z.L., Liang, Y., Qin, Z.Z., Liu, J., Huang, Y.Q.: Preparation of PbYO composite photocatalysts for degradation of methyl orange under visible-light irradiation. Catal. Commun. 18, 93–97 (2012)

Affiliations

Tatjana Mitrović[1] · Nataša Tomić[2] · Aleksandra Djukić-Vuković[3] · Zorana Dohčević-Mitrović[4] · Saša Lazović[2]

✉ Saša Lazović
lazovic@ipb.ac.rs

1 "Jaroslav Černi" Water Institute, Jaroslava Černog 80, 11226 Belgrade, Serbia

2 Institute of Physics Belgrade, University of Belgrade, Pregrevica 118, 11080 Belgrade, Serbia

3 Faculty of Technology and Metallurgy, University of Belgrade, Karnegijeva 4, 11000 Belgrade, Serbia

4 Nanostructured Matter Laboratory, Institute of Physics Belgrade, University of Belgrade, Pregrevica 118, 11080 Belgrade, Serbia

Size–strain line-broadening analysis of anatase/brookite (TiO$_2$)-based nanocomposites with carbon (C): XRPD and Raman spectroscopic analysis

Aleksandar Kremenović, Mirjana Grujić-Brojčin, Nataša Tomić, Vladimir Lazović, Danica Bajuk-Bogdanović, Jugoslav Krstić and Maja Šćepanović

research papers

Size–strain line-broadening analysis of anatase/brookite (TiO2)-based nanocomposites with carbon (C): XRPD and Raman spectroscopic analysis

Aleksandar Kremenović,[a]* Mirjana Grujić-Brojčin,[b] Nataša Tomić,[b] Vladimir Lazović,[c] Danica Bajuk-Bogdanović,[d] Jugoslav Krstić[e] and Maja Šćepanović[b]

[a]Faculty of Mining and Geology, University of Belgrade, Đušina 7, Belgrade 11000, Serbia, [b]Center for Solid State Physics and New Materials, Institute of Physics, University of Belgrade, Pregrevica 118, Belgrade 11000, Serbia, [c]Photonics Center, Institute of Physics, University of Belgrade, Pregrevica 118, Belgrade 11000, Serbia, [d]Faculty of Physical Chemistry, University of Belgrade, Studentski Trg 12-16, Belgrade 11000, Serbia, and [e]Department of Catalysis and Chemical Engineering, Institute of Chemistry, Technology and Metallurgy, University of Belgrade, Njegoševa 12, Belgrade 11000, Serbia. *Correspondence e-mail: akremenovic@rgf.bg.ac.rs

A size–strain line-broadening analysis of the XRPD patterns and Raman spectra for two anatase/brookite (TiO2)-based nanocomposites with carbon (C) was carried out and the results compared with those of a similar sample free of carbon. The crystal structures and microstructures of anatase and brookite, as well as their relative abundance ratio, have been refined from XRPD data by the Rietveld method (the low amount of carbon is neglected). The XRPD size–strain analysis resulted in reliable structure and microstructure results for both anatase and brookite. The experimental Raman spectra of all the samples in the region 100–200 cm^{-1} are dominated by a strong feature primarily composed of the most intense modes of anatase (E_g) and brookite (A_{1g}). The anatase crystallite sizes of 14–17 nm, estimated by XRPD, suggest the application of the phonon confinement model (PCM) for the analysis of the anatase E_g mode, whereas the relatively large brookite crystallite size (27–29 nm) does not imply the use of the PCM for the brookite A_{1g} mode. Superposition of the anatase E_g mode profile, calculated by the PCM, and the Lorentzian shape of the brookite A_{1g} mode provide an appropriate simulation of the change in the dominant Raman feature in the spectra of TiO2-based nanocomposites with carbon. Raman spectra measured in the high-frequency range (1000–2000 cm^{-1}) provide information on carbon in the investigated nanocomposite materials. The results from field-emission scanning electron microscope (SEM), thermogravimetric analysis (TGA), Fourier transform infrared (FTIR) spectroscopy and nitrogen physisorption measurements support the XRPD and Raman results.

1. Introduction

Titanium dioxide (TiO2) is the most commonly used photocatalyst because of its high efficiency, nontoxicity, chemical and biological stability, and low cost. Among the three natural crystalline modifications (anatase, rutile and brookite) of TiO2, anatase and rutile are the most common and have been extensively investigated due to their excellent photoactivity. However, little has been reported for the brookite modification. Investigation of the properties and applications was limited due to the difficulty in producing pure brookite (Di Paola *et al.*, 2008, 2013; Xie *et al.*, 2009; Iliev *et al.*, 2013; Lee *et al.*, 2006; Bhave & Lee, 2007; Lee & Yang, 2006). It was also reported that hydrothermal synthesis is necessary to obtain brookite as a major phase (Bhave & Lee, 2007). The control of pH is very important, as high basicity is required for the
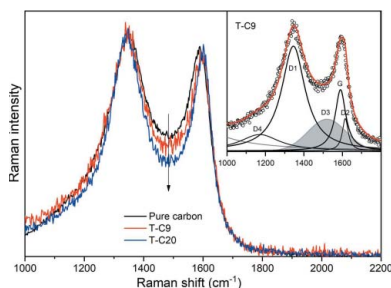
formation of brookite (Yanqing *et al.*, 2000; Zheng *et al.*, 2000; Okano *et al.*, 2009). Also, the control of the synthesis parameters, such as the hydrothermal temperature and reaction time, is of great importance (Nguyen-Phan *et al.*, 2011; Lin *et al.*, 2012; Tomić *et al.*, 2015).

Modifications of metal oxide nanoparticles with carbonaceous materials have attracted much attention over the past decade. Carbon materials, such as graphene, carbon nanotubes and carbon black, having unique structures, morphology, good conductivity and large surface area appear to be good candidates to be involved in the synthesis procedure with nanomaterials (Zhang, Lv *et al.*, 2010; Zhong *et al.*, 2010; Xie *et al.*, 2010; Cong *et al.*, 2015). This kind of composite is showing improvement in different application areas, such as water splitting for hydrogen generation and the degradation of various pollutants in wastewater, as well as air purification (Fan *et al.*, 2011; Sun *et al.*, 2014; Zhang, Tang *et al.*, 2010; Xie *et al.*, 2010). In this regard, it is beneficial to design composites that can provide higher adsorptivity, extended light absorption and good charge separation and transportation (Zhang, Lv *et al.*, 2010). Among the mentioned materials, carbon is easily affordable due to its low cost (Cong *et al.*, 2015).

This article is devoted to an investigation of the features and distinctions of XRPD and Raman scattering in the microstructure characterization of nanomaterials. XRPD and Raman spectroscopy results have been analysed and compared for pure TiO_2 and TiO_2 nanocomposites with carbon. The results of scanning electron microscopy (SEM), thermogravimetric analysis (TGA), Fourier transform infrared (FTIR) spectroscopy and nitrogen physisorption measurements support the XRPD and Raman results, and provide additional insight into the microstructure of the samples and their carbon content.

2. Materials synthesis

TiO_2 nanoparticles based on the brookite phase were synthesized using the sol–gel hydrothermal method. In a typical procedure, an appropriate amount of $TiCl_4$ (99.9% pure, Acros Organic) was dissolved in distilled water (150 ml) in an ice bath. In order to obtain the hydrogel, an aqueous solution of NaOH was added after careful control of the pH of the solution (pH $\sim$ 9). After aging in the mother liquor for 5 h, the hydrogel was placed in a steel pressure vessel (autoclave, $V = 50$ ml) at a controlled temperature. After treatment at 200°C for 24 h, filtration and washing (rinsing) with distilled water until complete removal of chloride ions were carried out. The last step was drying at 105.5°C for 72 h. For the purposes of preparing the composites of TiO_2 with carbon, a different amount of carbon black was added together with the hydrogel to an autoclave. As well as the pure TiO_2 sample (T-AB), samples with 9 and 20 wt% carbon black in the nanocomposite were prepared and are denoted T-C9 and T-C20, respectively. The carbon black content in these nanocomposites was estimated using thermogravimetric analysis (TGA) (see §1 of the supporting information).

3. Experimental methods

X-ray powder diffraction (XRPD) measurements were carried out on a Philips PW1710 diffractometer employing Cu $K\alpha_{1,2}$ radiation. Data were collected every 0.06° in the 10–110° 2θ angular range in step scan mode using a counting time of 12.5 s per step. The instrumental resolution function was obtained by parameterizing the profiles of the diffraction pattern of an LaB_6 (NIST SRM660a) standard specimen. Details of the XRPD line-broadening analysis are presented in §S2.1 of the supporting information.

Raman scattering measurements were performed using the TriVista TR557 triple spectrometer system equipped with a nitrogen-cooled CCD detector. The samples were excited in backscattering micro-Raman configuration by a Coherent Verdi G optically pumped semiconductor laser operating at 532 ± 2 nm with a minimal output laser power of about 20 mW. The Raman scattering measurements of nanopowders pressed into pellets were performed in the air, at room temperature, using an objective lens with 50× magnification and a 0.75 numerical aperture to focus the laser to a spot size of around 2 μm. To avoid local heating of the sample surface due to laser irradiation, neutral density filters transmitting 10 or 1% of the incident light were used to additionally reduce the laser power at the entrance of the optical system of the Raman spectrometer to less than 1 mW. To reveal the local heating effects on the Raman spectra of the investigated samples with a high carbon content, the output laser power was varied from 20 to 400 mW. In order to record the spectra with relatively high resolution in a lower frequency range, a 1800/1800/2400 grooves/mm diffraction grating combination was used in the TriVista system, whereas for the measurements in a wide wavenumber range with lower resolution, a 300/300/500 grooves/mm grating combination was used. In order to analyze the experimental results, the Raman spectra are fitted by the sum of the Lorentzian profiles and the profile obtained by Phonon Confinement Method (PCM) (see §S3.1 in the supporting information).

The morphologies of the synthesized nanopowders were studied on a Tescan MIRA3 field emission gun scanning electron microscope (FESEM) at 20 kV in a high vacuum. Powdered samples were sonicated in ethanol for 10 min, then a drop of the solution was applied to 'kish' graphite (crystals of natural graphite) and the sample was degassed in a low vacuum for an hour.

The loading percentage of C in TiO_2 was checked by TGA in air by scanning the temperature from 30 to 700°C at a rate of 10°C min^{-1} on an SDT 2960 TA instrument.

The IR transmission spectra of T-AB, T-C9 and T-C20 pellets before and after the introduction of carbon black were measured on a Thermo Nicolet 6700 FTIR spectrophotometer at room temperature in the range from 4000 to 400 cm^{-1}.

The textural properties of the nanocomposites were analyzed by nitrogen physisorption at −196°C using a Sorptomatic 1990 Thermo Finnigan device. Prior to adsorption, the samples were outgassed for 1 h in a vacuum at room temperature and, additionally, at 110°C and the same residual

pressure for 16 h. The specific surface areas (S_{BET}) of the samples were calculated from the linear part of the adsorption isotherm by applying the Brunauer–Emmet–Teller (BET) equation (Brunauer *et al.*, 1938).

4. Results and discussion

Results concerning composite materials of similar composition, TiO_2:Fe, are reported in Kremenović *et al.* (2011, 2013). In relation to the TiO_2:C composite materials presented in this article, the amount of Fe in TiO_2:Fe was significantly lower than the amount of C in TiO_2:C. Heterogeneity (phase and spatial), disorder, morphology and crystal structure were investigated for TiO_2:Fe. Only phase heterogeneity and not spatial heterogeneity is shown in TiO_2:C. The presence of three polymorphic modifications of TiO_2 (rutile, anatase and brookite), as well as amorphous TiO_2, was confirmed in TiO_2:Fe. The presence of Fe in TiO_2:Fe composites was confirmed only by SQUID magnetic measurements, but was not located in TiO_2 (rutile, anatase, brookite or amorphous) by XRPD (WPPF and PDF fit), high-resolution transmission electron microscopy (HRTEM) or Raman spectroscopy. SQUID magnetic measurements defined only the type of Fe distribution in the composite material. In the composite materials TiO_2:C, the presence of only two polymorphic modifications of TiO_2 (brookite and anatase) was confirmed, as well as amorphous C, but not amorphous TiO_2. The effect of Fe on the heterogeneity and disorder of TiO_2:Fe composites has not been studied, but the effect of C on TiO_2:C composites has been investigated. The aim of the study of TiO_2:C composite materials presented in this article is focused primarily on comparing the results of diffraction line/vibration mode broadening analysis using XRPD and Raman spectroscopic techniques. Also, during the investigation of TiO_2:Fe composite materials, the XRPD and Raman results were analyzed routinely. The XRPD and Raman results for TiO_2:C composite materials presented here have been analyzed and compared in much more detail. Such an analysis is necessary to determine the agreement/mutual support of the XRPD and Raman results. In this way, these two methods show a common/synergistic series of effects, which the individual methods alone cannot completely resolve.

4.1. XPRD

The XRPD patterns of the investigated samples are presented in Fig. S2 (see §S2.2 of the supporting information). In all three samples, the most intense diffraction peaks in the XRPD patterns can be ascribed to the two polymorph phases of TiO_2 brookite (PDF card 29-1360) and anatase (PDF card 78-2486). For the carbon-containing samples (T-C9 and T-C20), low-intensity diffraction peaks that correspond to carbon, *i.e.* the graphite 2H pattern (PDF card 89-7213), could be hardly distinguished due to extensive peak overlap with peaks from the brookite and anatase patterns. However, the 101 reflection at $\sim$44.5° 2θ that corresponds to the graphite 2H pattern could be recognized if the *y* axis is represented as a

Table 1
Refined unit-cell, structure and microstructural parameters (average apparent crystallite size and average maximal strain), quantitative phase analysis results, *i.e.* contents of anatase and brookite, as well as reliability factors of the refinements for T-AB, T-C9 and T-C20.

Sample	T-AB	T-C9	T-C20
Brookite (space group *Pbca*, No. 61)			
a (°)	9.1747 (2)	9.1850 (3)	9.1837 (2)
b (°)	5.4518 (1)	5.4579 (2)	5.4568 (1)
c (°)	5.1428 (1)	5.1488 (1)	5.1472 (1)
$\alpha=\beta=\gamma$ (°)	90	90	90
V (Å^3)	257.24 (1)	258.11 (1)	257.94 (1)
$\langle Ti-O\rangle$ (Å)	1.963 (5)	1.967 (6)	1.965 (5)
Average appar. size (nm)	29 (3)	27 (6)	29 (4)
Average max. strain $\times 10^{-4}$	11 (1)	7(2)	9(1)
%	74 (1)	83 (1)	77 (1)
R_B (%)	1.95	2.71	2.27
Anatase (space group $I4_1/amd$, No. 141)			
a (°)	3.7898 (2)	3.7939 (3)	3.7930 (2)
c (°)	9.4954 (6)	9.508 (1)	9.5089 (7)
$\alpha=\beta=\gamma$ (°)	90	90	90
V (Å^3)	136.38 (1)	136.86 (2)	136.81 (1)
$\langle Ti-O\rangle$ (Å)	1.955 (2)	1.962 (4)	1.957 (3)
Average appar. size (nm)	17 (2)	14 (5)	15 (7)
Average max. strain $\times 10^{-4}$	27 (3)	17 (6)	11 (5)
%	26 (1)	17 (1)	23 (1)
R_B (%)	1.79	3.10	1.74
Reliability factors of the refinements			
R_{wp} (%)	6.51	8.41	6.96
R_p (%)	4.71	6.52	5.36
R_{exp} (%)	4.70	4.63	4.41
χ^2	1.97	3.38	2.55

logarithm of diffraction intensity (insets of Fig. S2 in §S2.2 of the supporting information). The XRPD patterns indicate the microcrystalline to amorphous character of carbon black (see Fig. S3 in §S2.3 of the supporting information). The above-mentioned 101 reflection that corresponds to the graphite 2H pattern indicates a slight change of the carbon black crystalline structure during synthesis.

Structure models for the Rietveld (1969) refinements are taken from Meagher & Lager (1979) for brookite and from Horn *et al.* (1972) for anatase. Some of the results from the Rietveld refinements are presented in Table 1 and Fig. 1. Refined values of the atomic coordinates and the corresponding interatomic distances and angles are in good agreement with the literature data. For all three samples, the refined values of the interatomic Ti—O distances for brookite and anatase are in excellent agreement with the values obtained by Meagher & Lager (1979) and Horn *et al.* (1972) (Table 1). The same is true for the refined unit-cell parameters when compared to the values obtained by Meagher & Lager (1979) for brookite and Horn *et al.* (1972) for anatase. This is clear evidence that C atoms did not enter in significant amounts into the brookite and anatase crystal structures.

The contents of the brookite phase in the samples T-AB, T-C9 and T-C20 are 74 (1), 83 (1) and 77 (1)%, respectively (values in parentheses represent estimated standard deviations). A somewhat higher brookite content in the TiO_2-based nanocomposite samples (T-C9 and T-C20) in comparison to pure TiO_2 (T-AB) indicates that the presence of carbon may

have an influence on the brookite/anatase phase ratio. The quantity of crystalline carbon could not be refined due to its low abundance (probably less than 2%) and large diffraction peak overlap.

The refined average apparent crystallite size and average maximal strain in brookite are similar for all samples, indicating that the average crystallite size radius is about 30 nm and the average maximal strain is about 1×10^{-3} (Table 1).
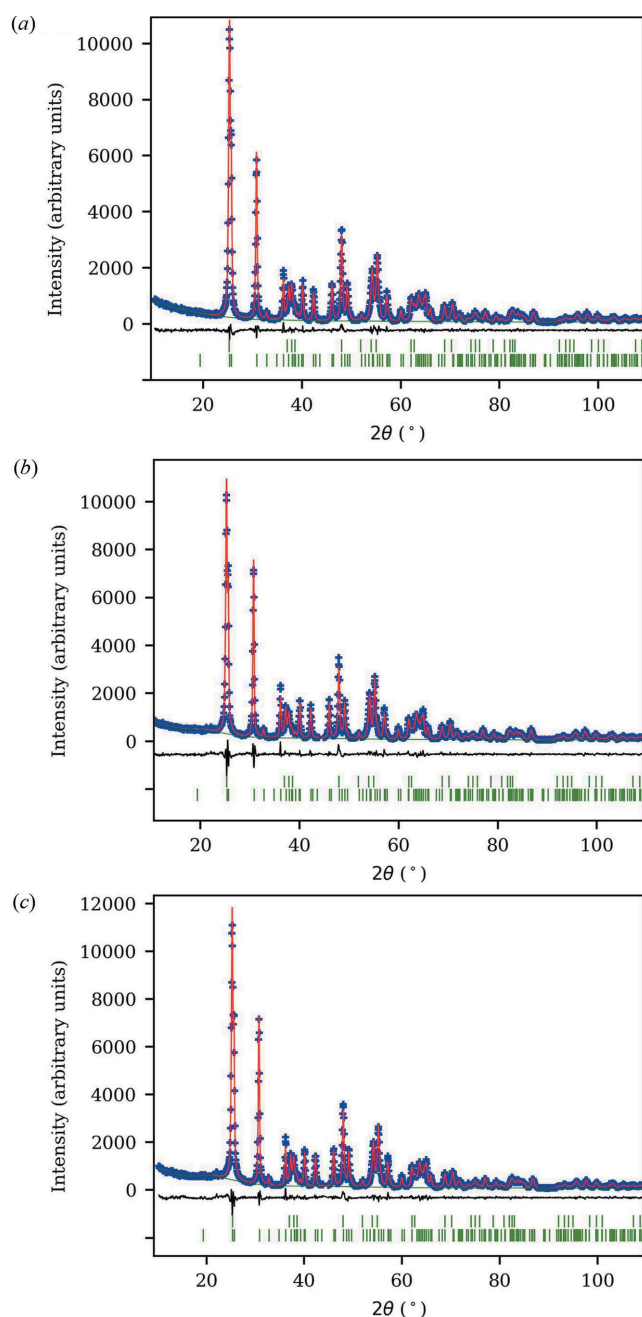

Figure 1
Final Rietveld plots for (a) T-AB, (b) T-C9 and (c) T-C20. Blue crosses denote observed step intensities and the red line represents the corresponding calculated values. The difference curve between the observed and calculated values is given at the bottom (black line). Vertical green bars represent diffraction line positions; the upper bars correspond to brookite and the lower bars to anatase.

The refined average apparent crystallite size and average maximal strain in anatase are similar for all samples, with the exception of the strain in T-AB (27×10^{-4}), indicating that the average crystallite size radius is about 15 nm and the average strain is about 15×10^{-4} (Table 1).

4.2. Raman scattering

The Raman spectra of all the synthesized samples are dominated by the features of anatase and brookite (shown and assigned in §S3.2 of the supporting information). The spectra taken in the region from 100 to 230 cm^{-1}, usually used as a reliable titania fingerprint (Tomić et al., 2015), are shown in Fig. 2. Characteristic Raman modes at ∼126 [A_{1g}(B)], 130 [B_{1g}(B)], 143 [E_g(A)], 153 [A_{1g}(B)], 160 [B_{1g}(B)], 172 [B_{1g}(B)], 197 [E_g(A) + A_{1g}(B)] and 212 cm^{-1} [A_{1g}(B)] are assigned to the anatase (A) and brookite (B) phases (Iliev et al., 2013; Ohsaka et al., 1978; Tomić et al., 2015; Šćepanović et al., 2007), as denoted in Fig. 2. Since the average crystallite sizes in anatase are estimated by XRPD to be from ∼14 to ∼17 nm (Table 1), it is expected that phonon confinement and other effects relevant for nanomaterials may have an impact on the most intense anatase E_g mode (Šćepanović et al., 2007;
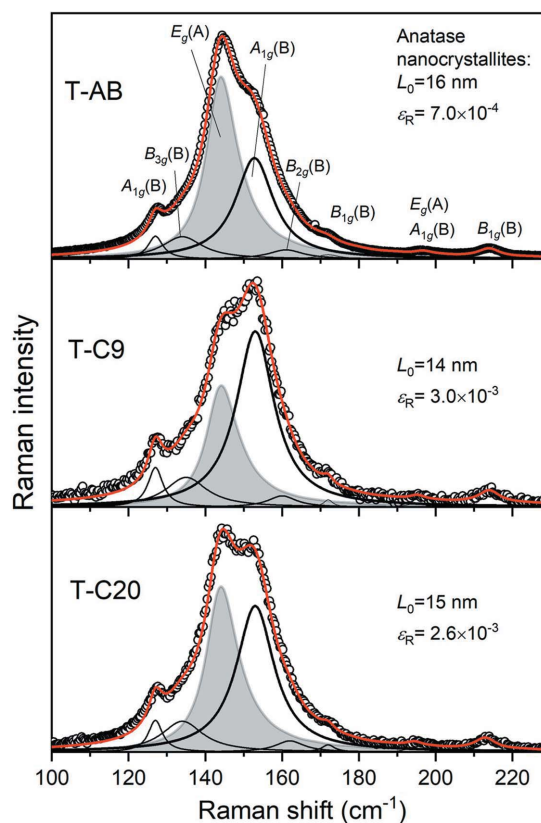

Figure 2
Experimental Raman spectra of T-AB, T-C9 and T-C20 in the titania fingerprint region (100–230 cm^{-1}), with the modes assigned, together with the corresponding calculated results, given as the sum of the most intense anatase mode, E_g(A), obtained by the PCM, other anatase (A) and all brookite (B) modes fitted by the Lorentzians. The values of the reduced chi-squared (χ^2) and adjusted R-squared (R^2) parameters: T-AB ($\chi^2 = 1.98 \times 10^{-5}$, $R^2 = 0.9964$), T-C9 ($\chi^2 = 4.55 \times 10^{-4}$, $R^2 = 0.9928$) and T-C20 ($\chi^2 = 1.24 \times 10^{-4}$, $R^2 = 0.9982$).

A. Kremenović et al. · Anatase/brookite (TiO2)-based nanocomposites with carbon

Kremenović *et al.*, 2013). On the other hand, for the crystallite size of brookite, estimated to be close to 29 nm (Table 1), the effect of phonon confinement (shift and broadening of the Raman mode) on the A_{1g} mode is not expected, as can be seen in previous work related to mixed-phase titania (Kremenović *et al.*, 2013; Tomić *et al.*, 2015). Therefore, all the modes shown in Fig. 2 are fitted by the Lorentzian profiles, except the most intense anatase E_g mode, which is simulated by the PCM (defined in §S3.1 of the supporting information).

The phonon confinement due to the nanosize effect causes asymmetrical broadening and a shift of the most intense anatase E_g mode to higher frequencies (blue-shift) in comparison to the corresponding bulk values. The influence of strain on the mode position is simulated in the PCM by Equations S11 and S12 (see §S3.1 in the supporting information), proposed by Gouadec & Colomban (2007) and Kibasomba *et al.* (2018). The values of the average correlation length L_0 and the so-called Raman strain (ε_R) in anatase, both obtained as fitting parameters in the numerical adjustment of the spectrum calculated by PCM to the experimental spectrum, are shown in Fig. 2. A good agreement between the

simulated and experimental E_g mode, with a similar Raman shift (~144 cm^{-1}) and broadening (~10–11 cm^{-1}) in all the investigated samples, could be obtained by using a parameter choice reflecting the compensation of the blue-shift due to a decrease of nanocrystallite size and the red-shift due to tensile Raman strain (see §S3.1 in the supporting information). Namely, the effects of tensile strain partially compensate for the effect of phonon confinement in such a way as to produce similar Raman positions in the spectra of all the samples in spite of their different correlation lengths.

The brookite modes are simulated by Lorentzian profile, with the position ~153 cm^{-1} and linewidth ~12 cm^{-1} of the most intense brookite A_{1g} mode similar for all the samples, which relies on the similar crystalline structure of brookite (Table 1). Therefore, the proposed fitting procedure is appropriate for an analysis of the changes in the position and shape of the dominant Raman features with C content in TiO$_2$-based nanocomposites.

The strong impact of different laser powers (1–400 mW) during the Raman measurements on the spectra of TiO$_2$-based nanocomposites with carbon has been noticed and analyzed for sample T-C20. The Raman feature shown in Fig. 3(*a*) is blue-shifted and becomes more symmetric with increasing laser power. The decomposition of the spectra with a procedure similar to that described above shows that the anatase E_g mode is blue-shifted (from 144.0 to 148.8 cm^{-1}) and broadened (from 10.5 to 18 cm^{-1}) with increasing laser power, whereas the brookite A_{1g} mode is less influenced; it is slightly red-shifted (by less than 1 cm^{-1}) and less broadened (by 12 to 16.5 cm^{-1}) in comparison to the anatase E_g mode [Fig. 3(*b*)]. This is in accordance with literature data (Šćepanović *et al.*, 2007, 2019; Du *et al.*, 2006) and indicates the increase of the local temperature at the sample surface up to 277°C at maximal laser power (400 mW) (Du *et al.*, 2006). This analysis also reveals that the Raman spectrum of the TiO$_2$ nanopowder
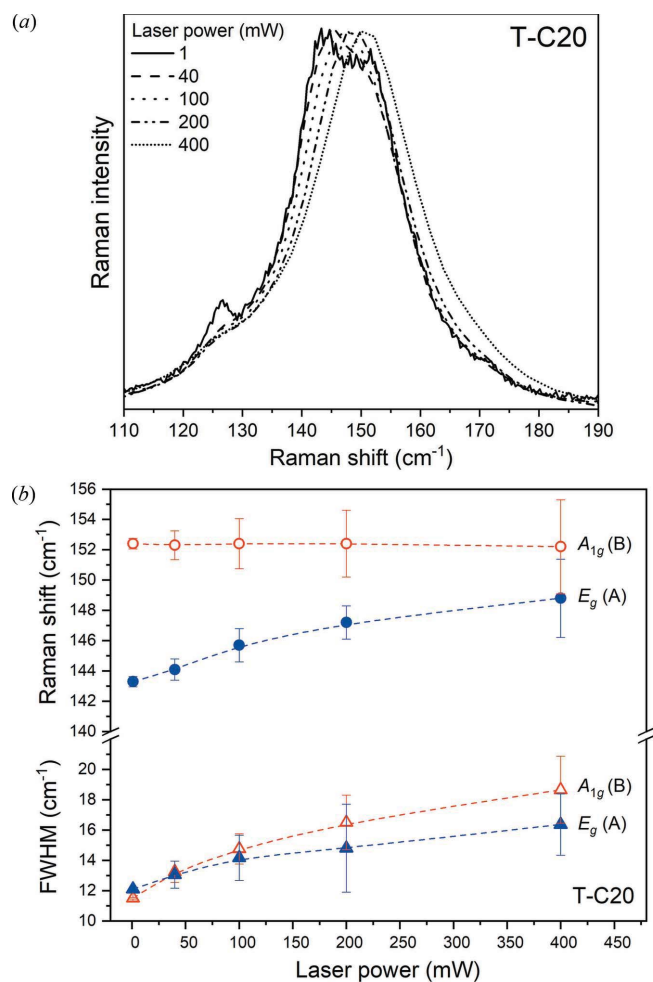

Figure 3
(*a*) Normalized Raman spectra of the TiO$_2$-based nanocomposite with 20% C (T-C20) taken at different laser powers in the range 1–400 mW. (*b*) The dependence of the Raman shift and the FWHM of the most intense anatase E_g (A) and brookite A_{1g} (B) modes on laser power.
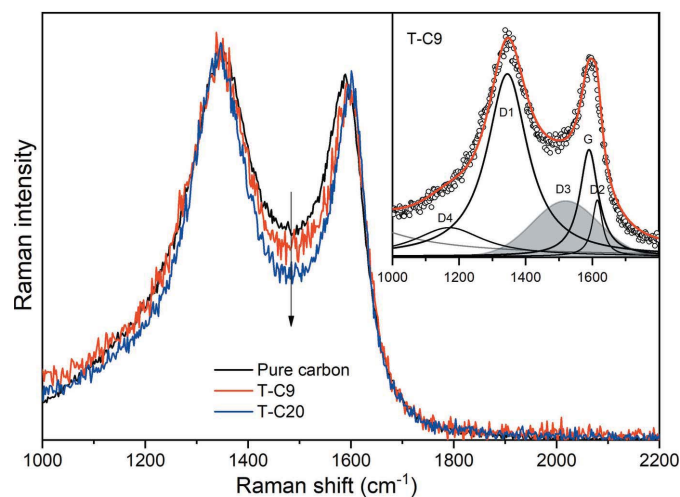

Figure 4
The Raman spectra of pure carbon and TiO$_2$-based nanocomposites T-C9 and T-C20, taken in the fingerprint carbon region and normalized to the G mode. Inset: the Raman spectra of nanocomposite sample T-C9, fitted by the sum of the corresponding Lorentzian and Gaussian profiles.

Table 2
The frequencies of the first-order Raman modes of carbon, together with relevant mode intensity ratios and the statistics of fit.

The intensities are denoted as: vs = very strong, s = strong, m = medium and w = weak. FWHM is full width at half maximum.

Band	Vibrational mode (Sadezky *et al.*, 2005)	Pure C Raman shift (cm^{-1})	Pure C FWHM (cm^{-1})	T-C9 Raman shift (cm^{-1})	T-C9 FWHM (cm^{-1})	T-C20 Raman shift (cm^{-1})	T-C20 FWHM (cm^{-1})
G	E_{2g} Graphitic structure (s)	1582	68	1590	67	1596	60
D1	A_{1g} Disordered graphitic lattice (vs)	1343	193	1345	148	1345	140
D2	E_{2g} Disordered graphitic lattice (s)	1610	39	1615	37	1615	37
D3	Amorphous carbon (Gaussian shape) (m)	1513	220	1520	200	1530	160
D4	A_{1g} Disordered graphitic lattice (w)	1177	318	1170	255	1170	300
Mode intensity ratio							
$I(D1)/I(G)$		2.3		3.6		3.9	
$I(D3)/I(G)$		1.8		1.2		0.8	
Goodness-of-fit							
Reduced χ^2		3.40×10^{-4}		8.82×10^{-4}		4.91×10^{-4}	
Adjusted R^2		0.9958		0.9906		0.9943	

composed of anatase and brookite phases, in the spectral range presented in Fig. 3(*a*), is mostly influenced by the behaviour of the anatase E_g mode.

Besides the TiO$_2$ modes discussed above, in the Raman spectra of the TiO$_2$-based nanocomposites (T-C9 and T-C20), features related to carbon are detected. In Fig. 4, the variations of the Raman spectra of pure carbon black and TiO$_2$-based nanocomposite samples are shown in the carbon fingerprint range (1000–2200 cm^{-1}). It can be seen that the central part of the normalized spectrum (around 1500 cm^{-1}) decreases from the pure carbon sample to T-C20. To relate the observed variations in the spectra to variations of the carbon structure due to hydrothermal synthesis conditions, the spectra have been fitted by the sum of the Lorentzians (denoted D1, D2 and G) and Gaussian (D3), according to the methodology optimized by Sadezky *et al.* (2005) and Pawlyta *et al.* (2015). The decomposed spectrum of T-C9 is given in the inset as an example, and the results are summarized in Table 2.

The D1 band, ascribed to the disordered graphitic lattice (Sadezky *et al.*, 2005), is located at a similar position in pure carbon and the TiO$_2$ nanocomposites. However, the G band, related to the graphitic structure (Sadezky *et al.*, 2005), is shifted in T-C9 and T-C20 towards higher frequencies in comparison to pure carbon. Such a shift, together with the narrowing of the D1 and G bands (see Table 2), indicates a decrease of the amorphous carbon content in the nano-composite samples (Ferrari *et al.*, 2000; Pawlyta *et al.*, 2015). Also, the narrowing and shift to higher frequencies of the D3 band, related to amorphous carbon (Merlen *et al.*, 2017; Sadezky *et al.*, 2005; Pawlyta *et al.*, 2015), supports the conclusion that the content of amorphous carbon decreases when carbon is subjected to a hydrothermal procedure, which is more pronounced in the nanocomposites with a higher carbon content.

Note that bands D3 and D4 (related to the disordered graphite lattice) may also originate from hydrogenation (CH)

and oxidation (CO), respectively (Karlin *et al.*, 1997; Merlen *et al.*, 2017), but in the nanocomposite samples investigated here, we have not detected CH and CO vibrations in the relevant regions of the FTIR spectra (see §S5 in the supporting information).

The ratios of the integrated intensities of the different Raman bands in the first-order spectral region have been used to perform further analysis of carbon crystalline and amorphous phases (Sadezky *et al.*, 2005; Pawlyta *et al.*, 2015). The increase of the integrated intensity ratio I_{D1}/I_G and the decrease of I_{D3}/I_G (Table 2) both point to a slightly higher content of the crystalline carbon phase and a lower amount of the amorphous carbon phase in the nanocomposites (especially in sample T-C20) than in pure carbon.

Although the refined unit-cell parameters obtained from XRPD analysis have shown that C atoms did not enter in significant amounts into the brookite and anatase crystal structures, the results of both characterization methods imply that carbon could influence the formation of brookite and anatase phases in TiO$_2$-based nanocomposites synthesized by the hydrothermal method. This is also supported by our wider research, where we have investigated the influence of carbon content in the range from 0.3 to 20% on the formation of titania phases by this synthesis method. The Raman results, presented in §S3.2 in the supporting information, show that the addition of a small amount of carbon suppresses the formation of brookite, so that the synthesized sample with a low carbon content is dominated by the anatase phase. An increase in the carbon content is followed by the formation of brookite in preference to the anatase phase. However, it seems that this transformation may be partially suppressed at a higher percent of carbon (as in sample T-C20), which may be a consequence of a different manner of formation of the composite with the highest carbon content (for an analysis of nitrogen physisorption, see §S7 of the supporting information). Recent research shows that the influence of carbon

A. Kremenović *et al.* • Anatase/brookite (TiO$_2$)-based nanocomposites with carbon **219**

content on the brookite-to-anatase ratio in TiO_2-based nanomaterials depends on the carbon source, the type of synthesis and the starting TiO_2 phase (Li *et al.*, 2013; Cano-Casanova *et al.*, 2021), but this subject still needs further study.

4.3. XRPD *versus* Raman scattering

Both XRPD and Raman scattering analyses have shown that TiO_2 consists of a combination of anatase and brookite phases in all samples investigated in this work. This is also supported by the SEM measurements (see §S6 in the supporting information), revealing two different types of particles: spherical, ascribed to anatase, and spindle-like, characteristic for brookite (Tomić *et al.*, 2015). The spindle-like particles of brookite in sample T-AB are elongated by up to ∼200 nm, with the shorter dimension estimated at less than 40 nm. By comparing size values for brookite obtained from XRPD (Table 1) and SEM measurements, one can conclude that on average one particle is composed from 6–7 crystallites.

It is known that the Raman modes in nanocrystalline oxide materials are very sensitive to disorder, caused by nonstoichiometry due to the nanometric crystallite size or thermal effects. In that sense, the correlation length is introduced in the PCM to define the mean size of the homogeneous regions in a material (Kosacki *et al.*, 2002). The correlation length may be influenced by many factors, such as the level of disorder due to the presence of point defects, dislocations and voids, as well as a disturbance in the long-range order, due to doping or the creation of solid solutions, so the PCM analysis of the Raman spectra may provide important information about lattice disorder (Šćepanović *et al.*, 2010). Having in mind that in this work the correlation lengths of the anatase phase used in the PCM simulations match the anatase crystallite size estimated by XRPD, the crystallites are suggested to have little disorder.

The analysis of the Raman spectra, performed in §4.2, has shown that the most intense brookite Raman A_{1g} mode is not significantly shifted and broadened in comparison to the bulk values (Iliev *et al.*, 2013). This fact, together with the brookite crystallite size (according to XRPD) being too big for phonon confinement effects, excludes the PCM analysis in the case of the brookite phase.

Regarding the amorphous TiO_2 phase, the Raman and XRPD analyses have given similar results. Namely, an analysis of the Raman spectra, decomposed by the combination of the PCM and Lorentzian profiles (§4.2), did not show the presence of modes which could be assigned to this phase (Kremenović *et al.*, 2013), either in pure TiO_2 or in the nanocomposites.

Besides giving insight into the nanocrystalline structures of the anatase and brookite phases in pure TiO_2 and nanocomposites, XRPD and Raman scattering may also provide information on their content ratio (see §S4 in the supporting information).

The carbon content, which contributes to the very dark colour of the sample (in comparison to the white of pure TiO_2), has little influence on the XRPD measurements, but in the Raman scattering causes a significant increase in the absorption of laser energy, which can induce local heating. This makes the nanocomposites with carbon extremely sensitive to laser power, which requires additional attention during the Raman measurements (careful choice of parameters and equipment). However, this allows an investigation of the behaviour of the Raman spectra of complex materials with local heating. The observed variation of the Raman spectra with increasing laser power (see Fig. 3) may even be used to estimate the level of heating and local temperature.

It appears that XRPD is not very useful for the investigation of carbon in the crystalline and especially amorphous state when it is present in small amounts. The intensities of the diffraction maxima depend on the number of electrons of the atoms that make up the crystal and XRPD barely detects carbon (carbon has only six electrons; we had to show the diffraction intensity on a logarithmic scale in order for the strongest carbon reflection to be visible) in samples T-C9 and T-C20. Note also that the results of XRPD analysis show that initial carbon is mostly amorphous (see §S2.3 of the supporting information). In contrast, the intensity of Raman scattering is proportional to the change in the polarizability of molecules; the atoms in carbon are tightly bound by strong covalent bonds and the Raman spectra show clearly defined carbon bands which do not overlap with the anatase and brookite modes. This allows a detailed analysis to be made of the variation of carbon structure due to hydrothermal synthesis by Raman scattering measurements (presented in Fig. 4 and Table 2). These results show that, during hydrothermal synthesis, the amorphous carbon phase is reduced in the nanocomposites in comparison to this phase in initial carbon. This is even more pronounced in sample T-C20, which may indicate that higher carbon content probably enhances the carbon crystallization during the hydrothermal process.

5. Conclusions

The compatibility, synergy and limits of XRPD and Raman scattering measurements have been established by investigating pure TiO_2 nanopowder and two TiO_2-based nanocomposites with different amounts of carbon, fabricated by the sol–gel hydrothermal method. To assure proper correlation between the XRPD and Raman results, several analytical techniques (TGA, SEM, FTIR and nitrogen physisorption) have also been used. Both XRPD and Raman scattering, together with SEM results, have shown that, in all the samples, brookite is a major phase with good crystallinity. Matching anatase crystallite sizes were determined by XRPD and PCM analysis of the anatase Raman E_g mode, confirming the low disorder of this phase. Amorphous TiO_2 has not been detected by either Raman scattering or XRPD. XRPD analysis could not detect whether significant amounts of carbon had been incorporated into the brookite and anatase crystal structures, whereas the Raman results revealed a decreasing content of amorphous carbon when subjected to the hydrothermal procedure, which is more pronounced in the nanocomposite with the higher carbon content. The brookite-to-anatase ratios estimated by the XRPD and Raman measurements imply that

carbon could influence the formation of the brookite phase in preference to the anatase phase in the TiO_2-based nanocomposites synthesized by the hydrothermal method.

6. Related literature

The following references are cited in the supporting information: Barrett *et al.* (1951); Campbell & Fauchet (1986); Dubinin (1975); Gregg & Sing (1982); Grujić-Brojčin *et al.* (2009); Hearne *et al.* (2004); Mikami *et al.* (2002); Richter *et al.*, 1981; Rodríguez-Carvajal (1993, 2001, 2016); Spanier *et al.* (2001); Stokes & Wilson (1944); Thompson *et al.* (1987); Wang *et al.* (2007).

References

Barrett, E. P., Joyner, L. G. & Halenda, P. P. (1951). *J. Am. Chem. Soc.* **73**, 373–380.

Bhave, R. C. & Lee, B. I. (2007). *Mater. Sci. Eng. A*, **467**, 146–149.

Brunauer, S., Emmett, P. H. & Teller, E. (1938). *J. Am. Chem. Soc.* **60**, 309–319.

Campbell, I. H. & Fauchet, P. M. (1986). *Solid State Commun.* **58**, 739–741.

Cano-Casanova, L., Amorós-Pérez, A., Ouzzine, M., Román-Martínez, M. C. & Lillo-Ródenas, M. A. (2021). *J. Environ. Chem. Eng.* **9**, 104941.

Cong, Y., Li, X., Dong, Z., Yuan, G., Cui, Z. & Zhang, J. (2015). *Mater. Lett.* **138**, 200–203.

Di Paola, A., Bellardita, M. & Palmisano, L. (2013). *Catalysts*, **3**, 36–73.

Di Paola, A., Cufalo, G., Addamo, M., Bellardita, M., Campostrini, R., Ischia, M., Ceccato, R. & Palmisano, L. (2008). *Colloids Surf. A Physicochem. Eng. Asp.* **317**, 366–376.

Du, Y. L., Deng, Y. & Zhang, M. S. (2006). *J. Phys. Chem. Solids*, **67**, 2405–2408.

Dubinin, M. M. (1975). *Prog. Surface Membrane Sci.* **9**, 1–70.

Fan, W., Lai, Q., Zhang, Q. & Wang, Y. (2011). *J. Phys. Chem. C*, **115**, 10694–10701.

Ferrari, A. C. & Robertson, J. (2000). *Phys. Rev. B*, **61**, 14095–14107.

Gouadec, G. & Colomban, Ph. (2007). *Prog. Cryst. Growth Charact. Mater.* **53**, 1–56.

Gregg, S. J. & Sing, S. J. (1982). *Adsorption, Surface Area and Porosity*. London: Academic Press.

Grujić-Brojčin, M., Šćepanović, M. J., Dohčević-Mitrović, Z. D. & Popović, Z. V. (2009). *Acta Phys. Pol.* **A116**, 51–54.

Hearne, G. R., Zhao, J., Dawe, A. M., Pischedda, V., Maaza, M., Nieuwoudt, M. K., Kibasomba, P., Nemraoui, O., Comins, J. D. & Witcomb, M. J. (2004). *Phys. Rev. B*, **70**, 134102.

Horn, M., Schwebdtfeger, C. F. & Meagher, E. P. (1972). *Z. Kristallogr. Cryst. Mater.* **136**, 273–281.

Iliev, M. N., Hadjiev, V. G. & Litvinchuk, A. P. (2013). *Vib. Spectrosc.* **64**, 148–152.

Karlin, S. & Colomban, Ph. (1997). *J. Raman Spectrosc.* **28**, 219–228.

Kibasomba, P. M., Dhlamini, S., Maaza, M., Liu, C.-P., Rashad, M. M., Rayan, D. A. & Mwakikunga, B. W. (2018). *Results Phys.* **9**, 628–635.

Kosacki, I., Suzuki, T., Anderson, H. U. & Colomban, Ph. (2002). *Solid State Ionics*, **149**, 99–105.

Kremenović, A., Antić, B., Blanuša, J., Čomor, M., Colomban, Ph., Mazerolles, L. & Bozin, E. S. (2011). *J. Phys. Chem. C*, **115**, 4395–4403.

Kremenovic, A., Grujic Brojcin, M., Welsch, A.-M. & Colomban, P. (2013). *J. Appl. Cryst.* **46**, 1874–1876.

Lee, B. I., Wang, X., Bhave, R. & Hu, M. (2006). *Mater. Lett.* **60**, 1179–1183.

Lee, J. H. & Yang, Y. S. (2006). *J. Mater. Sci.* **41**, 557–559.

Li, K., Xiong, J., Chen, T., Yan, L., Dai, Y., Song, D., Lv, Y. & Zeng, Z. (2013). *J. Hazard. Mater.* **250–251**, 19–28.

Lin, H., Li, L., Zhao, M., Huang, X., Chen, X., Li, G. & Yu, R. (2012). *J. Am. Chem. Soc.* **134**, 8328–8331.

Meagher, E. P. & Lager, G. A. (1979). *Can. Mineral.* **17**, 77–85.

Merlen, A., Buijnsters, J. G. & Pardanaud, C. (2017). *Coatings*, **7**, 153.

Mikami, M., Nakamura, S., Kitao, O. & Arakawa, H. (2002). *Phys. Rev. B*, **66**, 155213.

Nguyen-Phan, T.-D., Kim, E. J., Hahn, S. H., Kim, W.-J. & Shin, E. W. (2011). *J. Colloid Interface Sci.* **356**, 138–144.

Ohsaka, T., Izumi, F. & Fujiki, Y. (1978). *J. Raman Spectrosc.* **7**, 321–324.

Okano, S., Yamamuro, S. & Tanaka, T. (2009). *Sci. China Ser. E-Technol. Sci.* **52**, 190–192.

Pawlyta, M., Rouzaud, J.-N. & Duber, S. (2015). *Carbon*, **84**, 479–490.

Richter, H., Wang, Z. P. & Ley, L. (1981). *Solid State Commun.* **39**, 625–629.

Rietveld, H. M. (1969). *J. Appl. Cryst.* **2**, 65–71.

Rodríguez-Carvajal, J. (1993). *Physica B*, **192**, 55–69.

Rodríguez-Carvajal, J. (2001). *IUCr Commission on Powder Diffraction Newsletter*, **26**, 12–19.

Rodríguez-Carvajal, J. (2016). *FullProf* computer program (https://www.ill.eu/sites/fullprof/)

Sadezky, A., Muckenhuber, H., Grothe, H., Niessner, R. & Pöschl, U. (2005). *Carbon*, **43**, 1731–1742.

Šćepanović, M., Grujić-Brojčin, M., Lazarević, N. & Popović, Z. V. (2019). *Phys. Status Solidi A*, **216**, 1800763.

Šćepanović, M., Grujić-Brojčin, M., Vojisavljević, K., Bernik, S. & Srećković, T. (2010). *J. Raman Spectrosc.* **41**, 914–921.

Šćepanović, M. J., Grujić-Brojčin, M., Dohčević-Mitrović, Z. D. & Popović, Z. V. (2007). *Appl. Phys. A*, **86**, 365–371.

Spanier, J. E., Robinson, R. D., Zhang, F., Chan, S.-W. & Herman, I. P. (2001). *Phys. Rev. B*, **64**, 245407.

Stokes, A. R. & Wilson, A. J. C. (1944). *Proc. Phys. Soc.* **56**, 174–181.

Sun, H., Liu, S., Liu, S. & Wang, S. (2014). *Appl. Catal. Environ.* **146**, 162–168.

Thompson, P., Cox, D. E. & Hastings, J. B. (1987). *J. Appl. Cryst.* **20**, 79–83.

Tomić, N., Grujić-Brojčin, M., Finčur, N., Abramović, B., Simović, B., Krstić, J., Matović, B. & Šćepanović, M. (2015). *Mater. Chem. Phys.* **163**, 518–528.

Wang, D., Chen, B. & Zhao, J. (2007). *J. Appl. Phys.* **101**, 113501.

Xie, J., Lü, X., Liu, J. & Shu, H. (2009). *Pure Appl. Chem.* **81**, 2407–2415.

Xie, Y., Heo, S. H., Yoo, S. H., Ali, G. & Cho, S. O. (2010). *Nanoscale Res. Lett.* **5**, 603–607.

Yanqing, Z., Erwei, S., Suxian, C., Wenjun, L. & Xingfang, H. (2000). *J. Mater. Sci. Lett.* **19**, 1445–1448.

Zhang, H., Lv, X., Li, Y., Wang, Y. & Li, J. (2010). *ACS Nano*, **4**, 380–386.

Zhang, Y., Tang, Z.-R., Fu, X. & Xu, Y.-J. (2010). *ACS Nano*, **4**, 7303–7314.

Zheng, Y., Shi, E., Cui, S., Li, W. & Hu, X. (2000). *J. Am. Ceram. Soc.* **83**, 2634–2636.

Zhong, J., Chen, F. & Zhang, J. (2010). *J. Phys. Chem. C*, **114**, 933–939.

electronic reprint

The Serbian Society for Ceramic Materials

Institute for Multidisciplinary Research (IMSI), University of Belgrade

Institute of Physics, University of Belgrade

Center of Excellence for the Synthesis, Processing and Characterization of Materials for use in Extreme Conditions "CEXTREME LAB" - Institute of Nuclear Sciences "Vinča", University of Belgrade

Faculty of Mechanical Engineering, University of Belgrade

Center for Green Technologies, Institute for Multidisciplinary Research, University of Belgrade

Faculty of Technology and Metallurgy, University of Belgrade

Faculty of Technology, University of Novi Sad

PROGRAMME and the BOOK of ABSTRACTS

5CSCS-2019

5th Conference of the Serbian Society for Ceramic Materials June 11-13.2019. Belgrade Serbia

Edited by:
Branko Matović
Zorica Branković
Aleksandra Dapčević
Vladimir V. Srdić

Programme and Book of Abstracts of The Fifth Conference of The Serbian Society for Ceramic Materilas **publishes abstracts from the field of ceramics, which are presented at international Conference.**

area, mean pore diameter, pore volume and PSD), the presence of catalytically active mixed crystal phases and appropriate morphology provided efficient photocatalytic activity, especially when chemically modified catalyst was used.

1. M. Vasic, et al., *Process. Appl. Ceram.*, **10** [3] (2016) 189
2. G. Shao, et al., *Powder Technol.*, **258** (2014) 99

P-18

PHASE TRANSITION FROM TiO₂ BROOKITE-BASED NANOPOWDER TO TITANATE: EFFECT OF ANNEALING TEMPERATURE ON MORPHOLOGY AND PHOTOCATALYTIC BEHAVIOR

Nataša Tomić[1], Mirjana Grujić-Brojčin[1], Aleksandar Kremenović[2], Vladimir Lazović[3], Maja Šćepanović[1]

Center for Solid State Physics and New Materials, Institute of Physics, University of Belgrade, 11080 Belgrade, Serbia
Laboratory of Crystallography, Faculty of Mining and Geology, University of Belgrade, Đušina 7, 11001 Belgrade, Serbia
Photonics Center, Institute of Physics, University of Belgrade, 11080 Belgrade, Serbia

TiO₂ nanopowder based on brookite phase was synthesized using sol-gel hydrothermal method, with TiCl used as a precursor [1]. For the purposes of preparing one-dimensional (1D) nanoribbons, the obtained TiO₂ nanopowder was used as a precursor following an alkaline hydrothermal approach [2, 3], after which an annealing process took place. The structural properties of the synthesized nanomaterials were analyzed by X-ray powder diffraction (XRPD). Besides the XRPD pattern, the structural and morphological characteristics of obtained nanopowder and nanoribbon were also investigated by Raman spectroscopy and Field Emission Scanning Electron Microscopy (FESEM). Synthesized nanostructures were tested in photocatalytic degradation of Reactive Orange (RO16) azo-dye, since these dyes represent the most toxic ones among various types of dyes. The TiO₂ brookite-based nanopowder showed the best photocatalytic efficiency, whereas the titanate after annealing were much faster in degradation in comparison with titanate obtained after hydrothermal process.

[1] N. Tomić, *Mater. Chem. Phys.*, **163** (2015) 518
[2] V. Bellat, R. Chassagnon, O. Heintz, L. Saviot, D. Vandroux, N. Millot, *Dalton Trans.* **44** (2015) 1150
[3] A. Souza, O. Ferreira, V. Nunes, Aet al., *Mater. Res.*, **21** (2018) e20180110

SCMP

The 20th Symposium on Condensed Matter Physics

BOOK OF ABSTRACTS

Conference Chair

Cedomir Petrovic, *Brookhaven National Laboratory, USA*

Željko Šljivančanin, *Vinča Institute of Nuclear Sciences Serbia*

Organizing Committee

Jelena Pešić, *Institute of Physics Belgrade*
Andrijana Šolajić, *Institute of Physics Belgrade*
Petar Mali, *Faculty of Sciences, University of Novi Sad*
Jelena Pajović, *Faculty of Physics, University of Belgrade, Serbia*
Srđan Stavrić, *Vinča Institute of Nuclear Sciences*
Svetislav Mijatović, *Faculty of Physics, University of Belgrade, Serbia*
Božidar Nikolić, *Faculty of Physics, University of Belgrade, Serbia* – chair

Organized by

Institute of Physics Belgrade

Faculty of Physics, University of Belgrade
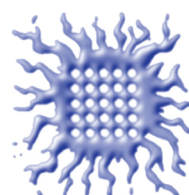
Vinča Institute of Nuclear Sciences

Serbian Academy of Sciences and Arts

Program Committee

Ivan Božović, *Brookhaven National Laboratory, USA*
Vladimir Dobrosavljević, *Florida State University, USA*
Milan Damnjanović, *Faculty of Physics, University of Belgrade, Serbia*
Vladimir Djoković, *Vinča Institute, University of Belgrade, Serbia*
Gyula Eres, *Oak Ridge National Laboratory, USA*
Laszló Forró, *Ecole Polytechnique Fédérale de Lausanne, Switzerland*
Radoš Gajić, *Institute of Physics Belgrade, University of Belgrade, Serbia*
Igor Herbut, *Simon Fraser University, Canada*
Zoran Ikonić, *University of Leeds, UK*
Ivanka Milošević, *Faculty of Physics, University of Belgrade, Serbia*
Branislav Nikolić, *University of Delaware, USA*
Cedomir Petrovic, *Brookhaven National Laboratory, USA*
Dragana Popović, *National High Magnetic Field Laboratory USA*
Zoran S. Popović, *Vinča Institute, University of Belgrade, Serbia*
Zoran V. Popović, *Institute of Physics, University of Belgrade, Serbia*
Zoran Radović, *Faculty of Physics, University of Belgrade, Serbia*
Miljko Satarić, *Faculty of Technical Sciences, University of Novi Sad, Serbia*
Vojislav Stamenković, *Argonne National Laboratory, USA*
Željko Šljivančanin, *Vinča Institute, University of Belgrade, Serbia*
Bosiljka Tadić, *Jožef Štefan Institute, Slovenia*
Milan Tadić, *School of Electrical Engineering, University of Belgrade, Serbia*
Darko Tanasković, *Institute of Physics, University of Belgrade, Serbia*

XX SYMPOSIUM ON CONDENSED MATTER PHYSICS SFKM 2019

Conference presentations cover full range of research topics within the experimental, theoretical and computational condensed matter physics, including but not limited to the following:

Semiconductor physics. Electronic structure, Quantum dots and wires, Photonic crystals, High magnetic fields phenomena, Ultra-fast phenomena.

Surface, interface and low-dimensional physics. Graphene, Carbon and other nanotubes, Topological insulators, Complex oxide interfaces, Transport in nanostructures.

Magnetism. Magnetic materials and phase transitions, Magneto-electronics and spintronics, Magnetic nanoparticles.

Superconductivity. Conventional, high Tc, and heavy-fermion superconductors: Materials and mechanisms, Heterostructures: Proximity effect and transport phenomena.

Strongly correlated and disordered systems. Materials with strong correlations and disorder, Dynamical properties from time-resolved experiments, Quantum fluids, Cold atoms and BEC.

Phase transitions, phase ordering and structural ordering of condensed matter. Equilibrium and dynamic phenomena, Ferroelectricity, Multiferroics, Quasi-Crystals, Crystal surface morphology and dynamics, Crystal growth.

Soft and biological matter. Polymers, Liquids and gels, Liquid crystals, Elastomers, Membranes, Living cells and living matter.

Statistical physics of complex systems. Networks and other structures.

Conference venue:
Serbian Academy of Sciences and Arts, Knez Mihailova 35, Belgrade

Conference website: http://www.sfkm.ac.rs

Pure Brookite Nanopowder: Photocatalytic Properties Before and After Annealing

Nataša Tomić[a], Mirjana Grujić-Brojčin[a], Bojana Višić[a], Jugoslav Krstić[b], and Maja Šćepanović[a]

[a]*Center for Solid State Physics and New Materials, Institute of Physics, University of Belgrade, 11080 Belgrade, Serbia*

[b]*Institute of Chemistry, Technology and Metallurgy, Department of Catalysis and Chemical Engineering, University of Belgrade, Njegoševa 12, 11000 Belgrade, Serbia*

Abstract. TiO_2 nanopowder with pure brookite phase was synthesized using sol-gel hydrothermal method, with $TiCl_4$ as a precursor [1]. After this alkaline hydrothermal approach an annealing process at 860 K took place. The structural properties of the as synthesized and annealed nanopowders were analyzed by X-ray powder diffraction (XRPD). The structural, morphological and texture characteristics of both nanopowders were also investigated by Raman spectroscopy, Scanning Electron Microscopy (SEM) and N_2 physisorption at 77 K. Efficiency of photocatalytic degradation of Reactive Orange (RO16), one of the most toxic azo-dye among various types of dyes, was investigated for both nanopowders. As synthesized brookite nanopowder showed the fast photocatalytic degradation of RO16, whereas the annealed nanopowder was slower in degradation under the same conditions. Lower degradation efficiency could be related to decrease of the textural parameters (specific surface area, mesopore volume, and maximum pore diameter) of brookite nanopowder due to annealing.

REFERENCES

1. Tomic, N., et al., *Mater. Chem. Phys.* **163**, 518-528 (2015).

Bulletin of the American Physical Society

Fall 2019 Meeting of the Ohio-Region Section and the Michigan Section of the American Association of Physics Teachers
Volume 64, Number 15
Friday–Saturday, October 11–12, 2019; Flint, Michigan

Session A02: OSAPS Poster Session
4:15 PM, Friday, October 11, 2019
Kettering University Academic Building Room: 3342

Chair: Corneliu Rablau, Kettering University

Abstract: A02.00006 : Formation of Palladium (II) Oxide within Titanium Dioxide Electrospun Nanofibers: Combined Raman and X-ray Diffraction Study

Preview Abstract   ← *Abstract* →

Authors:
　Daniel Isaacs
　　(University of Wisconsin Oshkosh)

　Patrick McManus
　　(University of Wisconsin Oshkosh)

　Nenad Stojilovic
　　(University of Wisconsin Oshkosh)

　Maja Scepanovic
　　(Institute of Physics, University of Belgrade)

　Mirjana Grujic-Brojcin
　　(Institute of Physics, University of Belgrade)

　Natasa Tomic
　　(Institute of Physics, University of Belgrade)

　Laila Shahreen
　　(The University of Akron)

　George Chase
　　(The University of Akron)

TiO_2-PdO composite submicron fibers were produced using electrospinning method. The morphology of the fibers was probed using Scanning Electron Microscopy, whereas Raman Spectroscopy and powder X-Ray Diffraction experiments were used for probing the crystalline phases of pure TiO_2 and TiO_2 -- PdO fibers. In particular, the effects of annealing time (at $600\ ^{o}C$) on the crystal structure and the role of embedded PdO were investigated. The results of Raman scattering measurements have shown dominant anatase TiO_2 phase in all samples. The crystallinity of anatase phase, as well as the appearence of rutile and brookite phases, depend on annealing and doping conditions. The existence of PdO within TiO_2 stabilizes its anatase phase, and the Raman modes ascribed to PdO become more pronounced with annealing. The combination of Raman and X-Ray diffraction techniques proves to be a powerful tool in characterizing these materials.

Formation of Palladium (II) Oxide within Titanium Dioxide Electrospun Nanofibers: Combined Raman and X-ray Diffraction Study DANIEL ISAACS, PATRICK MCMANUS, NENAD STOJILOVIC, University of Wisconsin Oshkosh, MAJA SCEPANOVIC, MIRJANA GRUJIC-BROJCIN, NATASA TOMIC, Institute of Physics, University of Belgrade, LAILA SHAHREEN, GEORGE CHASE, The University of Akron — TiO_2-PdO composite submicron fibers were produced using electrospinning method. The morphology of the fibers was probed using Scanning Electron Microscopy, whereas Raman Spectroscopy and powder X-Ray Diffraction experiments were used for probing the crystalline phases of pure TiO_2 and TiO_2 – PdO fibers. In particular, the effects of annealing time (at 600 ºC) on the crystal structure and the role of embedded PdO were investigated. The results of Raman scattering measurements have shown dominant anatase TiO_2 phase in all samples. The crystallinity of anatase phase, as well as the appearence of rutile and brookite phases, depend on annealing and doping conditions. The existence of PdO within TiO_2 stabilizes its anatase phase, and the Raman modes ascribed to PdO become more pronounced with annealing. The combination of Raman and X-Ray diffraction techniques proves to be a powerful tool in characterizing these materials.
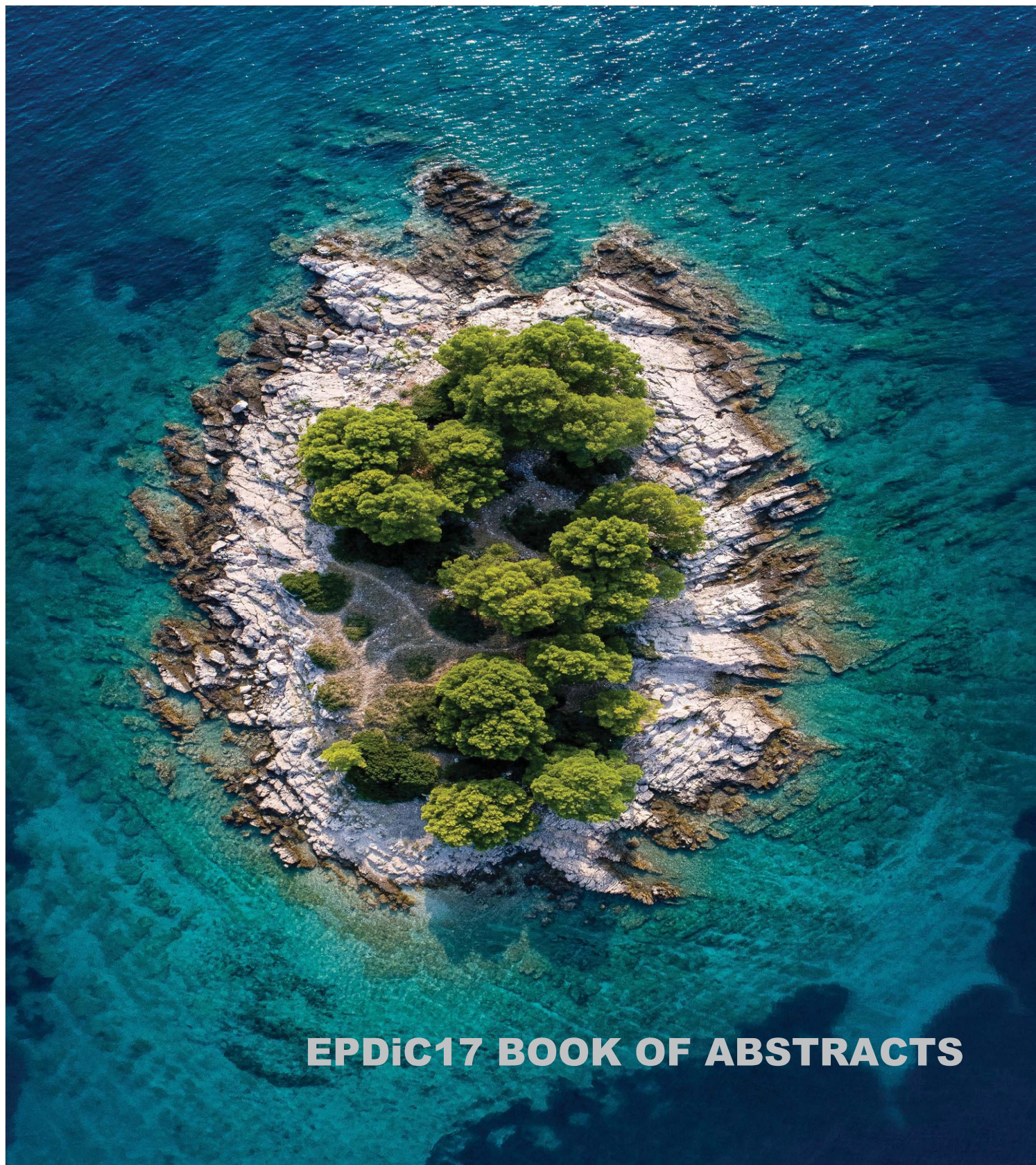
Nenad Stojilovic
University of Wisconsin Oshkosh

EPDiC17

Šibenik.Croatia. 31 May - 3 June 2022.

EPDiC17 BOOK OF ABSTRACTS

Structural and microstructural study of brookite based TiO$_2$ nanocomposites with carbon black (C)

Aleksandar Kremenović [1], Mirjana Grujić-Brojčin [2], Nataša Tomić [2], Maja Šćepanović [2]

[1] Faculty of Mining and Geology, University of Belgrade, Belgrade, Serbia

[2] Institute of Physics, University of Belgrade, Belgrade, Serbia

✉ aleksandar.kremenovic@rgf.bg.ac.rs

Structural and microstructural properties of TiO$_2$-based nanocomposites with carbon black (C), synthesized by sol-gel-hydrothermal method, have been studied by XRPD and Raman scattering. Detailed size-strain analyses of XRPD and Raman scattering results are presented in order to investigate the influence of C content on brokite and anatase phase formation. The XRPD size-strain analyses have resulted in reliable structure and microstructure results for both anatase and brookite and their relative abundance ratio has been refined by Rietveld method. The brookite and anatase crystallite sizes are estimated by XRPD at ~ 27–29 and 14–17 nm, respectively. The Raman spectra of all samples are dominated by the most intensive modes of anatase (E_g) and brookite (A_{1g}). The analysis of anatase E_g mode by PCM (Phonon Confinement model) has revealed partial compensation of phonon confinement due to anatase nanocrystallite size and tensile deformation of anatase lattice. The refined unit cell parameters obtained from XRPD have shown that C atoms did not enter in the significant amounts into brookite and anatase crystal structures. On the other side, the Raman spectra have revealed features assigned to carbon. The results of both analyses imply that the presence of carbon could influence the formation of brookite and anatase phase in the TiO$_2$-based nanocomposites synthesized by the hydrothermal method [1].

[1] A. Kremenović, M. Grujić-Brojčin, N. Tomić, V. Lazović, D. Bajuk-Bogdanović, J. Krstić, M. Šćepanović, Size-strain line broadening analysis of anatase/brookite (TiO$_2$) based nanocomposites with carbon (C) – XRPD and Raman spectroscopy, *Acta Crystallographica* **B**, in press.

ACADEMY OF SCIENCES AND ARTS OF THE REPUBLIC OF SRPSKA

ТЕХНИЧЕСКИ УНИВЕРСИТЕТ ГАБРОВО

ALMA MATER EUROPAEA
ECM
THE UNIVERSITY FOR LEADERSHIP

XV МЕЂУНАРОДНИ НАУЧНИ СКУП
САВРЕМЕНИ МАТЕРИЈАЛИ 2022

ПРОГРАМ РАДА
И
КЊИГА АПСТРАКАТА

XV INTERNATIONAL SCIENTIFIC CONFERENCE
CONTEMPORARY MATERIALS 2022

PROGRAMME
AND
THE BOOK OF ABSTRACTS

Бања Лука, 8 – 9. септембар 2022. године
Banja Luka, September 8th to 9th, 2022

ОРГАНИЗАТОР НАУЧНОГ СКУПА

Академија наука и умјетности Републике Српске

СУОРГАНИЗАТОРИ

Alma Mater Europaea
Технички универзитет Габрово

ПОКРОВИТЕЉ НАУЧНОГ СКУПА

Министарство за научнотехнолошки развој,
високо образовање и информационо друштво

ОДРЖАВАЊЕ СКУПА СУ ПОМОГЛИ

МХ Електропривреда Републике Српске
Универзитетски Клинички центар Републике Српске
Комора доктора медицине РС

ОРГАНИЗАЦИОНИ ОДБОР

Академик Драгољуб Мирјанић, предсједник
Академик Рајко Кузмановић
мр Срђан Рајчевић
Академик Бранко Шкундрић
Академик Неђо Ђурић
Академик Есад Јакуповић
Проф. др Илија Железаров
Проф. др Лудвик Топлак
Проф. др Зоран Рајилић
Проф. др Владо Ђајић
Проф. др Саша Вујновић

presented. This paper presents forensic medical expertise of traces on the corpse in combination with trasological analyzes, both on the corpse and on the materials related to the specific case of the crime of murder, which all contributed to clarifying the cause of the murder. The murder happened at night, commited by several people, the victim was a young man who was ostracized by his family due to frequent consumption of alcoholic beverages in combination with narcotics. In the cross-section of the set of conclusions that emerged after the conducted analyzes, an indisputable fact "emerged" that helped clarify this case.

Key words: Forensics, Medical analysis, Micro traces.

REMOVAL OF NADOLOL USING COUPLED NANOMATERIALS BASED ON TITANIUM AND CARBON

Andrijana Vukojević[1], Maria M. Savanović[1], Nataša Tomić[2], Stevan Armaković[1], Svetlana Pelemiš[3], Sanja J. Armaković[1]

[1]*University of Novi Sad, Faculty of Sciences, Novi Sad, Serbia,*
[2]*Center for Solid State and New Materials, Institute of Physics Belgrade, Belgrade, Serbia*
[3]*University of East Sarajevo, Faculty of Technology, Zvornik, Republic of Srpska, Bosnia and Herzegovina*

Abstract: Nadolol (NAD), one of the representatives of β-blockers, is used to treat cardiovascular diseases such as angina and hypertension. Due to its frequent use, it has been detected in hospital wastewater from which it is not removed efficiently enough, so it reaches natural waters. The lack of a satisfactorily efficient method for removing NAD from wastewater has created a need to find a more efficient way for its removal. This paper aims to investigate the efficiency of photocatalytic degradation of NAD by two TiO_2-C nanocomposites with different carbon content (9 and 20 wt%) under UV radiation. The applied nanocomposites, synthesized by the sol-gel hydrothermal method, showed significant efficiency in removing NAD compared to direct photolysis. Also, the reaction rate constant, according to which the decomposition of NAD in the presence of TiO_2-C takes place in the pseudo-first order, was calculated. The degradation of NAD was monitored by HPLC–PDA technique.

Key words: Nadolol, Photocatalytic degradation, Kinetics.

SCI WIDE
WEBINARS

5th Edition of Nanotechnology and Nanomaterials Virtual

December 09, 2022

V-NTNM2022

↓

Webinar Timings　　**Speakers Timings**

07:00 – 07:10　　　　　　　　　　　Introduction

Plenary Sessions

↓

07:10 – 07:50	12:40 – 13:20	Title: Designing of Functional Nano-Materials for Hydrogen Production using Overall Water Splitting Phenomenon **Tokeer Ahmad, Jamia Millia Islamia, India.**
07:50 – 08:30	16:50 – 17:30	Title: A Pure Titania Photocatalyst: Preparation, Characterization and Photocatalytic Activity of Octahedral-Shaped Anatase Particles **Bunsho Ohtani, Hokkaido University and Nonprofitable Organization touche NPO, Japan.**

Keynote Sessions

↓

08:30 – 09:05	16:30 – 17:05	Title: NANOGARD SC202 - Self Cleaning and Antifogging Coating for Automobile Industry **Vengadaesvaran Balakrishnan, UM Power Energy Dedicated Advanced Centre, Malaysia.**
09:05 – 09:40	17:05 – 17:40	Title: Gold Nanoparticle-based colorimetric Sensors for Pesticides Detection: A Review **Keat Khim Ong, National Defence University of Malaysia, Malaysia.**
09:40 – 10:15	10:40 – 11:15	Title: Hetero-structure-based Catalyst Nanomaterials for Visible Light-driven Photocatalytic CO_2 Reduction Reactions **Blaž Likozar, National Institute of Chemistry, Slovenia.**
10:15 – 10:50	18:15 – 18:50	Title: Nanocrystalline Tungsten Trioxide Cathode Films Prepared by Ultrasonic Spray Deposition for Electrochromic Applications **Chi-Ping Li, National United University, Taiwan.**

10:50 – 11:25	13:50 – 14:25	**Title:** Improving the Reliability Design of Mechanical Systems such as Refrigerator **Seongwoo Woo, Ethiopian Technical University, Ethiopia.**
11:25 – 12:00	15:25 – 16:00	**Title:** Domain wall Stability switching in magnetic nanowires for nanomemory storage devices **Mohammed Al Bahri, A'Sharqiyah University, Oman.**
12:00 – 12:35	07:00 – 07:35	**Title:** Contactless Magnetic Sensing in Condition Monitoring and Anomaly Detection for Smart Grid: New Possibilities and Alternatives **Philip Pong, New Jersey Institute of Technology, USA.**
12:35 – 13:10	07:35 – 08:10	**Title:** Experimental Evolution of Magnetite Nanoparticle Resistance in Escherichia coli **Akamu Jude Ewunkem, Winston Salem State University, USA.**

Invited Sessions

13:10 – 13:30	16:10 – 16:30	**Title:** Cyclable carbon dot/chitin nanocrystal hybrid for selective detection and adsorption of Cr(VI) and Co(II) from aqueous media **Elena F Krivoshapkina, ITMO University, Russian Federation.**
13:30 – 13:50	16:30 – 16:50	**Title:** Nanocomposite semiconducting materials for efficient utilization of visible light in photocatalytic reactions **Dmitry Selishchev, Boreskov Institute of Catalysis, Russian Federation.**
13:50 – 14:10	10:50 – 11:10	**Title:** Biopolymeric hybrid nanocomposites materials 3D printing with nanotechnological applications in the water treatment **Estefanía Baigorria, Sao Paulo State University, Brazil.**
14:10 – 14:30	16:10 – 16:30	**Title:** Supercapacitive Effects of Multi-Walled Carbon Nanotubes-Functionalized Spinel Copper Manganese Oxide **Christopher Nolly, University of the Western Cape, South Africa.**

14:30 – 14:40	15:30 – 15:40	Title: Application of single-crystal V2O5 in photodegradation of selected pharmaceutical products **Maria Savanovic, University of Novi Sad, Serbia.**
14:40 – 14:50	08:40 – 08:50	Title: In Vitro Ruminal Digestibility Test of Forage (Festuca arundinacea) biofortificated with Selenium Nanoparticles **Gabriela Medina-Pérez, Universidad Autonoma del Estado de Hidalgo, Mexico.**
14:50 – 14:60	22:50 – 23:00	Title: Metal selenides as electrodes for sustainable energy storage materials **Muhammad Sajjad, Zhejiang Normal University, China.**

Closing Ceremony

Application of single-crystal V_2O_5 in photodegradation of selected pharmaceutical products

<u>Maria M. Savanović</u>[1,3], Andrijana Bilić[1,3], Aleksandra Jovanoski Kostić[1], Stevan Armaković[2,3], Nataša Tomić[4], Maja Šćepanović[4], Mirjana Grujić-Brojčin[4], Aleksandar Kremenović[5], Sanja J. Armaković[1,3]

[1]University of Novi Sad, Faculty of Sciences, Department of Chemistry, Biochemistry and Environmental Protection, Novi Sad, Serbia
[2]University of Novi Sad, Faculty of Sciences, Department of Physics, Novi Sad, Serbia
[3]Association for the International Development of Academic and Scientific Collaboration (AIDASCO), Novi Sad, Serbia
[4]Center for Solid State and New Materials, Institute of Physics Belgrade, Belgrade, Serbia
[5]Faculty of Mining and Geology, University of Belgrade, Đušina 7, Belgrade, 11000, Serbia

Presenter Name: Maria Savanović
Email: maria.savanovic@dh.uns.ac.rs
Phone: +381642840046
Institute/ Organization: University of Novi Sad, Faculty of Sciences, Department of Chemistry, Biochemistry and Environmental Protection, Novi Sad, Serbia
Country: Serbia
Presentation Category: Poster Presentation

Among pharmaceuticals in natural and wastewater, a significant increase is noted for β-blockers due to the rise in cardiovascular diseases. Usually, β-blockers are present in the environment in a mixture or combined with various organic pollutants. To prevent and eliminate β-blockers from the environment, there is a need for new efficient methods and materials for their removal from the water environment. This work aimed to investigate the photocatalytic properties of hydrothermally synthesized V_2O_5 nanopowder towards photodegradation of three β-blockers (nadolol, pindolol, and metoprolol) separate and in the mixture in the presence of UV radiation. Structural, morphological, and surface properties of synthesized V_2O_5 nanopowder have been investigated by scanning electron microscopy, X-ray spectroscopy, and Raman spectroscopy. V_2O_5 was employed in the degradation of nadolol, pindolol, and metoprolol in separate water solutions, wherein it showed the greatest effect in removing pindolol. Further, the mixture of nadolol, pindolol, and metoprolol have been subjected to photocatalytic reaction with V_2O_5 to study their degradation when coexisting in environmental waters, as it occurs in nature. An increased degradation rate of nadolol and metoprolol was observed in the mixture, while the degradation efficiency of pindolol decreased. Density functional theory analysis was conducted to explain the influence of the molecular structure of selected β-blockers on the efficiency of the degradation process.